

Time, Tides, and Tectonics on Icy Satellites

by

Z. A. Selvans

B.S., California Institute of Technology, 1998

M.S., University of Colorado, 2007

A thesis submitted to the

Faculty of the Graduate School of the

University of Colorado in partial fulfillment

of the requirements for the degree of

Doctor of Philosophy

Department of Geological Sciences

2009

UMI Number: 3387542

All rights reserved

INFORMATION TO ALL USERS

The quality of this reproduction is dependent upon the quality of the copy submitted.

In the unlikely event that the author did not send a complete manuscript and there are missing pages, these will be noted. Also, if material had to be removed, a note will indicate the deletion.



UMI 3387542

Copyright 2010 by ProQuest LLC.

All rights reserved. This edition of the work is protected against unauthorized copying under Title 17, United States Code.



ProQuest LLC
789 East Eisenhower Parkway
P.O. Box 1346
Ann Arbor, MI 48106-1346

This thesis entitled:
Time, Tides, and Tectonics on Icy Satellites
written by Z. A. Selvans
has been approved for the Department of Geological Sciences

Karl Mueller

Robert T. Pappalardo

John Wahr

John Spencer

Bruce Jakosky

Date _____

The final copy of this thesis has been examined by the signatories, and we find
that both the content and the form meet acceptable presentation standards of
scholarly work in the above mentioned discipline.

Selvans, Z. A. (Ph.D., Geological Sciences)

Time, Tides, and Tectonics on Icy Satellites

Thesis directed by Prof. Karl Mueller

In the outer solar system, we cannot use the radiometric dating techniques applied in terrestrial geology. We also lack the detailed understanding of the correspondence between crater size-frequency distributions and absolute ages that lunar samples has given us in the inner solar system. Additionally, many geologically interesting icy satellites are insufficiently cratered to yield precise relative ages. Thus we must find other ways to construct geological chronologies. In this work I develop two techniques.

The first compares the linear tectonic features covering Jupiter's moon Europa to modeled tensile fractures resulting from tidal stresses due to the non-synchronous rotation (NSR) of the satellite's decoupled, icy, lithospheric shell. The amount of shell rotation required to align a feature with the stress field resulting from NSR is used as a proxy for time. This translation is potentially convolved with a phase lag between the tidal potential and the stresses it induces, resulting from the shell's partially viscous response to the NSR forcing. The geography of individual lineaments is found to be no more consistent with NSR stresses than chance would predict, however, the ensemble of global lineaments displays a non-uniform apparent rate of lineament formation throughout the time period recorded by the surface. This non-uniformity may be explained either by steady state fracture formation, activity, quiescence and erasure, or by a transient episode of tectonics.

The second technique encodes the myriad superposition relationships evident between Europa's tectonic features as a directed graph enabling algorithmic

analysis. The observed superposition relationships are generally insufficient to construct complete stratigraphic stacks, but we can calculate the degree to which they corroborate or contradict another hypothesized order of formation. We find that they tend to corroborate the hypothesis that the lineaments are tensile fractures due to prograde NSR stresses.

Together these results offer cautious support for the idea that Europa's shell rotates independently of its silicate interior, and demonstrate techniques useful in comparing tectonic features on other icy satellites to hypothesized mechanisms of formation.

Dedication

Para la chica rosa. Valía la pena.

Acknowledgements

Kim Stanley Robinson, for helping me dream big dreams again.

Bruce Murray, for getting me into grad school, and teaching me that you can (sometimes) safely get into a shouting match with your boss, and both be the better for it afterward.

Bob Pappalardo, for being sympathetic (maybe too sympathetic), and for inviting me into his harem.

Aaron S. Wolf for actually being willing and able to talk about science. Including the big chunk that's actually software engineering.

Irma Black for putting up with an uninvited visitor in her department, and both Dave Stevenson and Oded Aharonson for being willing to sponsor me as an uninvited visitor, and letting me audit their classes.

All the LASP and Geology admins who were somehow willing to send my paychecks into the electro-financial aether, despite sometimes having not seen me in months, or years, or maybe even ever.

All the open source software that made my work possible, including Python, Numpy, SciPy, Matplotlib, NetworkX, Graphviz, Quantum GIS, OSGEO, TeXShop, Subversion, and Vim.

Jorge Cham and his Ph.D. Comics, for making it clear I wasn't alone.

Contents

Chapter

1	Introduction	1
1.1	A (very) brief history of geologic time	1
1.2	Dating Extraterrestrial Surfaces	3
1.2.1	Counting Craters on Terrestrial Bodies	3
1.2.2	The Difficulties of Crater Dating Icy Satellites	4
1.3	The Approach of This Work	5
2	Modeling Tidal Stresses using Gravitational Potential Theory	6
2.1	Introduction	6
2.2	Stressing mechanisms	9
2.2.1	Nonsynchronous rotation	9
2.2.2	Diurnal tides	10
2.3	From tidal potential to viscoelastic stresses	11
2.3.1	The tidal potential	11
2.3.2	Relating the potential to elastic surface stresses	13
2.3.3	Introducing viscous relaxation	16
2.4	A qualitative description of NSR stresses	19
2.4.1	NSR tides in the fluid limit ($\Delta \gg 1$)	20
2.4.2	NSR tides in the elastic limit ($\Delta \ll 1$)	20

2.4.3	NSR tides in a truly viscoelastic case ($\Delta \approx 1$)	22
2.5	Numerical method, and a complication due to the core	25
2.6	Results	26
2.6.1	Love numbers	27
2.6.2	The direct effects of the outer layer's viscosity	30
2.6.3	Stress patterns and phase shifts	33
2.6.4	Geological implications of viscoelasticity	36
2.7	Comparison to previous methods	39
2.8	Summary and future work	44
3	A Critical Look at True Polar Wander and Non-Synchronous Rotation	46
3.1	Introduction	46
3.2	Methods	50
3.2.1	Mapping the Global Lineaments	50
3.2.2	NSR Stress Calculation	58
3.2.3	Comparing Lineaments to a Stress Field	60
3.2.4	Inferring a Time Series	64
3.2.5	Stress Isotropy and Noise	66
3.3	Results	69
3.3.1	Quality of fit is surprisingly uninformative.	69
3.3.2	Sinuosity, location and orientation determine lineament fits.	75
3.3.3	We need new metrics diagnostic of NSR.	78
3.3.4	The activity history of our map is very unlikely.	80
3.3.5	The current pole of rotation may not be special.	91
3.4	Conclusions	93
3.4.1	Three stories about NSR	93
3.4.2	Things that didn't happen on Europa.	100

3.4.3	Reconsidering our assumptions	101
4	Geological Superposition Networks	103
4.1	Introduction	103
4.2	From maps to graphs	105
4.2.1	Ideal GSNs	106
4.2.2	GSNs only yield partial orders	108
4.2.3	Using GSNs to corroborate an ordering hypothesis	111
4.2.4	Real world GSNs	116
4.3	Mapping E15	122
4.4	Results: Does the E15 GSN corroborate NSR?	128
4.5	Future GSN Applications	135
5	Conclusions and Future Work	137
Bibliography		140

Tables**Table**

2.1	Viscoelastic Model Parameters (Figs. 2.1, 2.3, and 2.4)	21
2.2	Diurnal Love Numbers for Europa	21
2.3	NSR Love Numbers for Europa	21
2.4	Flattening model parameters (Figs. 2.2 and 2.5)	43

Figures

Figure

2.1	Complex Love numbers and Lamé parameters as a function of Δ	24
2.2	Phase lag and NSR stress magnitudes as a function of Δ	31
2.3	Diurnal stresses as a function of orbital location	34
2.4	NSR stresses as a function of Δ	37
2.5	Stresses from the present work compared to the “flattening” method	40
3.1	Europa’s lineaments as mapped	51
3.2	Surface density of lineaments mapped on Europa	53
3.3	Correlation between mapped lineament density and mosaic resolution	54
3.4	Correlation between mapped lineament density and phase angle .	55
3.5	Correlation between mapped lineament density and incidence angle	56
3.6	Correlation between mapped lineament density and emission angle	57
3.7	Mapped lineaments transformed to suggested pre-TPW locations	59
3.8	NSR fit quality for several maps	67
3.9	Various lineaments and their associated fit curves.	70
3.10	Synthetic map of random great circle segments	72
3.11	Synthetic map of idealized NSR lineaments	73
3.12	Mapped lineaments with locations and orientations randomized .	76
3.13	Inferred activity history of our map, compared to random maps .	81

3.14	$H(b)$ for mapped features vs. a suite of resamplings	83
3.15	Activity histories ($H(b)$) of mapped lineaments classified by length	84
3.16	Activity histories ($H(b)$) of mapped features classified by sinuosity	85
3.17	The sensitivity of activity history ($H(b)$) to the value of \overline{D}_{max} . .	86
3.18	Distribution of $RMD(H(b))$ for various lineament populations. . . .	88
3.19	Mapped lineaments translated to their best-fit longitudes	90
3.20	Non-uniformity of activity history as a function of paleopole location	92
3.21	Synthetic $H(b)$ curves recreating our observations.	98
4.1	A synthetic random acyclic GSN	107
4.2	Dependence of C and $ R(X) $ with minimum intersection confidence	112
4.3	Southern E15 Regional Mapping Mosaic	123
4.4	Low Confidence Type Intersections	124
4.5	High Confidence Type Intersections	125
4.6	Mapped E15 lineaments	126
4.7	E15 Intersection Confidence Distribution	127
4.8	Distribution of path confidences in E15 GSN	129
4.9	Number and Confidence of Cycles in E15 GSN	131
4.10	NSR activity history inferred from the E15 map.	132
4.11	Significance of the E15 GSN's agreement with NSR ordering . . .	134

Chapter 1

Introduction

The temporal dimension is vital to nearly all scientific investigation, but poses special challenges to those who study naturally occurring processes that operate on geological or astronomical timescales. When the laboratory is a mountain range, ice sheet, or protoplanetary disk, and the experiment has been running since long before your species acquired the powers of speech, time risks becoming a thing to interpret as much as measure.

1.1 A (very) brief history of geologic time

In the late 17th century, Nicolas Steno created a general framework for the science of stratigraphy. It was made up of four axioms about the nature of sediment deposition and the temporal relationships between adjacent strata and other geologic features:

Original Horizontality:

Sediments are initially deposited as horizontal layers.

Superposition:

Newer strata are deposited upon older ones.

Lateral Continuity:

Strata have their lateral extent determined by pre-existing obstacles.

Cross-cutting Discontinuities:

Any feature which crosses a stratum must post-date its deposition.

Original horizontality is a simple but general statement about the energetics and systematics of sediment deposition. The other three principles all relate to superposition of one kind or another, to the ways in which a temporal relationship manifests itself in a physically durable way.

Steno also had another insight. He realized that fossils record the chronology of extant organisms, and that the set of extant organisms has changed through time. Thus an organism's appearance within or extinction from the fossil record becomes a kind of timestamp associated with the stratigraphic contact at which it occurs. Fossils alone cannot convey any temporal information, because evolution is not a cumulative or progressive process (e.g. shells do not become reliably longer or larger through evolutionary time), but in combination with their location in the stratigraphic column, they allow the correlation of geographically disconnected strata. This powerful combination of stratigraphic chronology and cross-correlation based on the fossil record was the main means of investigating geologic time for more than 200 years, but it resulted in a purely relative timeline. To pin this series of ordered geologic events to absolute time, a better understanding of basic physical processes was needed.

One of the first plausible attempts came in the late 19th century, William Thompson (Lord Kelvin) estimated the time required for the Earth to cool diffusively to its present temperature under the assumption that the planet was initially completely molten using the near-surface thermal gradient measured in deep mines. His estimate of $2 - 4 \times 10^7$ yr was off by two orders of magnitude because he was unaware of the heat generated within the Earth by radioactive decay. In 1905 Ernest Rutherford was the first to suggest (in a lecture attended

by Lord Kelvin no less) that natural radioactivity within the Earth had resulted in underestimates of the Earth's thermal age, and to propose the use of radioactive decay systems as a method of dating rocks. It was not until the 1930s that this method of dating was recognized as the best technique for obtaining absolute ages [*Knopf and Holmes*, 1931], and it took the improved understanding of nuclear processes that resulted from World War II and the development of sensitive mass spectrometry to really make radiometric dating the tool it is today [*Dalrymple*, 1994].

1.2 Dating Extraterrestrial Surfaces

In general the same stratigraphic and radiometric techniques used on the Earth are applicable to solid planetary bodies throughout the solar system. However, with the notable exception of the Earth's moon [*Hartmann*, 1970; *Husain et al.*, 1972; *Alexander et al.*, 1972], we have no in-situ absolute age measurements for any extraterrestrial surface, and we are generally limited to using imaging collected from orbital or greater distances in our large-scale geologic mapping. Within those constraints, the most successful method of dating planetary surfaces has been crater counting statistics.

1.2.1 Counting Craters on Terrestrial Bodies

Impact cratering is an ongoing, cumulative process, and so it may be used to establish at least the relative ages of adjacent surfaces. The size-frequency distribution of impact craters follows a power law, meaning that if one plots crater size versus the number of craters of that size per unit area in log-log space, the result is a straight line [*Hartmann*, 1966a, b]. Such lines are isochrons, indicating a particular age for any surface whose crater size-frequency distribution plots along it. Valid relative ages may be obtained for any two surfaces subjected to the

same impactor population and experiencing the same weathering processes. This dating technique was first developed in the 1960s for use on the Earth's moon, and soon thereafter applied to the early Mariner data from Mars.

Because the U.S. Apollo and Soviet Luna programs returned samples from known locations on the lunar surface to Earth for analysis, it has been possible to associate absolute radiometric ages with the isochrons derived from lunar crater counting statistics. Those results have been extrapolated, with significant corrections, to the other terrestrial planetary bodies. The isochron associated with a particular crater size-frequency distribution on the moon cannot be used directly on other bodies for a variety of reasons, including different impact energies for the same size impactors, depending on the target's location in the solar gravitational potential well and the target's own gravity, atmospheric screening of small impactors, and different weathering environments and resurfacing processes. Using crater counts to assign absolute ages to surfaces in the outer solar system is much more difficult.

1.2.2 The Difficulties of Crater Dating Icy Satellites

Crater counting systematics from the inner solar system do not directly generalize to the icy bodies of the outer solar system for several reasons. Foremost is the fact that the impactor population is different. In the inner solar system most impactors come from the main belt asteroids, but in the outer solar system dynamical simulations indicate that the Jupiter family comets ought to dominate, with some smaller contribution from long period comets and co-orbiting objects (e.g. Centaurs) that have been disturbed [Zahnle *et al.*, 1998; Zahnle, 2001; Zahnle *et al.*, 2003]. In addition to the different impactor population, the target material is ice and not silicates, which influences the mechanics of crater formation and some satellites may have deep liquid water oceans near enough to the surface to

affect the formation of large impact basins. Impact energies are also significantly altered by the gravity of the parent planets. Tidal disruption of poorly consolidated inbound objects is also likely, as was seen when Shoemaker-Levy 9 impacted Jupiter, and may not always result in obviously identifiable crater chains. Our understanding of important resurfacing processes is also much less well developed for icy satellites than for the terrestrial bodies of the inner solar system. In the case of Europa these difficulties are compounded by very low crater densities and the satellite's correspondingly young apparent surface age. It has further been suggested that what small craters there are may be overwhelmingly the result of secondary impacts [Bierhaus *et al.*, 2005].

1.3 The Approach of This Work

For all of the above reasons, if we are to understand the time evolution of the geology of icy satellites, it is desirable that alternative techniques be found of dating their surfaces. This thesis explores two potential methods. First, a model of the tidal stresses experienced by Europa as a result of both its eccentric orbit, and the non-synchronous rotation of the icy shell is developed. The rotation of the shell relative to Jupiter is then used as a proxy for time, by measuring how well tectonic features match the stresses as a function of their longitudinal translation. The second method revisits Steno's original stratigraphic axioms, and applies them to a map of the many cross-cutting linear features on Europa, resolving the implied temporal relationships algorithmically.

Chapter 2

Modeling Tidal Stresses using Gravitational Potential Theory

2.1 Introduction

A body subject to a varying gravitational potential will experience tidal deformation as different portions of the body are subjected to different gravitational forcings. The stresses arising from tidal deformations will be either stored elastically, relieved through material failure, or relaxed away viscously. Both failure and relaxation are dissipative processes capable of doing significant work; elastic storage of stress is reversible. In a viscoelastic body, the partitioning of stress among elastic storage, failure, and relaxation will depend on the strength and rheological properties of the body, and on the period of the forcing potential. If the forcing period is roughly equal to or greater than the natural viscous relaxation time of the material being forced, significant viscous relaxation may result, preventing or reducing the extent of material failure and reducing the amount of stress stored elastically.

In the case of natural satellites there are many possible sources of time-variable tidal deformation, for example tidal despinning [Melosh, 1977, 1980a], reorientation relative to the spin axis [Melosh, 1975, 1980b], orbital recession or procession [*Squyres and Croft, 1986; Helfenstein and Parmentier, 1983*], nonsynchronous rotation [*Helfenstein and Parmentier, 1985*], polar wander [*Leith and McKinnon, 1996*], and radial and librational tides due to an eccentric orbit [*Yo-*

der, 1979; Hoppa, 1998; Greenberg et al., 1998]. Many satellites exhibit large-scale systems of linear surface features that have been interpreted as faults, fractures, and other tectonic structures, and which have been linked to the above mechanisms. Examples include the three resonant Galilean satellites [McEwen et al., 2004; Greeley et al., 2004; Pappalardo et al., 2004], several of the middle-sized uranian and saturnian satellites [Squyres and Croft, 1986; Croft and Soderblom, 1991; Nimmo and Pappalardo, 2006; Nimmo et al., 2007], Triton [Croft et al., 1995], and even Mars' small irregular satellite Phobos [Dobrovolskis, 1982]. In these cases, observations of a satellite's global tectonic features, combined with a model of its tidal deformation, can be used to gain understanding of the satellite's dynamical and structural evolution.

In the case of icy satellites, viscous effects are likely to play an important role in the stress environment. This is because viscosity generally drops significantly as a material approaches its melting point, and the melting point of ice is much lower than that of silicates. Additionally, tidal heating appears to be an important factor in the histories of many icy bodies [Ojakangas and Stevenson, 1989; Meyer and Wisdom, 2007; Showman et al., 1997], meaning portions of the icy moons may have spent significant periods of time at relatively high temperatures.

In this work, we develop a model of tidal deformation and stress for an arbitrary satellite that is based on long-standing methods of computing global tides and stresses on the Earth. We treat the lithosphere as a layered Maxwell viscoelastic solid to understand how the relaxation of tidal stresses could affect the interpretation of global tectonic features. We focus on nonsynchronous rotation (NSR) and eccentricity (diurnal) tides, which offer the most plausible explanation for the pattern of lineaments observed on the surface of Europa [Helfenstein and Parmentier, 1985; McEwen, 1986; Leith and McKinnon, 1996; Geissler et al., 1998; Greenberg et al., 1998; Hoppa, 1998; Hoppa et al., 1999b, c; Figueiredo and

Greeley, 2000; Kattenhorn, 2002; Spaun et al., 2003]. We assume the satellite has radially dependent material properties, and include a rocky core, a hydrostatic ocean, and a lithospheric shell of arbitrary thickness having multiple viscosity layers. The frequency-dependent response is incorporated into the model through the use of complex-valued Lamé parameters and Love numbers. For demonstration purposes we apply the model to Jupiter’s satellite Europa. We assume Europa’s lithosphere consists of a high-viscosity outer layer surrounding a low viscosity inner layer, which approximates an ice shell undergoing stagnant lid convection. A parallel approach has been undertaken by [Harada and Kurita, 2007], who also consider a tidal potential method and viscoelastic relaxation of NSR stresses, but who do not provide the details of their calculations.

Our approach of deriving stresses directly from the gravitational potential has several advantages over previously published approaches, which derive stresses based on an instantaneous change in the triaxial ellipsoid describing a satellite’s shape [Melosh, 1977; Helfenstein and Parmentier, 1985; Leith and McKinnon, 1996; Hoppa, 1998]:

- (1) It allows the Love numbers h and ℓ to be specified independently, decoupling the radial and lateral tidal deformations.
- (2) It allows the use of realistic rheological properties for the body (e.g. treatment of the ice shell as a Maxwell solid; radially dependent structural properties, including the presence of a solid core; compressibility), and does not require that the outer shell be thin.
- (3) Because viscoelastic effects are included directly into the equations of motion, the results can be applied to all possible combinations of NSR rates and viscosity values.

- (4) Its mathematical form is amenable to the inclusion of individual potential terms (NSR or diurnal) and the future inclusion of other terms in the description of the potential (e.g., obliquity or polar wander).

This chapter is excerpted from work published in more detail as *Wahr et al.* [2009]. It describes the NSR and diurnal tidal forcing mechanisms (Section 2.2) and outlines a mathematical framework for computing the resulting outer surface stresses both for elastic and Maxwell viscoelastic satellites (Section 2.3). The effects of viscoelasticity on the NSR stresses are discussed qualitatively in Section 2.4. We use the viscoelastic model developed in Section 2.3 to compute diurnal and NSR stresses for Europa (Sections 2.5 and 2.6), and compare with results computed using previously published methods (Section 2.7).

2.2 Stressing mechanisms

2.2.1 Nonsynchronous rotation

The tidal despinning timescales for large natural satellites are short compared to the age of the solar system, meaning that today nearly all satellites are synchronously locked, always showing their parent planet the same hemisphere [Peale, 1999]. However, many large icy satellites are believed to have global oceans which decouple the motions of their floating shells from their interiors [Schubert et al., 2004]. Such a decoupled shell could experience a net tidal torque, and could rotate slightly faster than synchronously [Greenberg and Weidenschilling, 1984; Ojakangas and Stevenson, 1989]. From the rotating shell's point of view, the apparent location of the parent planet moves slowly across the sky. The tidal bulge, which remains fixed relative to the parent planet, appears to migrate in the direction opposing the rotation. As the bulge passes over a region of the shell, that region deforms and experiences a stress. If NSR exists, it should occur with a

period similar to the thermal diffusion or viscous relaxation timescales of the shell [Greenberg and Weidenschilling, 1984; Ojakangas and Stevenson, 1989], and thus viscous relaxation is likely to influence NSR stresses. Observations constrain the present period of NSR of Europa’s ice shell to be $> 10^4$ yr [Hoppa et al., 1999a]. NSR could also affect Ganymede [Collins et al., 1998; Zahnle et al., 2003; Nimmo and Pappalardo, 2004] and Io [Greenberg and Weidenschilling, 1984; Schenk et al., 2001], and could apply to other satellites with fluid or low-viscosity interiors.

2.2.2 Diurnal tides

Diurnal stresses for a synchronously rotating satellite have the same period as a satellite’s orbit. They arise on a satellite in an eccentric orbit for two reasons. First, for an eccentric orbit the distance between the satellite and the planet changes with time, thus changing the amplitude of the planet’s gravitational force on the satellite, creating the “radial tide.” At periape the tidal bulge is larger than at apoapse, and this daily deformation results in diurnally varying stresses.

Second, a synchronously orbiting satellite in an eccentric orbit does not always keep the same face toward the planet. A satellite at periape is orbiting slightly faster than its (constant) rotation rate, and at apoapse is orbiting slightly slower. This causes the tidal potential to rock back and forth relative to fixed points in the satellite, inducing a “librational tide” [Yoder, 1979; Greenberg et al., 1998].

As will be seen below, the magnitudes of these tides are proportional to the orbital eccentricity ϵ (for small values of ϵ). Diurnal tides have been suggested to explain the formation of the cycloidal ridges on Europa [Hoppa et al., 1999c], as well as tectonic structures on Io [Bart et al., 2004], Enceladus [Nimmo et al., 2007] and Triton [Prockter et al., 2005]. Diurnal forcing is at a much higher frequency than the NSR forcing, and so is less influenced by viscous relaxation.

2.3 From tidal potential to viscoelastic stresses

This section gives an overview of the derivation of the surface stresses on a Maxwell viscoelastic satellite subjected to the tidal forcings listed in the previous section. For a more detailed treatment, see *Wahr et al.* [2009], from which this content is excerpted.

2.3.1 The tidal potential

In the equilibrium state of a synchronously rotating satellite, the entire satellite is rotating together without deforming, and the satellite's rotation rate is equal to its mean motion, n , about the parent planet. On Europa for example, the rotation rate = $n = 2\pi/3.55$ radians/terrestrial day. We are assuming in this work that tidal dissipation has driven the orbital obliquity of the satellite to zero, meaning that the satellite's rotation axis is perpendicular to its orbital plane. Recent work [*Bills*, 2005] suggests that Europa may have a forced obliquity of $\sim 0.1^\circ$, which if present could result in surface stresses comparable in magnitude to those due to Europa's orbital eccentricity [*Hurford et al.*, 2006]. Those stresses are not considered here.

If NSR occurs, the satellite's equilibrium state consists of the rocky core and liquid ocean rotating synchronously with the orbital motion, but with the lithospheric shell rotating slightly faster than synchronously. We assume the NSR axis coincides with the axis of synchronous rotation, and so is perpendicular to the orbital plane. In this case, the angular rotation rate of the core and ocean is n , and the angular rotation rate of the floating shell is $n + b$, where b is the angular rate of NSR.

We attach a coordinate system to the outer surface of the shell, with the \hat{z} axis along the shell's rotation axis, and with the \hat{x} axis pointing toward the

parent planet at periapse (assumed to occur at time $t = 0$). The coordinate system rotates with the shell, and so its rotation rate is $n + b$. Let an arbitrary point in this coordinate system have the spherical coordinates r, θ, ϕ (radius, co-latitude, and eastward longitude, respectively). The tidal acceleration at (r, θ, ϕ) caused by the parent planet is the gradient of the tidal potential, $V_T(r, \theta, \phi)$. V_T can be expanded into spherical harmonics, as described in Appendix A of *Wahr et al.* [2009]. The result, when NSR is much slower than the diurnal rotation, is:

$$V_T(r, \theta, \phi, t) = Z \left(\frac{r}{R_s} \right)^2 [T_* + T_0 + T_1 + T_2] \quad (2.1)$$

where

$$T_* = \frac{1}{6}(1 - 3 \cos^2 \theta) \quad (2.2)$$

$$T_0 = \frac{1}{2} \sin^2 \theta \cos(2\phi + 2bt) \quad (2.3)$$

$$T_1 = \frac{\epsilon}{2}(1 - 3 \cos^2 \theta) \cos(nt) \quad (2.4)$$

$$T_2 = \frac{\epsilon}{2} \sin^2 \theta [3 \cos(2\phi) \cos(nt) + 4 \sin(2\phi) \sin(nt)] \quad (2.5)$$

Here, ϵ is the orbital eccentricity, R_s is the radius of the satellite, t is time relative to periapse, and the constant Z is:

$$Z = \frac{3GmR_s^2}{2a^3}, \quad (2.6)$$

with m being the mass of the planet, G Newton's gravitational constant, and a the semi-major axis of the satellite's orbit.

If the satellite's orbit is circular, so that $\epsilon = 0$. Then the tidal potential is represented entirely by $T_* + T_0$. If, in addition, there is no NSR (i.e. $b = 0$), then the potential is independent of time as seen from any point in the satellite. The potential would cause a permanent tidal bulge fixed to the satellite and pointing directly toward and away from the parent planet (there are outward tidal bulges on both sides of the satellite), but there would be no tidal shear stresses associated

with that bulge, since all stresses would have had an effectively infinite time to relax.

Non-synchronous rotation, on the other hand, causes the outer shell to rotate relative to the tidal potential with angular velocity = b , resulting in the $2bt$ time dependence shown in Eq. (2.3). The parent planet has longitude $\phi = -bt$ relative to our satellite-fixed coordinate system, and so Eq. (2.3) describes an elongated potential pointing directly toward and away from the planet. T_* is still time-independent, and thus does not cause shear stresses. However, because of the time dependence in T_0 , viscoelasticity within the outer shell would cause a time delay between when the shell passes through the V_T maximum, and when the shell fully deforms. Thus, the tidal bulge would not point directly toward the parent planet's center of mass, but (as we will show) would be offset from it by an amount that depends on the relationship between non-synchronous rotation rate and the viscous relaxation time.

The T_1 and T_2 terms in Eq. (2.1) represent the diurnal tidal potential. The amplitude of those terms is smaller than the NSR tidal potential by a factor of eccentricity (for Europa $\epsilon = 0.0094$). Thus, NSR stresses tend to be much larger than the diurnal stresses, unless the NSR period is very long compared to the relaxation time (as discussed in Section 2.4.1). T_1 and the $\cos(nt)$ term in T_2 cause the radial tide, and the $\sin(nt)$ term in T_2 causes the librational tide (see Section 2.2.2).

2.3.2 Relating the potential to elastic surface stresses

The vector field describing tidal displacements within the satellite $\vec{s}(r, \theta, \phi)$ can be derived from the applied tidal potential V_T , as in *Wahr* [1981] and *Wahr et al.* [2009]. The tidal potential V_T (Eq. (2.1)), is composed solely of second-degree spherical harmonics in (θ, ϕ) (T_* and T_1 have (degree, order) = (2,0), and

T_0 and T_2 have (degree, order) = (2,2)). We assume the equilibrium state of the satellite is spherically symmetric, and thus the material properties depend only on r (i.e. they are independent of θ and ϕ). This allows the surface displacements (at $r = R_s$) to be related to the potential via the two second-degree dimensionless Love numbers, h and ℓ (cf. [Munk and MacDonald, 1975; Lambeck, 1980]):

$$s_r(r = R_s, \theta, \phi, t) = \left(\frac{h}{g} \right) V_T \Big|_{r=R_s} \quad (2.7)$$

$$s_\theta(r = R_s, \theta, \phi, t) = \left(\frac{\ell}{g} \right) \frac{\partial V_T}{\partial \theta} \Big|_{r=R_s} \quad (2.8)$$

$$s_\phi(r = R_s, \theta, \phi, t) = \left(\frac{\ell}{g \sin \theta} \right) \frac{\partial V_T}{\partial \phi} \Big|_{r=R_s} \quad (2.9)$$

where g is the gravitational acceleration at the surface of the satellite. The Love number h describes the amplitude of the radial displacement (s_r), and ℓ describes both the southward (s_θ) and eastward (s_ϕ) lateral displacements.

Given $\vec{s}(r, \theta, \phi)$ we can then find the tidally induced stresses using the stress-displacement relationship:

$$\tau = \lambda (\nabla \cdot \vec{s}) + \mu [\nabla \vec{s} + (\nabla \vec{s})^T] \quad (2.10)$$

where τ is the stress tensor, and μ and λ are the Lamé parameters (μ is also known as the shear modulus), and the superscript T denotes transpose.

We are concerned in this work with modeling stresses at the satellite's outer surface. Since there can be no tidal surface tractions on the outer surface, $\tau_{rr} = \tau_{\theta r} = \tau_{\phi r} = 0$ when $r = R_s$. Since τ is symmetric, both $\tau_{r\theta}$ and $\tau_{r\phi}$ are also 0. Thus the only non-zero stress components at the surface are $\tau_{\theta\theta}$, $\tau_{\theta\phi} = \tau_{\phi\theta}$ and $\tau_{\phi\phi}$.

As detailed in Wahr *et al.* [2009], one may express these components in terms of the surface displacements, s_r , s_θ , and s_ϕ , and then use Eq. (2.7)-(2.9) to relate those results to the Love numbers h and ℓ and the tidal potential at the

surface, $V_T(r = R_s)$. Using Eq. (2.1) to write the tidal potential as a function of θ , ϕ , and t . The resulting stresses are:

$$\begin{aligned} \tau_{\theta\theta} = \frac{Z}{2gR_s} & \left[-\frac{1}{3}(\beta_1 + 3\gamma_1 \cos(2\theta)) + (\beta_1 - \gamma_1 \cos(2\theta)) \cos(2\phi + 2bt) \right. \\ & + 3\epsilon(\beta_1 - \gamma_1 \cos(2\theta)) \cos(nt) \cos(2\phi) - \epsilon(\beta_1 + 3\gamma_1 \cos(2\theta)) \cos(nt) \\ & \left. + 4\epsilon(\beta_1 - \gamma_1 \cos(2\theta)) \sin(nt) \sin(2\phi) \right] \end{aligned} \quad (2.11)$$

$$\begin{aligned} \tau_{\phi\phi} = \frac{Z}{2gR_s} & \left[-\frac{1}{3}(\beta_2 + 3\gamma_2 \cos(2\theta)) + (\beta_2 - \gamma_2 \cos(2\theta)) \cos(2\phi + 2bt) \right. \\ & + 3\epsilon(\beta_2 - \gamma_2 \cos(2\theta)) \cos(nt) \cos(2\phi) - \epsilon(\beta_2 + 3\gamma_2 \cos(2\theta)) \cos(nt) \\ & \left. + 4\epsilon(\beta_2 - \gamma_2 \cos(2\theta)) \sin(nt) \sin(2\phi) \right] \end{aligned} \quad (2.12)$$

$$\begin{aligned} \tau_{\phi\theta} = \tau_{\theta\phi} = \frac{2\ell Z \mu}{gR_s} & \left[-\cos\theta \sin(2\phi + 2bt) + 4\epsilon \sin(nt) \cos\theta \cos(2\phi) \right. \\ & \left. - 3\epsilon \cos(nt) \cos\theta \sin(2\phi) \right] \end{aligned} \quad (2.13)$$

where

$$\beta_1 = \mu[\alpha(h - 3\ell) + 3\ell] \quad (2.14)$$

$$\gamma_1 = \mu[\alpha(h - 3\ell) - \ell] \quad (2.15)$$

$$\beta_2 = \mu[\alpha(h - 3\ell) - 3\ell] \quad (2.16)$$

$$\gamma_2 = \mu[\alpha(h - 3\ell) + \ell] \quad (2.17)$$

and

$$\alpha = \frac{3\lambda + 2\mu}{\lambda + 2\mu} \quad (2.18)$$

Note that the first terms in Eq. (2.11) and (2.12) (i.e. those of the form $\frac{1}{3}(\beta + 3\gamma \cos(2\theta))$) lack any time dependence. Those stresses would not exist on a satel-

lite that has relaxed to a hydrostatic state. This relaxation is one of the consequences of viscoelasticity, discussed in the following section.

2.3.3 Introducing viscous relaxation

The stress results shown in Eq. (2.11)-(2.13) are derived under the assumption that the satellite behaves elastically. Moreover, the stress-displacement relation (Eq. (2.10)), and the relationships between the displacements and the tidal potential (Eq. (2.7)-(2.9)), all of which were used to derive the stress results, are valid only for an elastic rheology. A more appropriate model for the rheology of the satellite, particularly at the long periods characterizing NSR, is a Maxwell solid.

The correspondence principle [Peltier, 1974] can be applied to generalize the above results to a viscoelastic satellite by writing the sines and cosines with time-dependent arguments as sums of exponentials of the form $e^{i\omega t}$, where i is the imaginary number and ω is the frequency. For example, the NSR (T_0) term in Eq. (2.1) can be written equivalently as:

$$V_{T0} = Z \left(\frac{r}{R_s} \right)^2 \left(\frac{1}{4} \right) \sin^2 \theta [e^{i2\phi} e^{i2bt} + e^{-i2\phi} e^{-i2bt}] , \quad (2.19)$$

The correspondence principle for a Maxwell solid implies that if the tidal potential has a time dependence given by $e^{i\omega t}$, then the differential equations of motion remain unchanged, except that the elastic Lamé parameters μ and λ must be replaced by the complex quantities

$$\tilde{\mu}(\omega) = \mu \left(\frac{i\omega}{i\omega + \frac{\mu}{\eta}} \right) \quad (2.20)$$

$$\tilde{\lambda}(\omega) = \lambda \left(\frac{i\omega + \frac{\mu}{\eta} \left(\frac{2\mu+3\lambda}{3\lambda} \right)}{i\omega + \frac{\mu}{\eta}} \right) \quad (2.21)$$

where η is the viscosity [Peltier, 1974]. These choices for $\tilde{\mu}$ and $\tilde{\lambda}$ assume that viscoelastic relaxation occurs for shear stresses, but not for bulk stresses.

The Maxwell relaxation time is defined as $\tau_M = \eta/\mu$. The forcing period is $T = 2\pi/\omega$. For NSR, $\omega = 2b$ is twice the NSR rotation rate and so T is one half the shell's rotation period. Defining the dimensionless parameter Δ as:

$$\Delta \equiv \frac{T}{2\pi\tau_M} = \frac{\mu}{\eta\omega} \quad (2.22)$$

Eq. (2.20) and (2.21) become

$$\tilde{\mu}(\omega) = \mu \left(\frac{1}{1 - i\Delta} \right) \quad (2.23)$$

$$\tilde{\lambda}(\omega) = \lambda \left(\frac{1 - i\Delta \left(\frac{2\mu+3\lambda}{3\lambda} \right)}{1 - i\Delta} \right). \quad (2.24)$$

Because $\tilde{\mu}$ and $\tilde{\lambda}$ are now complex and frequency dependent, the tidal displacements and stresses, as well as the Love numbers, will also be complex and frequency dependent, with the Love numbers having the general form:

$$\tilde{h}(\omega) = h_{re}(\omega) + ih_{im}(\omega) \quad (2.25)$$

$$\tilde{\ell}(\omega) = \ell_{re}(\omega) + i\ell_{im}(\omega) \quad (2.26)$$

where h_{re} , h_{im} , ℓ_{re} , and ℓ_{im} are all real functions of frequency.

The significance of viscoelastic effects will depend on the value of Δ , which in turn depends on the ratio of the forcing period to the Maxwell time. If the forcing period is much shorter than the Maxwell time, then $\Delta \ll 1$, and the imaginary terms in Eq. (2.23) and (2.24) become negligible. In that case, $\tilde{\mu}(\omega) \approx \mu$ and $\tilde{\lambda}(\omega) \approx \lambda$ so that the effects of viscoelasticity are unimportant. In the other extreme, where the forcing period is much longer than the Maxwell time, then $\Delta \gg 1$, and so $\tilde{\mu}(\omega) \approx 0$ and $\tilde{\lambda}(\omega) \approx \lambda + 2\mu/3 =$ the elastic bulk modulus. Thus, at very long periods the material cannot support shear stresses, and so behaves as a fluid.

Applying the above substitutions to the elastic surface stresses, Eq. (2.11)-(2.13), we obtain the following expressions describing the stresses for a Maxwell rheology:

$$\begin{aligned} \tau_{\theta\theta} = \frac{Z}{2gR_s} Re & \left[\left(\tilde{\beta}_1(2b) - \tilde{\gamma}_1(2b) \cos(2\theta) \right) e^{i(2\phi+2bt)} \right. \\ & + 3\epsilon \left(\tilde{\beta}_1(n) - \tilde{\gamma}_1(n) \cos(2\theta) \right) e^{int} \cos(2\phi) \\ & - \epsilon \left(\tilde{\beta}_1(n) + 3\tilde{\gamma}_1(n) \cos(2\theta) \right) e^{int} \\ & \left. - 4\epsilon \left(\tilde{\beta}_1(n) - \tilde{\gamma}_1(n) \cos(2\theta) \right) i e^{int} \sin(2\phi) \right] \end{aligned} \quad (2.27)$$

$$\begin{aligned} \tau_{\phi\phi} = \frac{Z}{2gR_s} Re & \left[\left(\tilde{\beta}_2(2b) - \tilde{\gamma}_2(2b) \cos(2\theta) \right) e^{i(2\phi+2bt)} \right. \\ & + 3\epsilon \left(\tilde{\beta}_2(n) - \tilde{\gamma}_2(n) \cos(2\theta) \right) e^{int} \cos(2\phi) \\ & - \epsilon \left(\tilde{\beta}_2(n) + 3\tilde{\gamma}_2(n) \cos(2\theta) \right) e^{int} \\ & \left. - 4\epsilon \left(\tilde{\beta}_2(n) - \tilde{\gamma}_2(n) \cos(2\theta) \right) i e^{int} \sin(2\phi) \right] \end{aligned} \quad (2.28)$$

$$\begin{aligned} \tau_{\phi\theta} = \tau_{\theta\phi} = \frac{2Z}{gR_s} Re & \left[\tilde{\Gamma}(2b) i e^{i(2\phi+2bt)} \cos \theta - 4\epsilon \tilde{\Gamma}(n) i e^{int} \cos \theta \cos(2\phi) \right. \\ & \left. - 3\epsilon \tilde{\Gamma}(n) e^{int} \cos \theta \sin(2\phi) \right] \end{aligned} \quad (2.29)$$

where

$$\tilde{\beta}_1 = \tilde{\mu} \left[\tilde{\alpha}(\tilde{h} - 3\tilde{\ell}) + 3\tilde{\ell} \right] = \mu \left[\frac{\alpha(\tilde{h} - 3\tilde{\ell})}{1 - i\alpha\Delta/3} + \frac{3\tilde{\ell}}{1 - i\Delta} \right] \quad (2.30)$$

$$\tilde{\gamma}_1 = \tilde{\mu} \left[\tilde{\alpha}(\tilde{h} - 3\tilde{\ell}) - \tilde{\ell} \right] = \mu \left[\frac{\alpha(\tilde{h} - 3\tilde{\ell})}{1 - i\alpha\Delta/3} - \frac{\tilde{\ell}}{1 - i\Delta} \right] \quad (2.31)$$

$$\tilde{\beta}_2 = \tilde{\mu} \left[\tilde{\alpha}(\tilde{h} - 3\tilde{\ell}) - 3\tilde{\ell} \right] = \mu \left[\frac{\alpha(\tilde{h} - 3\tilde{\ell})}{1 - i\alpha\Delta/3} - \frac{3\tilde{\ell}}{1 - i\Delta} \right] \quad (2.32)$$

$$\tilde{\gamma}_2 = \tilde{\mu} \left[\tilde{\alpha}(\tilde{h} - 3\tilde{\ell}) + \tilde{\ell} \right] = \mu \left[\frac{\alpha(\tilde{h} - 3\tilde{\ell})}{1 - i\alpha\Delta/3} + \frac{\tilde{\ell}}{1 - i\Delta} \right] \quad (2.33)$$

$$\tilde{\Gamma} = \tilde{\mu}\tilde{\ell} = \frac{\mu\tilde{\ell}}{1 - i\Delta} \quad (2.34)$$

To derive the right-hand-sides of Eq. (2.30)-(2.33), we used

$$\tilde{\alpha} = \frac{3\tilde{\lambda} + 2\tilde{\mu}}{\tilde{\lambda} + 2\tilde{\mu}} = \alpha \left(\frac{1 - i\Delta}{1 - i\alpha\Delta/3} \right) \quad (2.35)$$

There are parameters μ , α , and Δ for each viscoelastic layer. The values for μ , α , and Δ that appear explicitly in Eq. (2.30)-(2.35) are those for the outer surface. Values in other layers (as well as in the surface layer) appear implicitly through their effects on \tilde{h} and $\tilde{\ell}$.

Focusing on just the NSR terms (the terms proportional to $e^{i(2\phi+2bt)}$ in Eq. (2.27)-(2.29)), since (as we shall see) the NSR stresses are more sensitive to viscoelastic effects than are the diurnal stresses:

$$\begin{aligned} \tau_{\theta\theta} &= \frac{Z}{2gR_s} \left[\left(\tilde{\beta}_{1re}(2b) - \tilde{\gamma}_{1re}(2b) \cos(2\theta) \right) \cos(2\phi + 2bt) \right. \\ &\quad \left. - \left(\tilde{\beta}_{1im}(2b) - \tilde{\gamma}_{1im}(2b) \cos(2\theta) \right) \sin(2\phi + 2bt) \right] \end{aligned} \quad (2.36)$$

$$\begin{aligned} \tau_{\phi\phi} &= \frac{Z}{2gR_s} \left[\left(\tilde{\beta}_{2re}(2b) - \tilde{\gamma}_{2re}(2b) \cos(2\theta) \right) \cos(2\phi + 2bt) \right. \\ &\quad \left. - \left(\tilde{\beta}_{2im}(2b) - \tilde{\gamma}_{2im}(2b) \cos(2\theta) \right) \sin(2\phi + 2bt) \right] \end{aligned} \quad (2.37)$$

$$\tau_{\phi\theta} = \tau_{\theta\phi} = -\frac{2Z}{gR_s} \cos \theta \left[\tilde{\Gamma}_{re}(2b) \sin(2\phi + 2bt) + \tilde{\Gamma}_{im}(2b) \cos(2\phi + 2bt) \right] \quad (2.38)$$

where the subscripts *re* and *im* denote the real and imaginary parts; and where, for example, $\tilde{\beta}_{1re}(2b)$ denotes the real part of $\tilde{\beta}_1$, with $\omega = 2b$ used to evaluate \tilde{h} , $\tilde{\ell}$, and Δ .

2.4 A qualitative description of NSR stresses

To better understand the effects of viscous relaxation on the NSR tidal deformations, we consider the behavior of a satellite in three cases: the fluid limit ($\Delta \gg 1$), the elastic limit ($\Delta \ll 1$), and a truly viscoelastic scenario ($\Delta \approx 1$). For

illustrative purposes, we focus on Jupiter's moon Europa, using the parameter values listed in Table 2.1, and we assume the core is synchronously locked.

2.4.1 NSR tides in the fluid limit ($\Delta \gg 1$)

First suppose the NSR period is much longer than the viscoelastic timescale of the floating ice shell, so that $\Delta \gg 1$. In that case $\tilde{\mu}$ is small, and so the shell deforms in response to the NSR tidal forcing nearly as though it were a fluid. Since the rocky core is presumed to be rotating synchronously, it keeps the same face constantly pointing toward the parent planet, and the tidal force at every point in the rocky core never changes: the tidal potential in the rocky core is given by Eq. (2.2) and (2.3) with $b = 0$. Since the core's viscosity is presumably finite, its shear stresses have had sufficient time to completely relax, and so its tidal response is the same as if it were a perfect fluid. Since the icy shell is assumed to also behave as a fluid in this $\Delta \gg 1$ limit, and the ocean actually *is* a fluid, both the icy shell and the rocky core are stretched into ellipsoids oriented toward and away from the parent planet, with amplitudes consistent with the assumption of a completely fluid satellite. Because of the NSR, fixed points in the icy shell are slowly rising and falling as they rotate through the bulge, but there are no induced shear stresses in the shell because $\tilde{\mu} = 0$ in Eq. (2.30)-(2.34), meaning that $\tau_{\theta\theta} = \tau_{\phi\phi} = \tau_{\phi\theta} = \tau_{\theta\phi} = 0$ in Eq. (2.36)-(2.38).

2.4.2 NSR tides in the elastic limit ($\Delta \ll 1$)

Next, suppose the NSR period is much shorter than the relaxation timescale of the icy shell, so that $\Delta \ll 1$. In that case $\tilde{\mu} \approx \mu$, and the shell behaves approximately elastically. The shell responds instantaneously to tidal forces, and so the orientation of the tidal bulge is still symmetric about the line to the planet, but now the shell supports shear stresses which try to hold back the bulging fluid

Table 2.1: Viscoelastic Model Parameters (Figs. 2.1, 2.3, and 2.4)

Parameter	Symbol	Value
Mass of Europa	M_E	4.8×10^{22} kg
Mass of Jupiter	M_p	1.8987×10^{27} kg
Radius of Europa	R_s	1.561×10^6 m
Europa's surface gravity	g	1.315 m s $^{-2}$
Europa's orbital semi-major axis	a	6.709×10^8
Eccentricity of orbit	ϵ	9.4×10^{-3}
Thickness of stagnant lid	D_{upper}	8×10^3 m
Viscosity of stagnant lid	η_{upper}	10^{22} Pa s
Thickness of convecting ice	D_{lower}	1.2×10^4 m
Viscosity of convecting ice	η_{lower}	10^{17} Pa s
Density of ice	ρ_{ice}	940 kg m $^{-3}$
Bulk modulus of ice ($= \lambda_{ice} + \frac{2}{3}\mu_{ice}$)	κ_{ice}	9.3×10^9 Pa
Shear modulus of ice	μ_{ice}	3.487×10^9 Pa
Thickness of ocean	D_{ocean}	1.5×10^5 m
Density of ocean	ρ_{ocean}	10^3 kg m $^{-3}$
Bulk modulus of ocean	κ_{ocean}	2×10^9 Pa
Density of silicate interior	ρ_{core}	3.8476×10^3 kg m $^{-3}$
Bulk modulus of core	κ_{core}	6.67×10^{10} Pa
Shear modulus of core	μ_{core}	4×10^{10} Pa
Complex Love numbers	$\tilde{h}, \tilde{\ell}$	see Tables 2.2 and 2.3

Table 2.2: Diurnal Love Numbers for Europa

Fig.	P_{orbit}	$h_{D,re}$	$h_{D,im}$	$\ell_{D,re}$	$\ell_{D,im}$
2.3a-d	3.55 days	1.192	-6.293×10^{-5}	0.3094	-2.903×10^{-5}
2.5a	n/a	1.2753	n/a	0.31882 ($\equiv \frac{h}{4}$)	n/a
2.5b	3.55 days	1.234	0.0	0.3228	0.0

Table 2.3: NSR Love Numbers for Europa

Fig.	P_{NSR}	$h_{N,re}$	$h_{N,im}$	$\ell_{N,re}$	$\ell_{N,im}$
2.4a	1.422×10^5 yr	1.813	-4.186×10^{-3}	0.4748	-2.766×10^{-3}
2.4b	1.422×10^6 yr	1.834	-2.235×10^{-2}	0.4884	-1.487×10^{-2}
2.4c	1.422×10^7 yr	1.857	-4.795×10^{-3}	0.5038	-4.883×10^{-3}
2.4d	1.422×10^8 yr	1.858	-1.334×10^{-3}	0.5095	-1.643×10^{-2}
2.5c	n/a	1.2753	n/a	0.31882 ($\equiv \frac{h}{4}$)	n/a
2.5d	6.334×10^7 yr	1.860	-8.597×10^{-4}	0.5047	-2.180×10^{-3}

ocean, and so the shell's displacement is smaller than in the $\Delta \gg 1$ case. However, as long as the shell is thin (i.e. its thickness is much smaller than the satellite's radius) it has only a minimal effect on the tidal bulge (see [Moore and Schubert, 2000; Wu *et al.*, 2001; Wahr *et al.*, 2006; Rappaport *et al.*, 2008]), and so the displacements are not affected much by the strength of the shell (i.e. the Love numbers \tilde{h} and $\tilde{\ell}$ are relatively insensitive to the value of Δ). Fixed points in the shell still rise and fall as they non-synchronously rotate through the bulge, and since $\tilde{\mu}$ is no longer small this periodic motion now results in significant shear stress within the shell. That shear stress is trying (but failing) to confine the ocean. The shear stress is symmetrically distributed about the satellite-planet vector, since the shell is responding instantaneously. The rocky core is still oriented toward the parent planet; it does not participate in the NSR, and so the forcing remains constant at every point in the core. Thus the core still responds to the tidal force as though it were a fluid.

2.4.3 NSR tides in a truly viscoelastic case ($\Delta \approx 1$)

Finally, consider an intermediate case where the NSR period and the viscous relaxation times are approximately equal (i.e. $\Delta \approx 1$). The icy shell still holds back the ocean slightly since the shell can partially support shear stresses, but because the shell is viscous it does not respond instantaneously to the tidal force. By the time a portion of the shell experiences its maximum displacement, it has rotated slightly beyond the satellite-planet vector. Thus, the bulge in the icy shell is slightly ahead of the satellite-planet vector. The impact of these shear stresses on the shell's displacement is still small, assuming the thickness of the shell is small relative to the radius of the satellite.

Figures 2.1a and 2.1b show how the real and imaginary parts of the Love numbers vary with Δ . Notice that the real parts of the Love numbers are about

the same for all values of Δ , and the imaginary parts are always small. Thus the shell's tidal bulge is still closely aligned with the satellite-planet vector. The shell, in effect, still mostly just rides up and down on the underlying ocean during its non-synchronous rotation. Its tidal displacement field is determined almost entirely by the shape of the ocean surface, and has little dependence on the shell's rheological properties.

The shell's rheology does have a significant impact on the shear stresses caused by that displacement field. Viscoelasticity in the shell can cause the shear stresses to be offset from the satellite-planet vector by up to $\sim 45^\circ$. For example, when $\Delta \approx 1$, $\tilde{\mu}$ and $\tilde{\alpha}$ in Eq. (2.30)-(2.34) have real and imaginary parts that are of the same order, and so they cause $\tilde{\beta}_1$, and the other complex coefficients to have significant imaginary parts even though (for a thin shell) the Love numbers \tilde{h} and $\tilde{\ell}$ are almost real (Fig. 2.1c and 2.1d show how the real and imaginary parts of $\tilde{\mu}$ and $\tilde{\lambda}$ vary with Δ .)

A perhaps counterintuitive result is that the stress pattern ends up being shifted in the direction opposite of the shell's rotation, rather than in the same direction. This can be seen by noting that the real and imaginary parts of Eq. (2.30)-(2.34) have the same sign, for \tilde{h} and $\tilde{\ell}$ real. The stress pattern shifts in this direction because Maxwell viscoelasticity causes the maximum displacement to occur after the maximum stress. Thus since the ocean-imposed displacement field is oriented toward the parent planet, the stress pattern is shifted in the direction the shell has rotated from. Once again, because the core is synchronously rotating, the forcing is constant at every point in the core and so the core still responds as though it were a fluid.

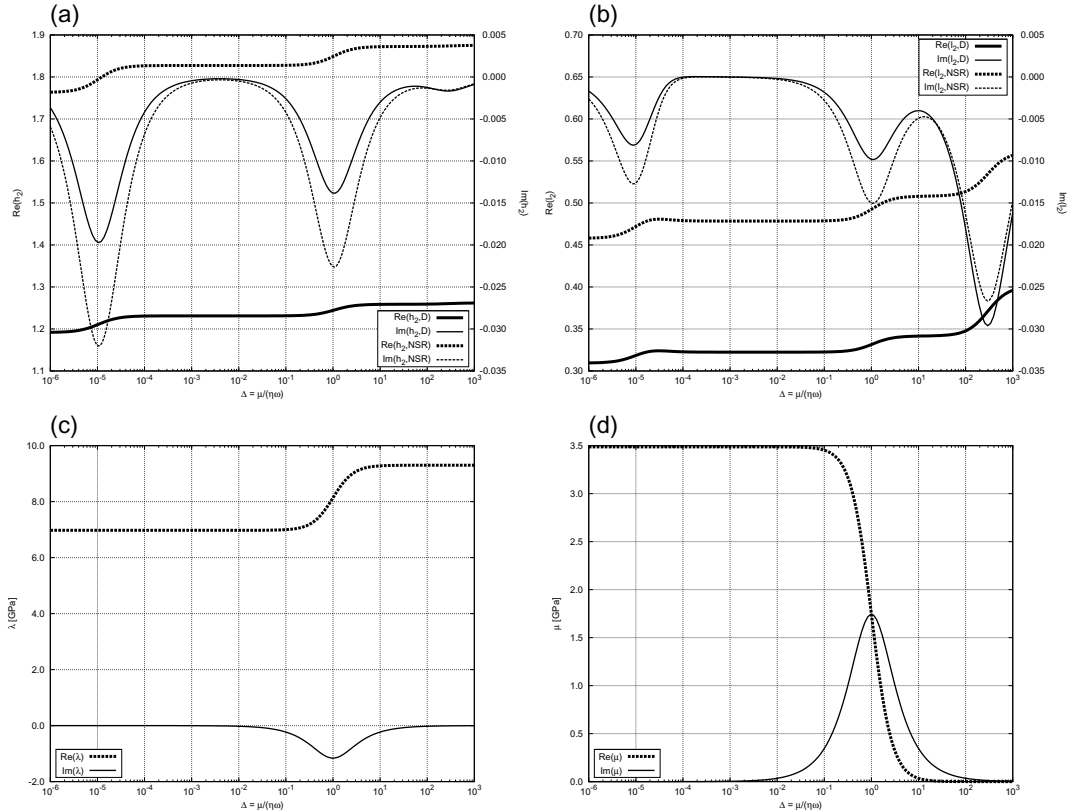


Figure 2.1: The complex Love numbers \tilde{h}_2 (a) and $\tilde{\ell}_2$ (b). The dashed curves are calculations in which the silicate core has a nearly fluid response, appropriate to NSR (see section 2.5). The solid curves indicate a core having a nearly rigid response, appropriate to the diurnal forcing. Imaginary parts are thin curves, tied to the right axes; real parts are thick curves, tied to the left axes. The upper shell's complex Lamé parameters $\tilde{\lambda}$ (c) and $\tilde{\mu}$ (d). Thick dashed curves correspond to real parts and thin solid curves are the imaginary parts. See section 2.6.1 for discussion. All plots use the parameters listed in Table 2.1, and a range of forcing frequencies ω , represented here by the parameter Δ which represents the value of Δ in the upper layer.

2.5 Numerical method, and a complication due to the core

For our numerical calculations we consider a satellite composed of four homogeneous compressible layers: a rocky core, an overlying fluid ocean, and a viscoelastic outer icy shell with a stiff upper layer (representing a conductive stagnant lid) and a low-viscosity basal layer (representing a possible convective region).

We recognize that the very cold surface layer of the ice shell will behave as a brittle-plastic material (e.g. [*Dombard and McKinnon, 2006*]) rather than viscously even on very long timescales, and whatever effect this near-surface layer has on the surface stresses is thus not accounted for in this model. However, if the fractured layer of the satellite extends to depths at which viscoelastic deformation occurs on the timescale of NSR, then our model should provide an accurate representation of the stresses at that depth.

In this example we choose the ice shell to be thin compared to the satellite's radius, but this is not a requirement of the method; it can be applied equally well to a satellite with a thick outer shell, or even to a satellite with no liquid ocean at all.

Our numerical method is based on standard algorithms used by geophysicists to compute tides on the Earth, and involves a modified version of the code used by [*Dahlen, 1976*] to compute terrestrial tides (see also, [*Wahr et al., 2006; Rappaport et al., 2008*]). We have modified this code to include complex rheological parameters and complex solution scalars, so that we can accommodate a Maxwell solid rheology. The diurnal and NSR solutions differ solely through the frequency-dependence of the Lamé parameters, as shown in Eq. (2.20)-(2.21). Once we have determined the complex Love numbers, \tilde{h} and $\tilde{\ell}$, they are used as described in Section 2.3.3 to find the surface stresses.

In the formulation of the model described above, we assume the coordinate system is attached to the icy shell and so rotates with it. However, in the case of NSR it is only the icy shell that rotates non-synchronously; the rocky core likely remains synchronously locked to the satellite’s orbital motion [*Greenberg and Weidenschilling, 1984*]. From the perspective of points in the icy shell, which is the region of most interest to this study, the external gravity field changes partly because the shell is rotating through the parent planet’s gravity field, and partly because the shell is rotating through the gravity field caused by the underlying core. At points within the rocky core, on the other hand, the gravity field never changes, and so as described in section 2.4, the core always responds to the NSR tidal forcing as though it were a fluid.

To obtain an adequate representation of the shape of the core and its effects on the icy shell, we set $\mu \approx 0$ in the rocky core when solving for the NSR tides. This eliminates shear stresses in the core, leading to much larger core tidal displacements. This in turn significantly increases the displacements and shear stresses in the icy shell, since then the gravity field from the core’s tidal bulge can be a much larger fraction of the direct gravity field from the parent planet. On Europa for example, setting $\mu \approx 0$ in the core can increase the displacements and shear stresses in the icy shell by up to 70%. This difference in the assumed behavior of the core under the diurnal and NSR forcings is why there are two sets of each of the Love numbers displayed in Fig. 2.1a and 2.1b.

2.6 Results

Our formulation of the equations of motion and the resulting stresses describes the effects of viscoelasticity in terms of the parameter Δ , which is proportional to the ratio between the forcing period and the Maxwell relaxation time of the ice. Because the shell we are considering has two viscoelastic layers with dif-

ferent viscosities, it will also have two values of Δ for a given forcing period. The resulting stresses at the outer surface (Eq. (2.27)-(2.29)) depend on those values in two ways:

- (i) they depend on the Δ values of each ice layer through the Love numbers h and \tilde{h} ; and
- (ii) they depend on Δ of the upper icy layer only, through $\tilde{\beta}_1$, $\tilde{\gamma}_1$, $\tilde{\beta}_2$, $\tilde{\gamma}_2$, and $\tilde{\Gamma}$.

Item (i) represents the effects of viscoelasticity on the surface displacements, whereas (ii) describes how those displacements translate into stresses within a viscoelastic medium (with the properties of the upper ice layer). The dependence (i) is weak so long as there is an underlying ocean and the ice shell is thin (relative to the radius of the satellite), as we are assuming in this application. Δ does have a large relative effect on the imaginary parts of the Love numbers, but the imaginary parts are only a small fraction of the real parts. The tidal response in this case is mostly determined by the ocean, and so the Love numbers are only weakly dependent on the properties of the ice shell (see [Moore and Schubert, 2000; Wu *et al.*, 2001; Wahr *et al.*, 2006; Rappaport *et al.*, 2008]). Thus, the primary influence of viscous effects comes through (ii).

2.6.1 Love numbers

The effects of viscoelasticity on the real and imaginary parts of the Love numbers are shown in Fig. 2.1a and 2.1b, for values of Δ (at the outer surface) spanning nine orders of magnitude. Values of $\Delta \ll 1$ indicate a forcing period short enough that the shear stresses do not have time to relax during a forcing cycle, and so the material behaves nearly elastically. Values of $\Delta \gg 1$ imply a long enough forcing period that the stresses have time to almost completely relax, allowing the material to behave almost as an inviscid fluid.

The results shown in these figures are computed using the upper and lower viscosity values η_{upper} and η_{lower} shown in Table 2.1, and varying the forcing period. The elastic value of μ , given in Table 2.1, is assumed to be the same in each layer. Thus, the results are computed assuming the values of Δ in the lower and upper layers are related by a factor of $\Delta_{lower}/\Delta_{upper} = \eta_{upper}/\eta_{lower} = 10^5$. We would have obtained the same results if we had fixed the forcing period and varied the viscosities of the layers in tandem (i.e. maintaining $\eta_{upper}/\eta_{lower} = 10^5$).

Results are shown both for the diurnal tides, where the period is well known but the viscosity is not, and for the NSR tides, where neither the period nor the viscosity is known. The difference between the diurnal and NSR results at any given value of Δ is because in the NSR case we assume the silicate core behaves as a fluid, and in the diurnal case we assume it behaves elastically. As described in Section 2.5, this causes the NSR Love numbers to be about 70% larger than the diurnal Love numbers for a fixed value of Δ .

Figures 2.1a and 2.1b show that the real parts of the Love numbers (thick lines, tied to left axes) are one to two orders of magnitude larger than the imaginary parts (thin lines, right axes) no matter what value is assumed for Δ . This is because the icy lithosphere is thin and so has only a small impact on the surface displacements regardless of whether it is viscoelastic or not. For the same reason, the real parts of the Love numbers vary by only $\sim 10\%$ over this entire range of Δ . This is important because the viscosity profile beneath the very outermost ice layer can perturb the surface stresses only through its effects on the Love numbers, and the figures show that those effects are likely to be no larger than $\sim 10\%$. Thus there is little additional accuracy to be gained by including a more complicated internal viscosity structure in the shell.

Figures 2.1a and 2.1b also show dips in the values of the imaginary parts of the Love numbers when $\Delta \approx 1$ and $\approx 10^{-5}$, with associated step function increases

in the real parts. The $\Delta \approx 1$ features reflect the transition from elastic-like to fluid-like behavior in the outer shell, as Δ transitions between < 1 and > 1 . These features result from similar behavior in the imaginary and real parts of $\tilde{\mu}$ and $\tilde{\lambda}$ of the outer shell evident in Fig. 2.1c and 2.1d. The features at $\Delta \approx 10^{-5}$ are due to a similar elastic-to-fluid transition in the lower ice layer: a value of $\Delta = 10^{-5}$ in the upper layer implies $\Delta = 1$ in the lower layer because we have chosen to fix the ratio $\eta_{upper}/\eta_{lower} = 10^5$.

There are also dips in the imaginary parts of the Love numbers at $\Delta \approx 300$, and corresponding step functions in the real parts. These features, which are far more prominent for the Love number $\tilde{\ell}$ than for \tilde{h} , represent the effects of an additional relaxation mode of the system, a mode with a relaxation time that is considerably longer than the Maxwell times of the ice layers. This situation is analogous to the post-glacial-rebound process on the Earth. Viscoelastic models of the Earth exhibit a large suite of relaxation modes. Some directly correspond to Maxwell times. Others, referred to as buoyancy modes, have longer periods and involve radial perturbations of density discontinuities. The $\Delta \approx 300$ mode evident in Fig. 2.1a and 2.1b corresponds to the viscoelastic mode usually referred to as C0 in the post-glacial-rebound literature, associated with the relaxation of the Earth's core-mantle boundary (e.g. [Peltier, 1985]). When the ocean/shell boundary is displaced from an equipotential surface, there is a gravitational (buoyancy) force that acts to restore it. This force is opposed by viscous resistance within the shell. Although this contribution to the viscoelastic Love numbers is interesting from a dynamical viewpoint, its impact on the surface stresses is minimal because the Love numbers play only a secondary role in determining the viscoelastic contributions to the surface stresses. However, it does cause the maximum phase shift to slightly exceed 45° when $\Delta \gg 1$, as can be seen in Fig. 2.2a. Reducing the density contrast between the ice and the ocean reduces the buoyancy force,

and increases the timescale on which these forces have an effect, pushing both the large dip in the imaginary part of $\tilde{\ell}$, and the increase in phase shift to values greater than 45° , out to larger Δ values.

2.6.2 The direct effects of the outer layer's viscosity

Viscous effects influence the surface stresses most through the Lamé parameters $\tilde{\mu}$ and $\tilde{\lambda}$ of the upper shell, and their impact on the parameters $\tilde{\beta}_1$, $\tilde{\gamma}_1$, $\tilde{\beta}_2$, $\tilde{\gamma}_2$, and $\tilde{\Gamma}$ (Eq. (2.30)-(2.34)). The surface stress components (Eq. (2.27)-(2.29)) are proportional to those last five parameters, and each of those parameters is proportional to $\tilde{\mu}$ of the outer surface. All except $\tilde{\Gamma}$ also depend on $\tilde{\lambda}$, but that dependence is not very strong. Figures 2.1c and 2.1d show the Lamé parameters as functions of Δ . Over the range of Δ considered here, $\tilde{\mu}$ varies enormously (from zero to 3.5×10^9 Pa) but $\tilde{\lambda}$ varies by only $\sim 30\%$ (from ~ 7 to $\sim 9 \times 10^9$ Pa). This variability, combined with the direct influence of $\tilde{\mu}$ on all of the parameters listed above, implies that the Δ dependence of $\tilde{\mu}$ will strongly and directly impact the surface stresses.

Note from Eq. (2.23) that $\text{Im}(\tilde{\mu})/\text{Re}(\tilde{\mu}) = \Delta$. Thus when $\Delta \ll 1$ the imaginary part is small relative to the real part, and when $\Delta \gg 1$ it is large (though both the real and imaginary parts vanish as $\Delta \rightarrow \infty$). When the real and imaginary parts are of comparable magnitude (i.e. $0.1 < \Delta < 10$), $\tilde{\mu}$ departs significantly from either the fluid or elastic limits. All of these characteristics of $\tilde{\mu}$ get passed through directly to the stress components. The value of Δ at the outer surface thus becomes critical in determining the surface stresses.

For the diurnal tides, assuming a plausible value for the viscosity of cold surface ice of 10^{22} Pa s (Table 2.1), Δ in the upper layer is roughly 2×10^{-8} , which means the effects of viscoelasticity can be safely ignored. The outer surface viscosity would have to be as small as 2×10^{15} Pa s for Δ to be as large as 0.1,

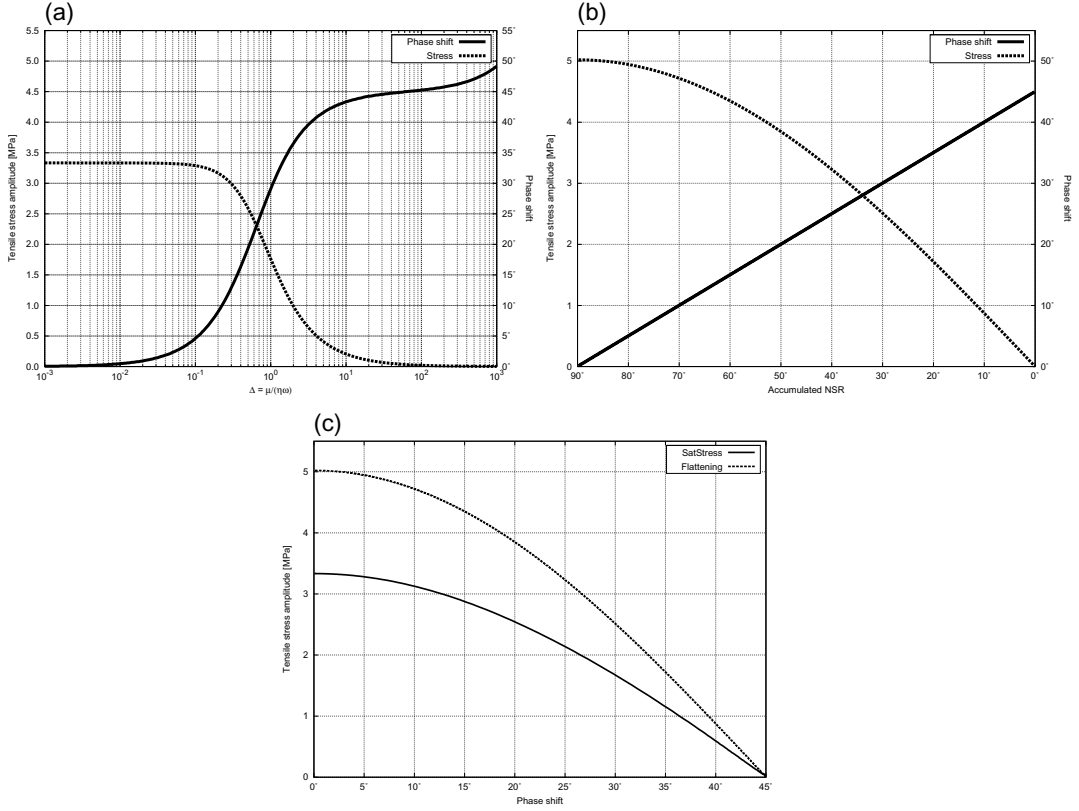


Figure 2.2: (a) NSR results from our viscoelastic model. Shown are the amplitude and phase shift of the maximum tensile stress as a function of Δ . The viscoelastic stress field experiences a phase shift $> 45^\circ$ for large values of Δ because of the effect the ice shell's buoyancy mode has on the imaginary part of the Love number $\tilde{\ell}$ for values of $\Delta \approx 300$ (see Fig. 2.1b, and discussion in Section 2.6.1.) If the density contrast between the ice and the ocean is reduced, this upturn moves out to larger values of Δ , as does that feature in $\tilde{\ell}$. (b) Similar to (a), with accumulated degrees of NSR for the flattening model (which we compare to in section 2.7) along the x-axis. (c) Because the variables that the two models use to determine the phase shift and stress amplitudes are different (Δ for the viscoelastic model, accumulated NSR for flattening), it is useful to compare the amplitudes as functions of the phase shift. The two curves are related by a nearly constant multiplier of ~ 1.5 , with the flattening model predicting larger amplitudes for an identical amount of phase shift. At phase shifts of $\approx 45^\circ$ (implying small stress amplitudes), this multiplicative relationship breaks down, with the amplitude of viscoelastic stresses eventually exceeding that of the flattening stresses.

which is roughly when viscous effects start to become important. A viscosity of 2×10^{15} Pa s may be reasonable for the warm lower ice layer, but as described above, the lower layer Δ has only a minimal impact on the surface stresses, no matter its value. The implication is that viscoelastic effects are not likely to have a significant effect on the diurnal tidal stresses.

For the NSR tides (again assuming the outer layer viscosity is 10^{22} Pa s), if the NSR period is between 1.2×10^5 and 1.2×10^7 yr, then Δ is in the range $0.1 < \Delta < 10$ where viscoelastic effects are important and are very sensitive to Δ . If the NSR period is significantly longer than 1.2×10^7 yr, then $\Delta \gg 1$, and the surface stresses are small: they decay away almost as quickly as the forcing can create them.

However, even relatively small NSR stresses can overwhelm the diurnal stresses. The diurnal tides arise because of the orbital eccentricity ϵ , and cause displacements that are ϵ ($= 0.0094$ for Europa) times as large as the NSR displacements. Thus, if the ice layer was elastic, the diurnal stresses would similarly be a factor of ϵ times smaller than the NSR stresses. Viscoelasticity reduces the NSR stress magnitudes as Δ increases (i.e. as the NSR period gets longer). For $\Delta \gg 1$, the parameters $\tilde{\beta}_1$, $\tilde{\gamma}_1$, $\tilde{\beta}_2$, $\tilde{\gamma}_2$, and $\tilde{\Gamma}$ in Eq. (2.30)-(2.34) become approximately inversely proportional to Δ . The elastic case is given by those same expressions, but with $\Delta = 0$. Thus, in order for the amplitudes of the NSR stresses to be reduced to where they are comparable or smaller than the diurnal amplitudes, Δ has to be on the order of $1/\epsilon$ or larger (~ 100 for Europa). For an outer layer viscosity of 10^{22} Pa s, an NSR period of $\sim 1.2 \times 10^8$ yr or longer is required for diurnal stresses to dominate NSR stresses.

2.6.3 Stress patterns and phase shifts

The value of Δ is critical for determining not only the magnitude of the surface stresses, but also how those stresses are distributed over the surface of the satellite. The smaller the value of Δ , the closer the shell's response is to being elastic, and so the closer the stresses are to being oriented symmetrically about the planet-satellite vector – a state we will refer to as having zero phase shift.

For the diurnal tides, Δ is so small that the resulting stresses are virtually elastic (see above). If the default viscosity values given in Table 2.1 are altered such that the entire shell has the high viscosity of the surface (10^{22} Pa s), the amplitude of the diurnal component of the stresses changes by less than 0.1%. If the the entire low viscosity portion of the shell is replaced with ocean, leaving only an 8 km thick high-viscosity upper shell, the difference in the amplitude of the diurnal component of the stresses is $\sim 3\%$. Maps of the diurnal stresses at different points in the orbit (i.e. at different values of nt in Eq. (2.27)-(2.29)) are shown in Fig. 2.3. In these plots, the sub-Jovian point at perijove is at latitude (y-axis) 0° , longitude (x-axis) 0° .

For the NSR tides the value of the period is unknown. Both the amplitude and the phase shift of the stresses depend on that period, mostly through the direct dependence on Δ of the outer surface. The parameters $\tilde{\beta}_1$, $\tilde{\gamma}_1$, $\tilde{\beta}_2$, $\tilde{\gamma}_2$, and $\tilde{\Gamma}$ (Eq. (2.30)-(2.34)) are proportional to $\tilde{\mu}$, and $\tilde{\mu}$ depends on Δ through (2.23). Thus, the right-hand-sides of Eq. (2.30)-(2.34) show that when $\Delta \ll 1$ the parameters $\tilde{\beta}_1$, $\tilde{\gamma}_1$, $\tilde{\beta}_2$, $\tilde{\gamma}_2$, and $\tilde{\Gamma}$ are nearly real and are well approximated by their elastic values (since \tilde{h} and \tilde{l} are nearly equal to their elastic values).

When $\Delta \gg 1$, those five parameters have small amplitudes, but their imaginary parts are a factor of Δ larger than their real parts (for example, $1/(1 - i\Delta) = (1 - i\Delta)/(1 + \Delta^2)$, has real and imaginary parts of approximately

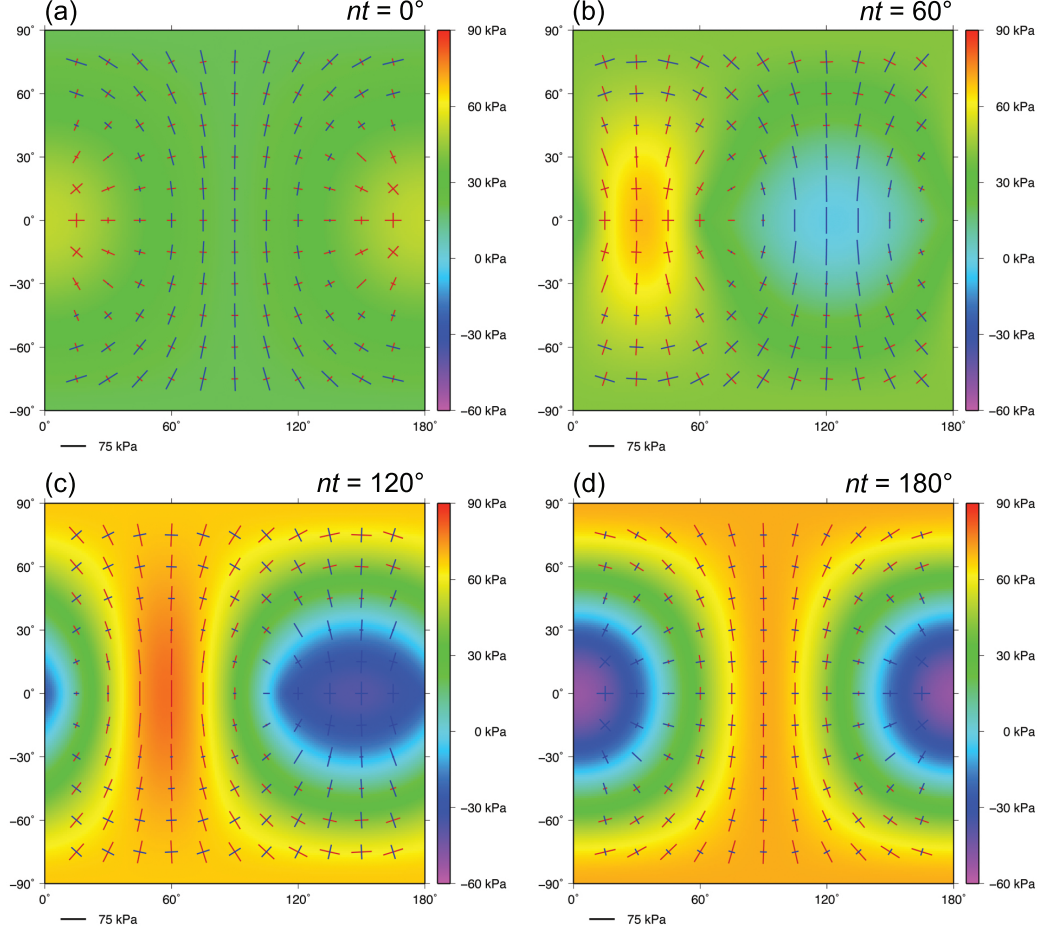


Figure 2.3: Diurnal stress results for Europa from the viscoelastic model, at different orbital locations, measured from perijove (nt in Eq. (2.27)-(2.29)), using parameters from Table 2.1. The sub-Jovian point at perijove is at latitude (y-axis) 0° , longitude (ϕ , x-axis) 0° . East is taken as positive. Results for $180^\circ < \phi < 360^\circ$ are the same as those between 0° and 180° : $\tau(\phi) = \tau(\phi + 180^\circ)$. Stresses in the second half of the orbit ($180^\circ < nt < 360^\circ$) are east-west reflections of those in the first half. Tic marks show the magnitude and orientation of the principal components of the stresses on the surface of the satellite. Compression (blue) is negative and tension (red) is positive. Background color shows the magnitude of the most tensile of the two principal components, as indicated by the color scales shown to the right of each panel.

Δ^{-2} and Δ^{-1} respectively, when $\Delta \gg 1$). This means that while $\tau_{\theta\theta}$ is proportional to $\cos(2\phi + 2bt)$ in the elastic limit, it is nearly proportional to $\sin(2\phi + 2bt)$ in the $\Delta \gg 1$ limit (see Eq. (2.36)). The factors of 2 in $(2\phi + 2bt)$ mean that the spatial pattern of $\tau_{\theta\theta}$ in the $\Delta \gg 1$ limit is displaced from the elastic pattern by 45° . The same is true of the other stress components, $\tau_{\phi\phi}$ and $\tau_{\phi\theta}$.

In general the patterns and amplitudes of the tidally induced surface stresses can be separated into 4 possible regimes. If the orbital eccentricity ϵ is small and the shell is thin, and assuming for the case of Europa that the viscosity of the upper layer of the ice is $\eta_{upper} = 10^{22}$ Pa s, we find:

(a) **$\Delta < 0.1$** . The NSR stress is nearly elastic, and so has a phase shift of $\sim 0^\circ$.

The NSR stress amplitude is a factor of $\sim \epsilon^{-1}$ times larger than the diurnal stress amplitude. For our nominal Europa, this corresponds to an NSR period (P_{nsr}) of less than 1.2×10^5 yr, and tensile NSR stresses of up to ~ 3.2 MPa.

(b) **$0.1 < \Delta < 10$** . The NSR stress amplitude is still much larger than that of the diurnal stress, but it varies rapidly through this range of Δ values (for Europa the NSR stress amplitude decreases from ~ 3.2 MPa to ~ 500 kPa as Δ increases). The phase shift varies from $\sim 0^\circ$ at $\Delta = 0.1$, to $\sim 45^\circ$ at $\Delta = 10$. For Europa this corresponds to $1.2 \times 10^5 < P_{nsr} < 1.2 \times 10^7$ yr.

(c) **$10 < \Delta < \epsilon^{-1} (\approx 100)$** . The amplitude of the NSR stress has relaxed significantly, but is still as large or larger than that of the diurnal stress. The phase shift of the NSR stress pattern is $\sim 45^\circ$. For Europa this corresponds to $1.2 \times 10^7 < P_{nsr} < 1.2 \times 10^8$ yr, and results in the maximum tensile stress being reduced from ~ 500 kPa to ~ 50 kPa as Δ increases through this range of values.

(d) $\Delta > \epsilon^{-1} (\approx 100)$. The amplitude of the NSR stress is smaller than that of the diurnal stress, becoming much smaller as $\Delta \rightarrow \infty$. The phase shift of the NSR stresses remains constant at $\sim 45^\circ$. However, for $\Delta \gg \epsilon^{-1}$ this becomes irrelevant after combining the NSR and diurnal stresses, because the NSR stress is overwhelmed by the diurnal stress. For Europa this corresponds to $P_{nsr} > 1.2 \times 10^8$ years.

These points are illustrated in Fig. 2.4, which shows NSR stresses for different values of Δ . The maps show the stress results Eq. (2.36)-(2.38) evaluated at time $t = 0$. At any time t , NSR would cause the sub-Jovian point at be at longitude $\phi = -bt$ relative to the Europan surface. Thus, these maps can also be interpreted as showing the surface stresses at any time, relative to a sub-Jovian point at latitude (y-axis) 0° and longitude (x-axis) 0° .

In the case of Europa, it is not yet possible to determine which of the above regimes is appropriate. All four are possible given current uncertainty in the NSR period and the range of plausible near-surface ice viscosities.

2.6.4 Geological implications of viscoelasticity

Attempts have been made to correlate lineaments on Europa with the NSR stress field by translating them longitudinally [Hoppa *et al.*, 2001; Kattenhorn, 2002; Hurford *et al.*, 2007; Figueiredo and Greeley, 2000]. The amount of translation required to get a good fit between a lineament and the stress field has been used as a proxy for the time elapsed since formation. The underlying assumption is that they formed at one longitude and, as the shell underwent NSR, they came to be located at another. This is only straightforward if the stress field is fixed with respect to the planet-satellite vector and has a known phase shift (previously assumed to be $\sim 45^\circ$). Because Δ can affect the phase shift of the NSR stresses,

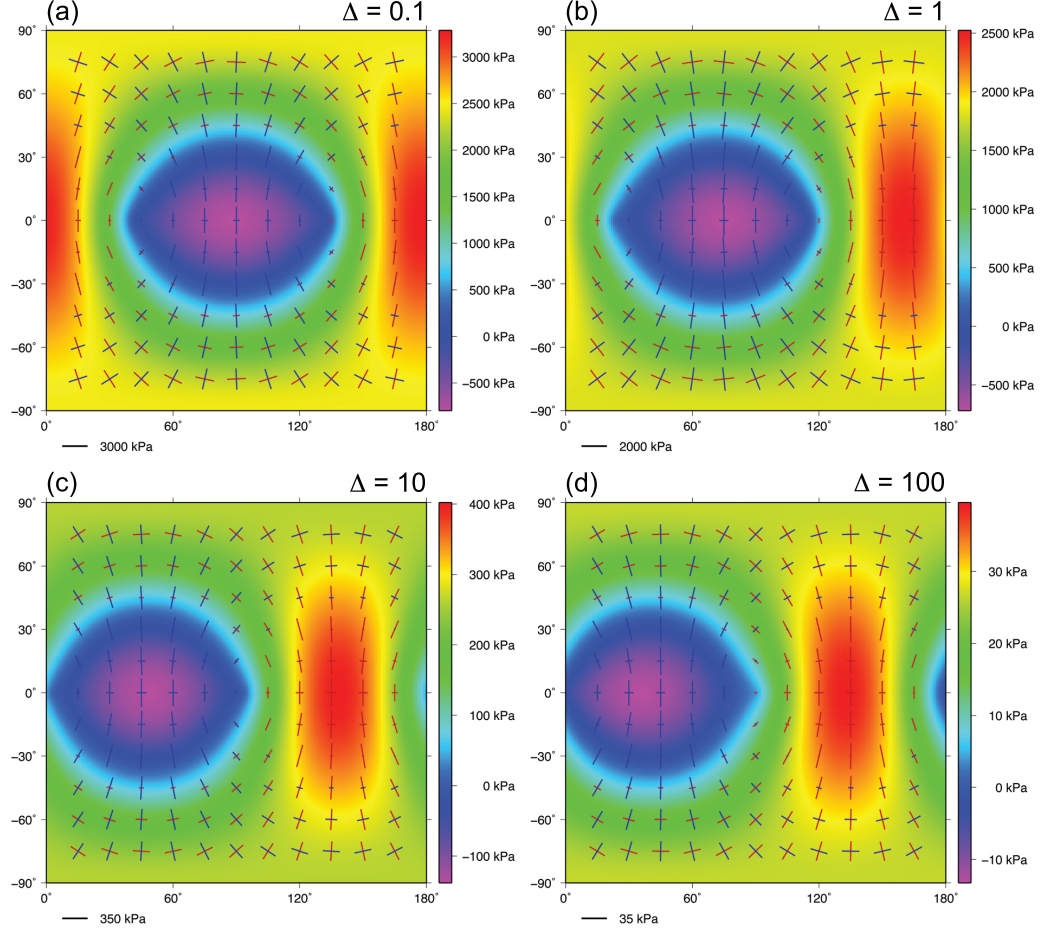


Figure 2.4: NSR stress results from the viscoelastic model for Europa at different values of Δ . Plots are similar to those in Fig. 2.3. The sub-Jovian point is at latitude = longitude = 0° , $\tau(\phi) = \tau(\phi + 180^\circ)$. The tic mark length and color scales indicating stress magnitudes vary among the four panels. Results are computed using the input parameters shown in Table 2.1, with the exception of the orbital eccentricity ϵ , which has been set to zero to exclude the contribution of the diurnal stresses. The length and color scales used in the panels varies, in order to allow each to show detail. (a) $\Delta = 0.1$, corresponding to nearly elastic stresses. The stress field is close to being symmetric about the planet-satellite vector (which passes through 0° and 180° longitude), though some small westward shift in the stresses is evident. (b) $\Delta = 1$ and the magnitudes of the stresses have been reduced slightly by relaxation, but the westward phase shift has increased significantly. (c) $\Delta = 10$ and the NSR stresses have largely relaxed away, though they are still significantly larger than the diurnal stresses pictured in Fig. 2.3. Here the phase shift is nearly complete, with the region of greatest tensile stresses close to its maximum separation from the planet-satellite vector. (d) $\Delta = 100$ ($\sim \epsilon^{-1}$ for Europa) and the overall NSR stress pattern is persistent, but the magnitudes are significantly smaller than those in Fig. 2.3. See Section 2.6.3 for further discussion.

the apparent longitude of formation of a lineament will also depend on Δ . If Δ is constant through time, this could introduce a constant translation of up to 45° to the lineaments whose shapes are determined by the NSR stress field, but their apparent longitudes of formation could still potentially be used as a proxy for their relative times of formation. However, if we allow that Δ may have changed through time [Nimmo *et al.*, 2006], it becomes difficult to infer even a relative time of formation, since different lineaments could have formed under different NSR stress regimes having different phase shifts.

Moreover, a variable Δ could allow the tidal stresses to transition between being dominated by diurnal and NSR tides. This could explain why on Europa we see both cycloidal lineaments (so far best explained by the diurnal tides) and the long arcuate global lineaments (plausibly related to the NSR tides, but see 3). If a change in Δ reflects a change in the rate of NSR, it could be that the global lineaments were formed during a period of rapid rotation in which the shell responded elastically to the NSR tide, and the cycloidal lineaments during a period of slow shell rotation, in which the NSR stresses were able to relax viscously, leaving the diurnal tide to dominate. Alternatively, a change in ice shell viscosity, e.g. through an episode of increased tidal heating or intense convection, could produce a similar change in Delta over time.

The model described here assumes the rate of NSR is constant. It assumes the time-dependence of the NSR forcing can be represented as a sinusoidal function with a single frequency. For an NSR rate that varies with time, the stresses could be computed by expanding the NSR forcing as a sum of sinusoidal functions, using the model described in this paper to find the stresses caused by each of those sinusoidal functions, and then summing those stresses together. A change in NSR would cause changes in the stress that depend not only on the initial and final NSR rates, but also on how quickly the NSR evolved. If that change in rate

happened quickly the induced stresses could be large during the transition even if the initial and final NSR rates were slow.

2.7 Comparison to previous methods

Results from the viscoelastic model described here can be used to assess the “flattening” model used in previous work to predict both diurnal and NSR stresses [*Helfenstein and Parmentier, 1985; Leith and McKinnon, 1996; Hoppa, 1998; Greenberg et al., 1998; Hurford et al., 2007*].

To estimate diurnal stresses, the flattening model computes the elastic response to the diurnal tidal potential terms, Eq. (2.4) and (2.5). To estimate NSR stresses, the model takes the difference between two stress fields. Each field is the elastic stress pattern caused by the NSR potential Eq. (2.3), with one field rotated about the \hat{z} axis relative to the other. In effect, one stress field is computed for $bt = 0$, and the other for $bt = \text{some specified angle}$.

In both the diurnal and NSR cases, the flattening model relates the elastic stress field to the elastic Love number h ; either explicitly [*Hurford et al., 2007*], or implicitly through a flattening parameter [*Leith and McKinnon, 1996*]. Although the Love number ℓ does not occur explicitly in the flattening formalism, a comparison with our elastic results, Eq. (2.11)-(2.13), shows that the flattening model implicitly assumes $\ell = h/4$, a result that is in good agreement with the elastic Love number results found here (see Fig. 2.1a and 2.1b in the $\Delta \rightarrow 0$ limit).

Figures 2.5a and 2.5b compare our diurnal stress results with those of the flattening model applied to a similar satellite. Both sets of results were computed for a time corresponding to 225° after perijove (i.e. $nt = 225^\circ$ in Eq. (2.27)-(2.29)). The two methods predict similar overall patterns. Amplitude differences are on the order of only 7%, and presumably reflect differences between the interior models used.

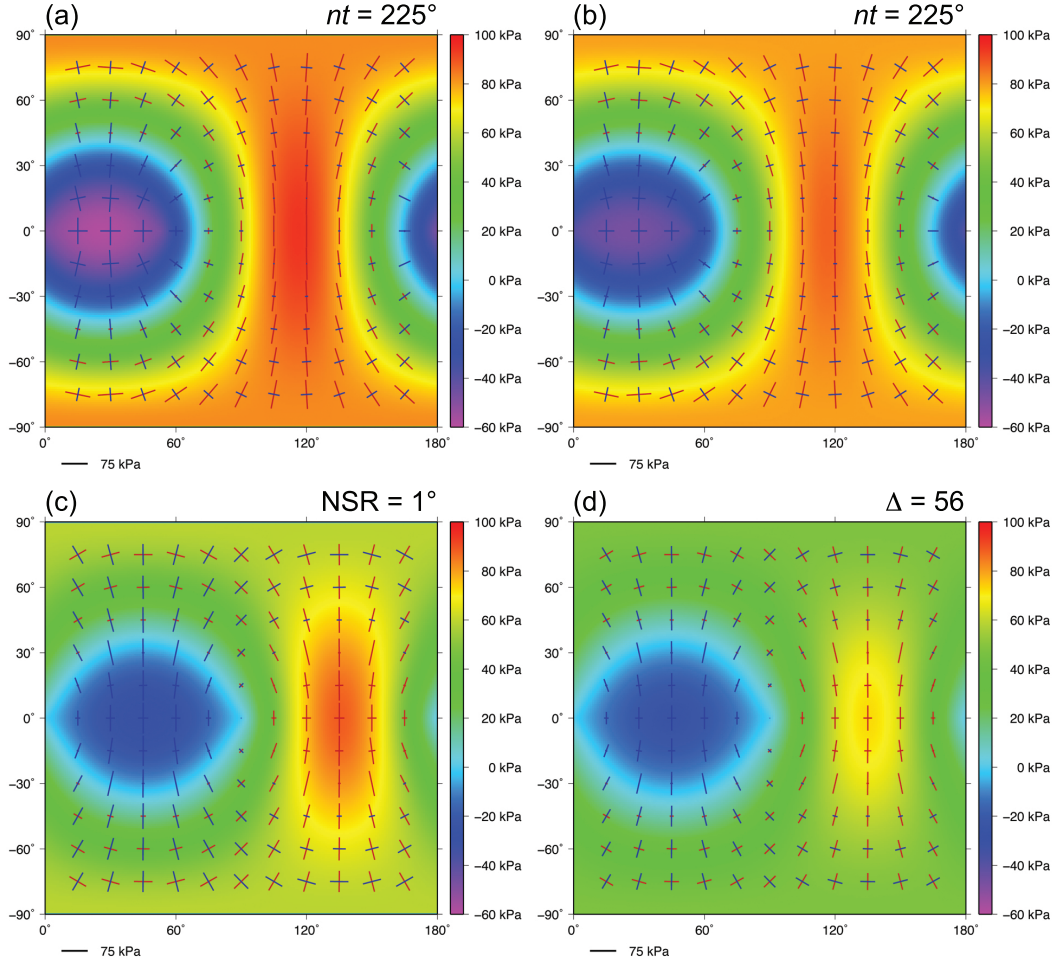


Figure 2.5: Stresses computed using the “flattening” method (left) compared to those from our viscoelastic model (right) for a satellite with similar physical properties. Table 2.4 lists the input parameters adopted for the flattening calculations (T. Hurford, personal communication, 2006). These parameters, excluding the real valued Love numbers, have also been adopted for the viscoelastic calculations. Because the viscoelastic model requires more information about the internal structure of the satellite in order to calculate the frequency-dependent Love numbers, those parameters in Table 2.1 not listed in Table 2.4 have been adopted in (b) and (d). (a) Flattening and (b) viscoelastic results for diurnal stresses at 225° after perijove (i.e. $nt = 225^\circ$ in Eq. (2.27)-(2.29)). (c) NSR stresses from the flattening method with 1° of accumulated NSR, compared to those calculated by the viscoelastic model (d) with $\Delta = 56$, at which point the two models each have a phase shift of 44.5° . See Section 2.7 for discussion.

The situation is more complicated for the NSR stresses. The flattening method's representation of those stresses as the difference between two elastic stress fields is somewhat ad hoc, and its relationship to the viscoelastic properties of the shell is not immediately obvious. Figure 2.2 can be used to empirically understand that relationship.

Figure 2.2a shows the largest tensile stress magnitude and the phase shift for the viscoelastic NSR model, as a function of Δ in the upper ice layer. The phase shift is defined here as the number of degrees of longitude separating the greatest tensile stress and the planet-satellite vector. For an elastic satellite the phase shift = 0° . Large values of Δ , corresponding to slow NSR rates and/or short viscous relaxation times, lead to phase shifts of 45° and small stress amplitudes.

Figure 2.2b shows the same quantities for the flattening model, as a function of the rotation angle between the two elastic stress patterns (the “accumulated degrees of NSR”, which in the flattening model is the parameter that describes how much stress is allowed to build up in the shell, similar to our Δ .) Small values of the rotation angle result in large phase shifts and small amplitudes. This can be understood by considering, for example, $\tau_{\theta\theta}$. The elastic result Eq. (2.11) has a longitudinal dependence of $\cos(2\phi + 2bt)$. The difference between this cosine and the same cosine when ϕ has been rotated by the angle δ , is $\cos(2\phi + 2bt) - \cos(2\phi + 2\delta + 2bt) \approx$ (when δ is small) $\delta \sin(2\phi + 2bt)$. The difference, thus, decreases in amplitude as $\delta \rightarrow 0$, and lags $\cos(2\phi + 2bt)$ by 45° in ϕ . The difference between these cosines has an increasing amplitude and a decreasing phase shift as δ increases, consistent with the results shown in Fig. 2.2b.

Figure 2.2c compares our viscoelastic results with the flattening results, by plotting the maximum stress as a function of the phase shift. The general shapes of the viscoelastic and flattening curves are similar. Though for a given phase shift the flattening model tends to overestimate the maximum stress amplitude

by a factor of about 1.5. Alternatively, for a given maximum stress the flattening model predicts a larger phase shift. The results thus show that the viscoelastic and flattening models predict different relationships between the magnitude of the NSR stresses and their location on the surface of the satellite. Either the phase shift or the magnitude of the NSR stresses can match, but not both simultaneously. Note that had we not allowed shear stresses to relax in the synchronously rotating core by using a low value of $\tilde{\mu}_{core}$ in the NSR Love number calculations, as discussed in Section 2.5 above, the real parts of the NSR Love numbers would have been similar to the diurnal values (see Fig. 2.1a and 2.1b, and Tables 2.2 and 2.3), resulting in the viscoelastic stresses being $\sim 35\%$ smaller, and increasing the difference from the flattening model even more.

To compare spatial stress patterns for the two different models of NSR stresses, we need to match up values of Δ in the viscoelastic model with corresponding values of accumulated NSR in the flattening model. The results shown in Fig. 2.2a and 2.2b indicate that small values of accumulated NSR correspond to large values of Δ (i.e. to long NSR periods and/or small viscosities). For every value of accumulated NSR in the flattening model we find the corresponding value of Δ in the viscoelastic model such that the two models give identical phase shifts for the maximum tensile stress. Because of the linear relationship between phase shift and the amount of accumulated NSR evident in Fig. 2.2b, we expect 1° of NSR to result in a phase lag of $44.5^\circ (= 45^\circ - (0.5 \times NSR))$. For the parameters used in these calculations, this corresponds to $\Delta = 56$. The comparison can be seen in Fig. 2.5c and 2.5d. The spatial patterns are in good agreement. The amplitudes of the flattening stresses are larger than the amplitudes of the viscoelastic stresses, but only by $\sim 20\%$ rather than the $\sim 50\%$ that might be expected from Fig. 2.2c. This is because Fig. 2.5c and 2.5d consider a phase shift close to 45° , which is where the flattening model has usually been applied

Table 2.4: Flattening model parameters (Figs. 2.2 and 2.5)

Parameter	Symbol	Value
Elastic Love number	h	1.2753
Elastic Love number	ℓ	0.31882 ($\equiv \frac{h}{4}$)
Mass of Europa	M_E	4.80×10^{22} kg
Mass of Jupiter	M_p	1.8986×10^{27} kg
Radius of Europa	R_s	1.561×10^6 m
Europa's orbital semi-major axis	a	6.709×10^8 m
Eccentricity of orbit	ϵ	0.01
Bulk modulus of ice ($= \lambda_{ice} + \frac{2}{3}\mu_{ice}$)	κ_{ice}	9.1764×10^9 Pa
Shear modulus of ice	μ_{ice}	3.5187×10^9 Pa

in the past. Figure 2.2c shows that as the phase shift gets close to 45° the amplitude of the viscoelastic stresses approaches and eventually even exceeds that of the flattening stresses, though both are small at large values of Δ . This is partly due to the buoyancy mode described at the end of Section 2.6.1, which begins to influence the surface stresses when Δ exceeds ~ 10 (see Fig. 2.1a, 2.1b, and 2.2a). The flattening stresses reach zero amplitude when the phase shift is 45° , but the viscoelastic stresses maintain an amplitude of at least a few kPa until the phase shift is close to 50° , and vanish only as $\Delta \rightarrow \infty$.

2.8 Summary and future work

We have developed and implemented a method of calculating the tidally induced surface stresses of a radially stratified satellite with a Maxwell viscoelastic shell of arbitrary thickness overlying an inviscid ocean and a silicate core, derived directly from the time-varying gravitational potential experienced by the satellite. All regions of the satellite are compressible and self-gravitating. The formalism could easily be extended to also include viscoelasticity within the silicate core, though we have chosen not to do so here. The results could also readily be extended to find the stress field at any depth within the shell, by using output from the numerical Love number code at sub-surface depths.

We have applied this model to radial and librational diurnal tides caused by the eccentricity of the satellite's orbit, and to tides that would be caused by faster than synchronous rotation of a floating shell. In both these cases we assumed the satellite's orbit has zero obliquity, so that the orbital motion is in the satellite's equatorial plane, and that the NSR motion occurs in that same plane.

Viscoelastic effects are incorporated through the use of frequency-dependent, complex-valued Lamé parameters and Love numbers. The inclusion of viscous relaxation has significant implications for the NSR stress environment at the satellite's surface, both reducing the magnitude of stresses due to long period forcings, and inducing a phase shift that translates the NSR stress field in the opposite direction of shell rotation. The importance of these effects depends on the ratio of the NSR period to the viscous relaxation time of the satellite's outer surface, a ratio described here by the parameter Δ . If $\Delta \lesssim 10$, NSR stresses are much larger than diurnal stresses, and are very similar to the elastic limit with a $\sim 0^\circ$ phase shift. If $\Delta \gtrsim 100$, the NSR stresses will have a phase shift of $\sim 45^\circ$, but their amplitude will be smaller than the diurnal stresses. The effects of viscoelasticity

on the diurnal stresses are insignificant for any plausible value of outer surface viscosity.

Because Δ affects the phase shift of the stress field, the apparent longitude of formation of a lineament will also depend on Δ . If we accept the possibility that Δ changes through time, this makes it more difficult to use a lineament's apparent longitude of formation as a proxy for its time of formation (as we attempt to do in Chapter 3), even relative to other lineaments, since they may have formed under NSR stress regimes with different phase shifts.

If we think the linear features observed on the surface of an icy satellite are tidally induced or influenced fractures, it must follow that the surface stresses sometimes exceed the strength of the icy lithosphere. This implies that localized stress release due to brittle failure plays a role in defining the surface stress environment [*Smith-Konter and Pappalardo, 2008*]. It would be beneficial to incorporate the formation of brittle fractures and the resulting changes in the stress field into the viscoelastic model (cf. [*King et al., 1994*]). However, that modeling is inherently numerical, requiring localized adjustment of the stresses as each crack forms and affects the formation of subsequent fractures in the region. Thus, the stresses of our model are those one would expect to find on the surface of a viscoelastic shell stronger than the greatest calculated stress. In this paper we have applied this model to the stresses experienced by a shell in steady state with a constant rotation rate, but there are many other possible scenarios for reorientation of a decoupled shell that are not well represented by a steady-state solution. A time-variable NSR rate can easily be accommodated using the formalism described here, while calculating the time evolution of stresses due to episodic polar wander will require enhancements to the model.

Chapter 3

A Critical Look at True Polar Wander and Non-Synchronous Rotation

3.1 Introduction

This chapter attempts to infer a history of lineament formation activity on Europa by assuming that non-synchronous rotation (NSR) of the ice shell has taken place, has been a dominant source of stress in Europa's lithosphere, and that the tectonic features we see are primarily the result of tensile fracture. Under those assumptions, one can use the amount of shell rotation required to position a given feature such that its shape is as consistent as possible with the NSR stresses, as a proxy for the amount of time elapsed since its formation. By performing this analysis for many features, we can estimate the history and time variability of the rate of lineament formation on Europa. Assuming that NSR has occurred we may also ask about what axis the rotation appears most likely to have taken place. If that axis differs from the current rotational axis, it might be taken as evidence of true polar wander (TPW) events.

If the shell is rotating, a feature's longitude of formation may be very different from its mapped longitude. In order to determine the most likely longitudes of formation, we can create a suite of synthetic lineaments formed at a range of different longitudes, each representing a hypothesis as to what we would expect our mapped feature to look like, had it formed there. We then take note of the longitudes which produce synthetic lineaments most similar to our mapped

feature.

Because the NSR stresses are periodic in longitude, repeating every 180° as seen in Fig. 2.4, we can explore the entire space of possible model lineaments by sampling across 180° of translation. We call this translation b and let $-90^\circ \leq b \leq 90^\circ$. Each of our model lineaments has a corresponding value of b , indicating how far away from its mapped prototype feature it was synthesized, and in what direction. If $b > 0$, the synthetic feature was formed to the east of the mapped feature, and if $b < 0$ it was formed to the west.

The shape of each synthetic feature is then compared to its prototype, using a dimensionless metric we call \bar{D} defined below, which is small when the mapped and modeled features are similar and large when they are different. The collection of measured \bar{D} values corresponding to the set of modeled features generated over the entire range of b values defines a curve, $\bar{D}(b)$, that describes how well our hypothesized features agree with our observations, as a function of longitudinal translation. The value of b which minimizes $\bar{D}(b)$ gives us our best estimate of how much shell rotation has occurred since the mapped feature was formed, but for most features there are a range of b values which indicate a decent match. Not all locations within the NSR stress field deserve equal weight when considering the agreement between the mapped and modeled features, as failure orientations are less well defined when stresses are close to isotropic, and less important when stresses are small. Accounting for this, we define another metric $f_{nsr}(b)$, which depends on both the modeled lineament's location within the stress field and $\bar{D}(b)$, indicating both the quality and the significance of a mapped feature's agreement with the NSR stresses at a given longitudinal displacement b from its current location. The length weighted sum of $f_{nsr}(b)$ over all the features in our map describes the apparent history of NSR lineament formation activity as a function of shell rotation, which we call $H(b)$.

We stress that it is an *apparent* history of activity, as there are several factors which potentially confound straightforward analysis of $H(b)$. The NSR stresses are periodic, and the surface could in theory preserve a record of more than one full shell rotation, resulting in activity from different times overprinting each other in our history. We do not know with absolute certainty whether the shell's rotation is prograde or retrograde. If $\Delta \gg 1$, meaning that the shell's response to the NSR forcing is viscous, there may be a significant phase lag in the stress field as described in Section 2.6.3. This would result in the translation of the $H(b)$ curve, as would any significant delay between fracture formation and visibility. Resurfacing processes operating on times which are short compared to the shell rotation period would obscure evidence of older activity. Perhaps most significantly, NSR might not be occurring at all: the existence of lineaments which fit the NSR stresses well is not necessarily indicative of NSR, as virtually any non-sinuous lineament will fit NSR well for some value of b .

Setting aside these caveats for the moment, we find a significant peak in $H(b)$ centered at $b = +30^\circ$, relative to the elastic NSR stress field. This is equivalent to $b = -15^\circ$ if $\Delta \gg 1$ and the shell's response is largely viscous, which was the implicit assumption of previous work (e.g. *McEwen* [1986]). They found that their lineament map best matched NSR when features were shifted 25° to the west (i.e. at $b = -25^\circ$). Given the much larger number of features included in the present work and the differences in our measurement techniques this seems a fairly good agreement.

The concentration of activity within a relatively small range of b values argues against the idea that many shell rotations are recorded by Europa's surface (cf. *Sarid et al.* [2004]; *Hurford et al.* [2007]), as there is little reason to expect tectonic activity to take place periodically and at the same frequency as shell rotation. The apparent peak in activity also very significantly distinguishes our

map from a variety of different random maps, which all have much more uniform histories. Indeed, it may be the only thing that makes our map unusual.

We also calculate $H(b)$ assuming other possible poles of rotation, as might be appropriate had the mapped features been the result of NSR stresses prior to a true polar wander (TPW) event, and find that the current pole produces an apparent activity history which is more non-uniform than 90% of the 1000 poles tested. However, we have not yet rigorously determined what fraction of the surface is statistically distinguishable from the current pole.

We also consider the question of the shell's direction of rotation and the possibility of a viscous phase lag. If we assume less than half a rotation is recorded by our map, then the b which we are measuring relative to the elastic NSR field is $b = -(\psi + x)$, where ψ is the phase lag, and x is the amount of shell rotation which has taken place since the peak in activity occurred (both east positive). If we assume that the shell's rotation is prograde (as the results to be presented in Chapter 4 suggest), then we have the constraints $x \geq 0^\circ$ and $-45^\circ \leq \psi \leq 0^\circ$, which given our peak at $b = +30^\circ$, indicates the maximum in activity took place anywhere between $0^\circ \leq x \leq 15^\circ$ of shell rotation ago, and that the NSR stresses in the shell are greatest 30° to 45° west of the maximum in the tidal potential. Looking at Fig. 2.2a we see that this would require $\Delta_{nsr} \geq 1$, and would limit the most tensile NSR stresses to being ≤ 1.75 MPa.

We also note that the peak in $H(b)$ and any apparent displacement from the current stress field need not be explained by a single finite episode of lineament formation activity, and could also be the result of steady state processes. For example, one might imagine newly formed fractures becoming gradually more visible during a period of early tectonic activity or eruption, and then slowly being obscured once quiescent, as resurfacing processes reduce their visibility. This would result in an apparently stationary peak, like a standing wave, with a

shape and location determined by the relative rates of shell rotation, lineament formation, activity, and resurfacing.

3.2 Methods

3.2.1 Mapping the Global Lineaments

Mapping was performed on a global mosaic of Europa's surface produced by the USGS having a maximum resolution of 500 meters/pixel composed of images from the Galileo and Voyager missions. Low latitude regions were mapped using a simple cylindrical projection and polar regions were mapped using polar stereographic projections. Linear features ranging in length from ~ 100 km to ~ 2000 km were selected for length and continuity. No effort was made to preferentially select those features that appeared consistent with NSR, or to exclude those that did not. If ambiguous branching junctions were found along the length of a lineament, it was broken into separate features at the junctions in order to avoid artificially associating branches that might be distinct tectonic structures. In all, 661 features, shown in Fig. 3.1, were mapped having a cumulative length of 231,800 km.

3.2.1.1 Assessing Global Map Biases

Because Europa has not yet been completely imaged at even moderate resolution, there are necessarily large gaps in the lineament map where confident identification of distinct structures is not possible. In order to assess the possibility that our map was systematically biased by this uneven coverage, we calculated the correlation between mapped lineament density and four observational variables: resolution, incidence angle, emission angle, and phase angle. In order to estimate the mapped lineament density at all points on the satellite N random points

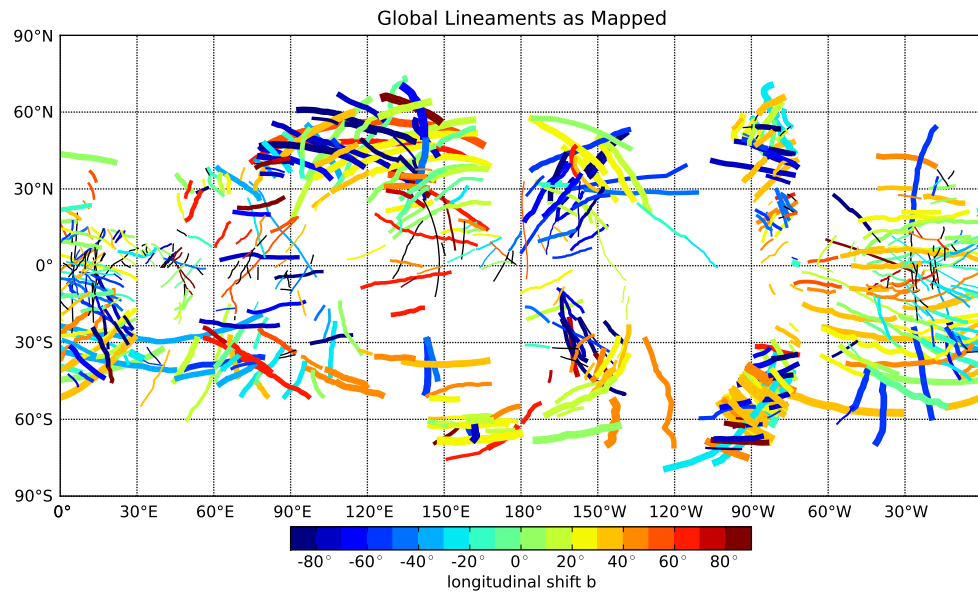


Figure 3.1: The entire set of mapped lineaments. Color corresponds to the value of b resulting in the lineament's best fit. Width corresponds to the value of \bar{D} at that value of b (wider implies a better fit). Thin black lineaments are those which were excluded entirely. This collection of features has $Q(\text{MAP}) = 0.512$.

evenly distributed over the sphere were chosen, and for each of them, the sum of the lengths of the mapped lineament segments whose midpoints were within a given distance d was calculated. A grid (seen in Fig. 3.2) was then interpolated between these N points, and the values of that grid were correlated with the four observational variables associated with the USGS mosaic. There was little to no correlation between the density of our map and these variables, suggesting that our map does not have large systematic biases due to imaging coverage (see Figs. 3.3 - 3.6).

We also compared the cumulative lengths of mapped lineaments within latitude and longitude bins to what would be expected from an evenly distributed map, and found that our map was close to being evenly distributed in latitude, with the largest deficiencies being at polar latitudes ($> 75^\circ$) representing a small portion of the satellite's surface, and fairly unevenly distributed in longitude, owing partly to the moderately high resolution north-south E15 regional imaging swath at $\sim 90^\circ\text{W}$ longitude. Uneven longitudinal coverage is not as serious a concern in the context of this analysis as poor latitude coverage would be, since a feature mapped at any given longitude may ultimately turn out to best fit the NSR stresses at any amount of shell rotation, whereas the deficiency at very high latitudes means our map is not sampling some small portion of the stress field at all.

3.2.1.2 Lineament Transformations

The reorientation of a lineament due to NSR is simply a longitudinal translation and can easily be modeled by adding or subtracting a constant to the longitudes of its vertices, but in order to explore the possible consequences of true polar wander we needed to transform the lineaments into the coordinate system of a pre-TPW Europa. To do so we take the modern day co-latitude (θ_{pmp}) and

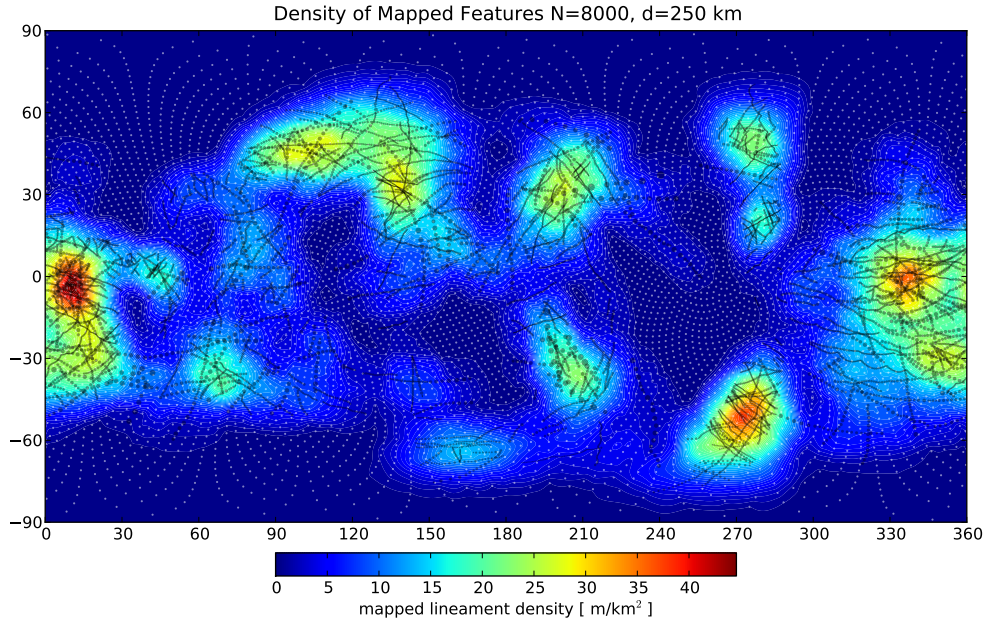


Figure 3.2: The surface density (mapped length per unit area) of lineaments on the surface of Europa. White points are the locations of the samples used to interpolate the grid. Black points show the location of the mapped vertices making up the lineaments (size proportional to length). The correlations between this mapped density and the imaging mosaic resolution, as well as other observational variables (see Figs. 3.3, 3.4, 3.5, and 3.6) are low. This suggests that while necessarily incomplete, the map does not have major systematic biases.

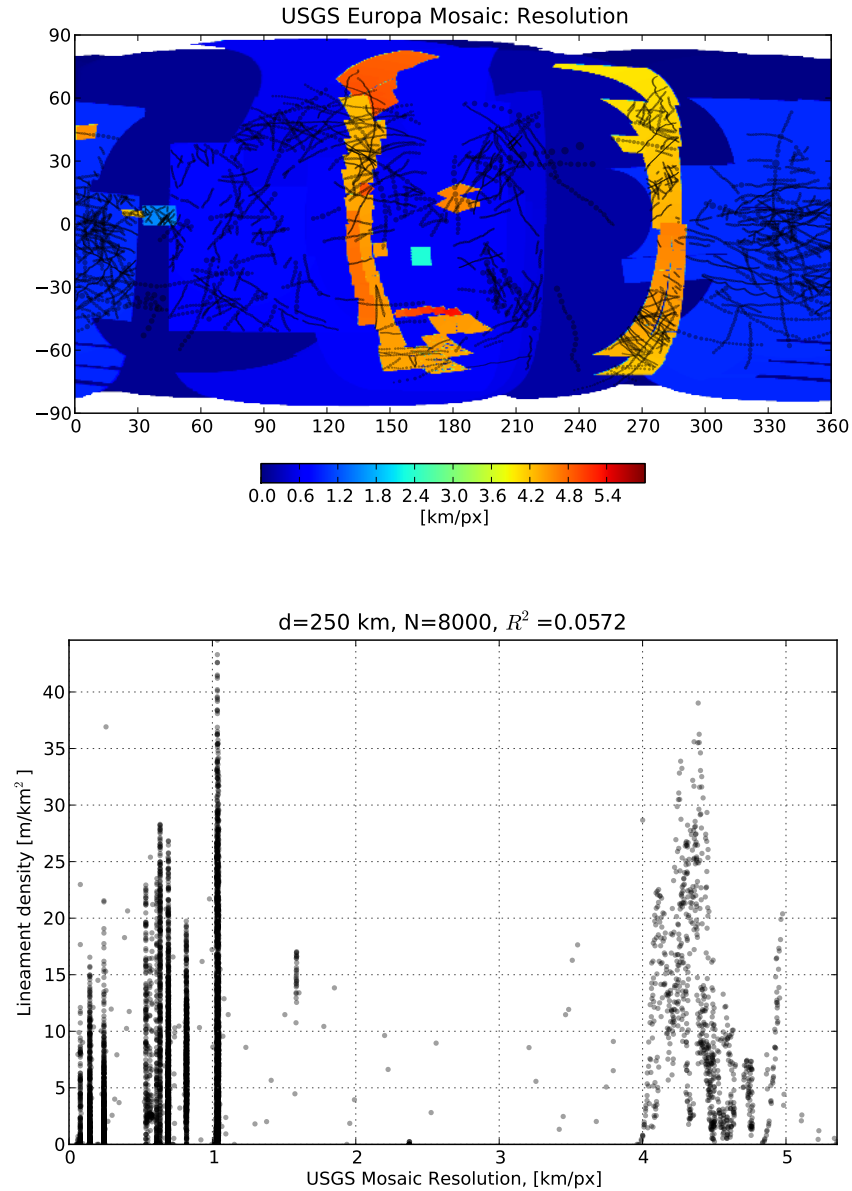


Figure 3.3: Correlation between mapped lineament density (see Fig. 3.2) and the resolution of the USGS mosaic on which the map was based. Black points in the upper plot are mapped vertices. Points in the scatter plot correspond to the 8000 uniformly distributed lineament density samples.

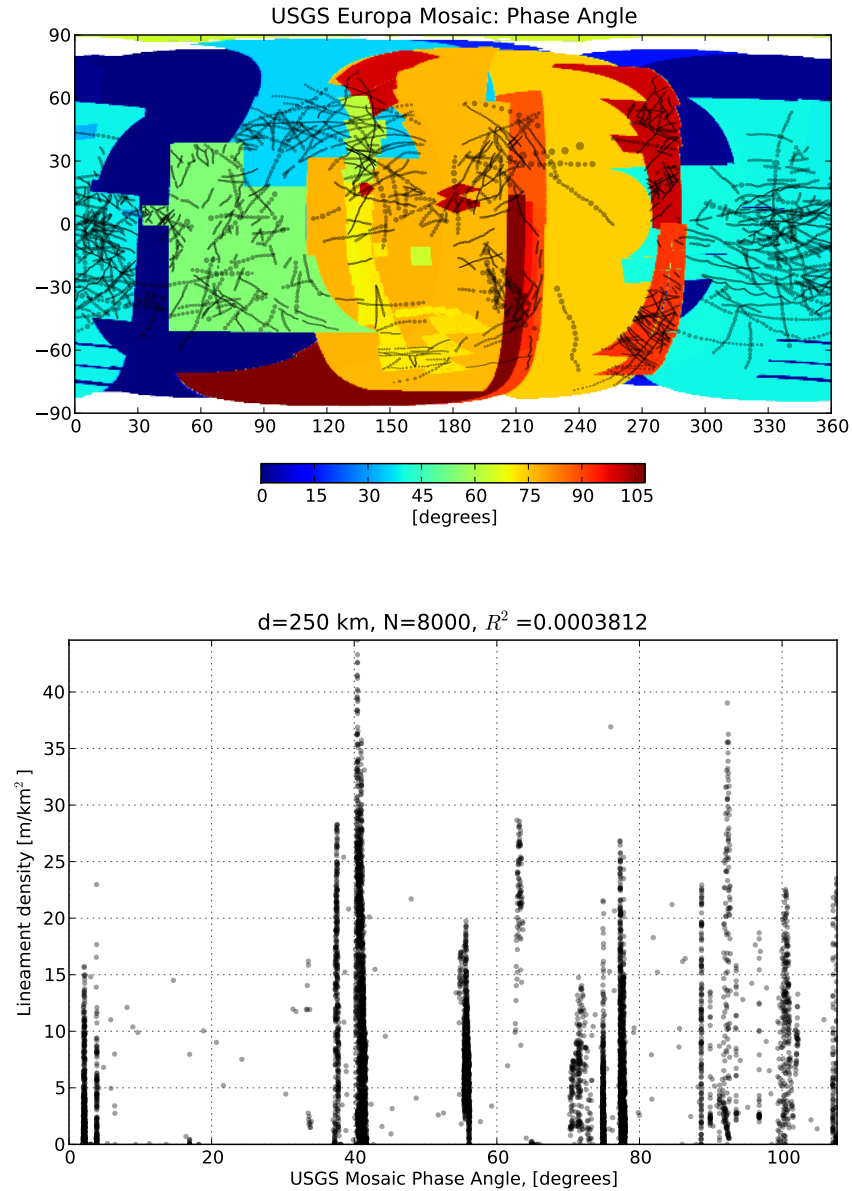


Figure 3.4: Correlation between mapped lineament density (see Fig. 3.2) and the phase angle at which the observations making up the USGS mosaic were obtained. Black points in the upper plot are mapped vertices. Points in the scatter plot correspond to the 8000 uniformly distributed lineament density samples.

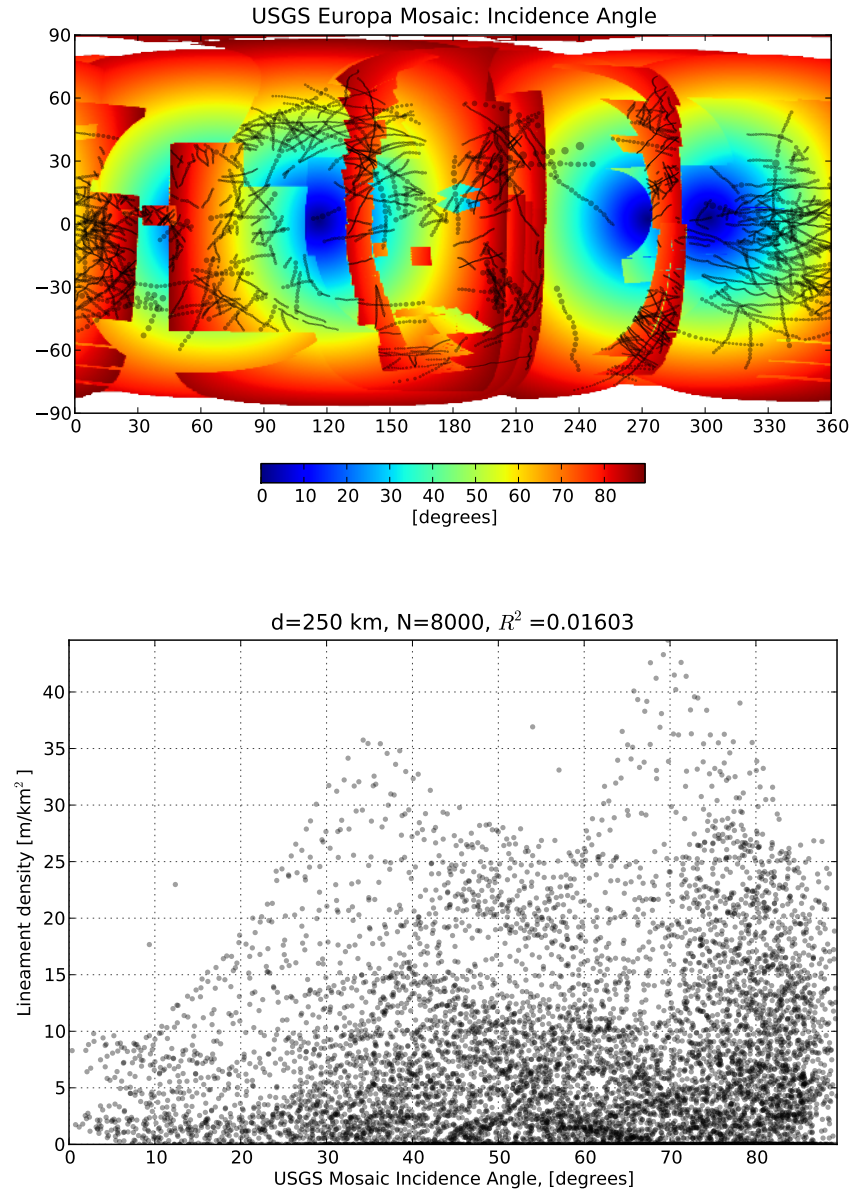


Figure 3.5: Correlation between mapped lineament density (see Fig. 3.2) and incidence angles of the observations which the USGS mosaic was based on. Black points in the upper plot are mapped vertices. Points in the scatter plot correspond to the 8000 uniformly distributed lineament density samples.

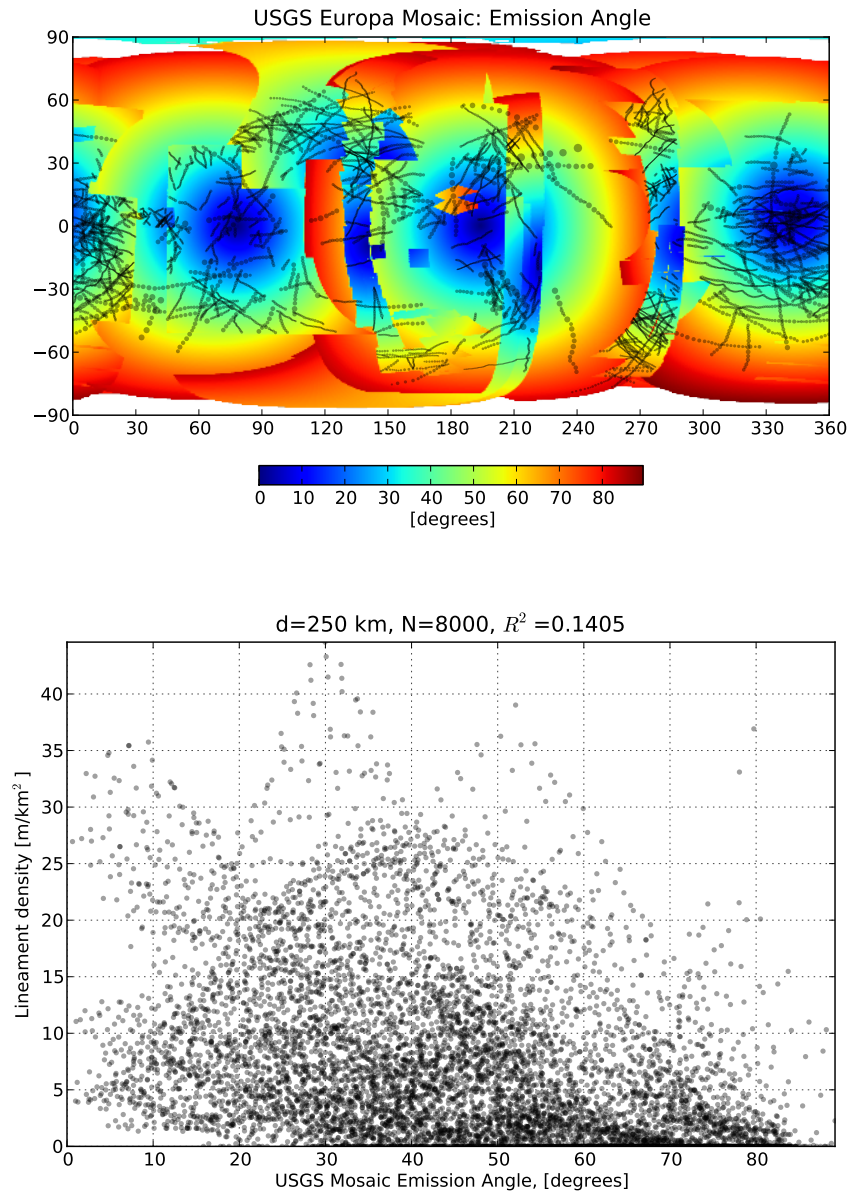


Figure 3.6: Correlation between mapped lineament density (see Fig. 3.2) and the emission angles of the observations which the USGS mosaic was based on. Black points in the upper plot are mapped vertices. Points in the scatter plot correspond to the 8000 uniformly distributed lineament density samples.

longitude (ϕ_{pnp}) of the hypothetical paleo-north-pole, and a point (r, θ, ϕ) on the surface of the sphere whose location we wish to transform and convert them to Cartesian coordinates, allowing $r = 1$ since we know all of our points are on the surface of the sphere, and we are taking the center of the sphere as the origin

$$\begin{pmatrix} x \\ y \\ z \end{pmatrix} = \begin{pmatrix} \sin \theta \cos \phi \\ \sin \theta \sin \phi \\ \cos \theta \end{pmatrix} \quad (3.1)$$

Then we obtain new (or rather, “old”) coordinates (x', y', z') by applying a rotation matrix defined by the location of the paleopole:

$$\begin{pmatrix} x' \\ y' \\ z' \end{pmatrix} = \begin{pmatrix} x \\ y \\ z \end{pmatrix} \begin{pmatrix} \cos \alpha & \sin \alpha \cos \beta & \sin \beta \sin \alpha \\ \sin \alpha & \cos \alpha \cos \beta & -\sin \beta \cos \alpha \\ 0 & \sin \beta & \cos \beta \end{pmatrix} \quad (3.2)$$

where $\alpha = \frac{\pi}{2} + \phi_{pnp}$ and $\beta = \theta_{pnp}$. Finally we transform back to spherical coordinates, and remove any longitudinal translation which has been introduced:

$$\begin{pmatrix} \theta' \\ \phi' \end{pmatrix} = \begin{pmatrix} \arctan \left(\frac{\sqrt{x'^2+y'^2}}{z'} \right) \\ \arctan \left(\frac{y'}{x'} \right) + \alpha \end{pmatrix} \quad (3.3)$$

The overall effect is that the transformed point is moved on the surface as if the paleopole had been moved directly north to the rotation pole. To transform an entire mapped feature, we simply transform each of the vertices defining it. The result of performing this transformation on the mapped lineaments, with the north paleopole now located at 80°W 10°N as suggested by [Schenk *et al.*, 2008] can be seen in Fig. 3.7. We have not within this work considered the stresses which would result from the reorientation event itself.

3.2.2 NSR Stress Calculation

Stresses due to non-synchronous rotation of the ice shell were calculated using the method described in Chapter 2 and Wahr *et al.* [2009]. Satellite pa-

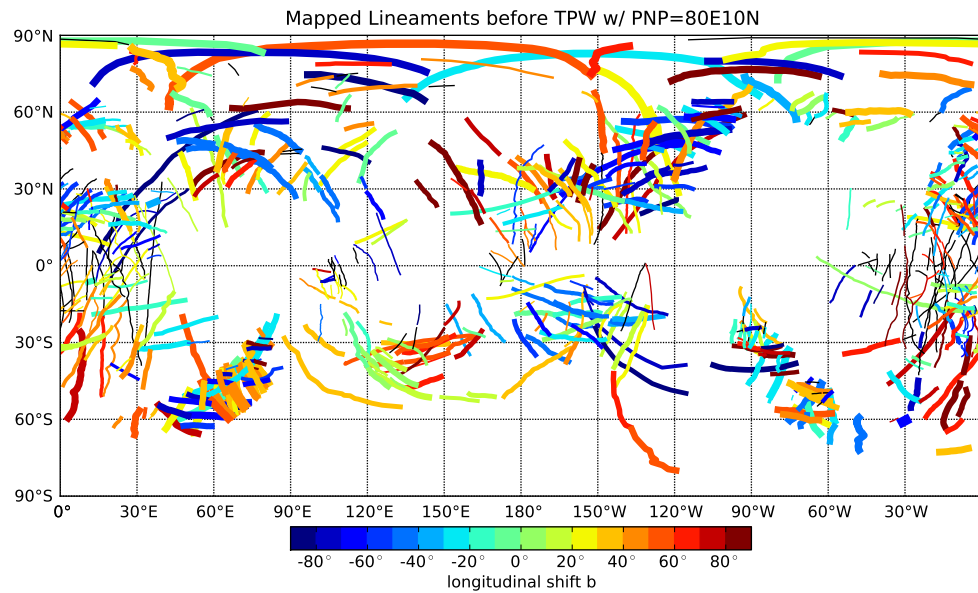


Figure 3.7: A map similar to that shown in Fig. 3.1, but showing the lineaments transformed to their locations prior to hypothetical TPW event in which the paleopole is currently located at 80°E , 10°N as suggested by Schenk *et al.* [2008]. The quality of this map's fit to the NSR stresses is only $Q(\text{TPW}) = 0.446$.

rameters were chosen in order to give the surface of the ice shell a nearly elastic response, with $\Delta \sim 10^{-2}$ (see Eq. 2.22). Within this regime the magnitude of the most tensile principal component of the stresses at the surface of the satellite can be as large as 3.2 MPa, and the phase lag between the forcing potential and the shell's viscoelastic response is negligible. See Table 2.1 for the complete list of the satellite parameters used. The resulting stress field is nearly identical to the one depicted in Fig. 2.4a.

Using parameters which result in an elastic response is acceptable because the main effect of viscous relaxation within the shell is to introduce a phase lag between the tidal potential and the resulting stresses, translating the stress field in longitude, and uniformly reducing the magnitude of the stresses as discussed in Chapter 2 and *Wahr et al.* [2009]. We can thus evaluate our results in the context of a viscous shell by looking at the relationship between Δ , stress magnitude and phase lag, as shown in Fig. 2.2a.

3.2.3 Comparing Lineaments to a Stress Field

With an expression describing the NSR stress field, and a collection of lineaments hypothesized to be the result of that stress field and tensile fracture of the ice shell, we turn to developing a method for comparing them. To make a direct comparison between a mapped feature and a calculated stress field, we must either infer stresses from a feature and compare those stresses with our calculated stresses, or use our calculated stresses to synthesize a lineament and compare that lineament with the one we mapped. We choose the latter because our direct observations are of lineaments, not stress fields, and because the synthesis of an ideal lineament given our stress field and failure mode is a forward modeling problem.

We are assuming that material failure takes place as tensile fracture, perpendicular to the more tensile of the principal components of the stress field on

the surface (the membrane stresses). We choose tensile fracture because it is the failure mode in which ice and most materials are weakest, because a NSR tide would induce tensile stresses over much of Europa’s surface, and because the expected orientation of failure is particularly well defined. Other failure modes are obviously possible, and can be explored using similar methods by defining different geometric relationships between the calculated stress components, and the resulting expected orientation (or orientations) of failure. This method of comparison can also be used more generally to compare a mapped feature to a stress field which is thought to vary on the timescale of the formation of the feature, for example cycloidal ridges resulting from the diurnal tidal stresses.

We further assume that the fractures that become lineaments form on a timescale much shorter than that of the ice shell’s rotation, and so we can treat the NSR stresses as being constant in time from the point of view of a propagating fracture. This means that aside from the parameters defining the gravitational potential and the material properties of the satellite, the only inputs that will affect the shape of a synthetic lineament are where within the stress field the fracture initiates and what direction it propagates. Given the NSR stress field and a mapped feature, generating a synthetic lineament representing what we would expect to see had that mapped feature been the product of those stresses is largely a question of choosing a place to initiate the fracture.

We select a point on the great circle defined by the plane passing through the satellite’s center and minimizing the sum of the squares of the length weighted distances from the midpoints of the mapped segments to that plane. We call this the lineament’s best fit great circle. We initiate fracturing at the point halfway between the points on this great circle which are closest to the endpoints of the mapped feature.

To find the plane defining the mapped feature’s best fit great circle we let

$r_i = l_i$, $\theta_i = \frac{\pi}{2} - \text{lat}_i$ and $\phi_i = \text{lon}_i$ where l_i is the length of the i^{th} segment making up the mapped feature and lat_i and lon_i are the latitude and longitude of the midpoint of the i^{th} segment. Let \vec{x}_i be the vector represented in spherical coordinates by (r_i, θ_i, ϕ_i) . The vector \vec{x}_i thus points from the center of the satellite toward the midpoint of the segment on the surface, and has a length proportional to the length of that segment.

The plane defining our best fit great circle can in turn be defined by a vector normal to it, \vec{u} , which we place at the center of the satellite pointing toward pole of the great circle (one of the two points on the sphere which are $\frac{\pi}{2}$ radians of arc away from it). Minimizing the length weighted sum of the squares of the distances from n mapped points to the plane defining the best fit great circle is equivalent to finding the vector \vec{u} which minimizes the sum:

$$\sum_{i=1}^n |\vec{u} \cdot \vec{x}_i|^2 \quad (3.4)$$

which is in turn equivalent to finding the eigenvector corresponding to the smallest eigenvalue of the matrix \mathbf{A} defined as:

$$\mathbf{A} \equiv \sum_{i=1}^n \vec{x}_i \vec{x}_i^T \quad (3.5)$$

Once we have found the fracture initiation point, we calculate the principal components of the NSR stresses and take as the direction of fracture propagation one of the two azimuths which are perpendicular to the most tensile principal component. We allow the crack to propagate on that heading for a small distance, add the new location to the list of vertices making up the synthetic lineament, and again calculate the NSR stresses, a new fracture propagation direction, and repeat the process until the synthetic feature is half as long as the mapped feature, or until the fracture has propagated into a region where the stresses are no longer tensile. The other half of the feature is constructed the same way, with the opposite initial propagation heading.

Determining to what degree the mapped and synthetic features resemble each other is not entirely straightforward because the lineaments are parametric curves, and it is not obvious which points on the two features ought to be compared to each other. In the context of computer vision this is known as the *correspondence problem*, and we borrow from that field a metric of shape similarity, the mean Hausdorff distance, and modify it slightly to suit our needs. The mean Hausdorff distance $MHD(A, B)$ from a set of points A to another set B, is defined as

$$MHD(A, B) \equiv \frac{1}{N_A} \sum_{a \in A} \min_{b \in B} \|a - b\| \quad (3.6)$$

where N_A is the number of points in A, and $\|a - b\|$ represents an underlying norm defined in the space of the two sets of points. In our case this norm is the distance along the spherical geodesic from a to b . This definition assumes that all points in A are of equal importance, and that the metric has a scale which is proportional to the scale of the two shapes being compared (i.e. $MHD(A, B)$ has units of distance). We define a new metric $\bar{D}(A, B)$:

$$\bar{D}(A, B) \equiv \frac{1}{L_A^2} \sum_{a \in A} l_a \min_{b \in B} \|a - b\| \quad (3.7)$$

where the sets A and B are the midpoints of the lineament segments for the mapped and synthetic features respectively, L_A is the overall length of the mapped lineament A, and l_a is the length of the individual lineament segment whose midpoint is a . Note that in general $\bar{D}(A, B) \neq \bar{D}(B, A)$. For example, consider the case in which A is a proper subset of B: $\bar{D}(A, B) = 0$, but $\bar{D}(B, A) > 0$, because of the nonzero distances from those points in B and not in A, to the nearest point which is within A. We choose to use $\bar{D}(\text{observed}, \text{model})$ instead of $\bar{D}(\text{model}, \text{observed})$ to avoid such cases, which would otherwise lead to overly optimistic fits when a synthetic feature is terminated early due to propagation of the fracture into a compressive region.

We weight by the lengths of the of the mapped lineament segment l_a because although each lineament is composed of a series of discrete points, it is meant to approximate a continuous curve. Long straight portions of a feature can be mapped accurately with only a few vertices, while sinuous portions require more points for the same length. We use the segment midpoints instead of the vertices themselves to avoid the special cases of endpoints and because the length which ought to be associated with each midpoint for weighting purposes is obvious.

In order to be able to use \bar{D} to compare how well two features of different scales match their respective synthetic doppelgangers, we have normalized it by the length of the mapped feature L_A , making it into a unitless quantity. The metric \bar{D} is thus an approximation of the mean distance from the points on the mapped feature A to the nearest point on the synthetic feature B, expressed as a fraction of the overall length of A. We can see that if A and B are two straight lines of equal length which intersect at their midpoints, we must have $0 \leq \bar{D}(A, B) \leq 0.25$. This is strictly correct in a Euclidean geometry because $MHD(A, B)$ scales linearly with feature length so long as the features remain similar (in the geometric sense). In spherical geometry, $MHD(A, B)$ will scale less than linearly with increases in feature length, but so long as the scale of the features is small relative to the radius of the sphere it will be approximately true, and even when the feature lengths are comparable to the radius of the satellite this deviation is not big enough to be significant, in light of the much larger effects of sinuosity, location, and orientation we will discuss below.

3.2.4 Inferring a Time Series

The above method allows one to compare a lineament to a stress field in its current location, but what we are interested in is how the mapped features would have compared to the NSR stress field at some time in the past, when the ice shell's

rotation had not yet brought the feature to its current location. That is, we want to know how \bar{D} varies as a function of a longitudinal translation b applied to the lineament in question. We can explore this by moving the fracture initiation point in longitude by b , generating the synthetic feature, and then translating that feature back by $-b$ such that its midpoint is centered on the mapped feature A before calculating \bar{D} . We use $\bar{D}(A, b)$ to denote the fit as a function of the mapped feature and the amount of translation, with the implicit assumption that the synthetic features are generated as described above.

Synthetic features created at some values of b will be more similar in shape to their prototypes than others, indicating the relative plausibility of our formation hypothesis at those different locations within the stress field. If we believe that the direction of shell rotation has been consistent, and that less than 180° degrees of rotation is recorded by our map, then we should be able to order the features according to their time of formation by ordering them according to the value of b at which $\bar{D}(b)$ is minimized.

Whether a feature X matches the stress field is not a discrete question, as $\bar{D}(X, b)$ varies continuously. In analyzing the mapped dataset as a whole we would therefore like to allow a given feature to contribute to the cumulative length of plausible lineaments at any value of b for which $\bar{D}(X, b)$ is less than some threshold value \bar{D}_{max} . This contribution should be in proportion both to its own length, and to how well it fits the NSR stresses at that location. We define a quantity $0 \leq f_{nsr}(X, b) \leq 1$ which can be used as a weighting function or probability, indicating how likely it is that a feature X resulted from NSR stresses at a particular amount of longitudinal translation:

$$f_{nsr}(X, b) \equiv \max \left(0, \left(1 - \frac{\bar{D}(X, b)}{\bar{D}_{max}} \right)^2 \right) \quad (3.8)$$

where \bar{D}_{max} is the greatest value of $\bar{D}(X, b)$ which we are willing to admit might

indicate agreement between the mapped and synthetic features. The choice of \overline{D}_{max} is somewhat arbitrary, but the overall results are not very sensitive to its value (see Figs. 3.8 and 3.17). Unless otherwise noted, we have used $\overline{D}_{max} = 0.125$ in all our analyses. In Euclidean geometry this would correspond (for example) to two line segments intersecting at their midpoints with an angle of 30° between them.

Using $f_{nsr}(X, b)$ we can construct a history of apparent lineament formation activity. For each value $-90^\circ \leq b \leq 90^\circ$, we calculate the length-weighted sum of $f_{nsr}(m, b)$ over all features m in the mapped dataset M :

$$h(M, b) \equiv \frac{1}{L_M} \sum_{m \in M} l_m f_{nsr}(m, b) \quad (3.9)$$

where L_M is the sum of the lengths of all the mapped features, and l_m is the length of the feature m within that set. The apparent activity history $h(M, b)$ is then the fraction of the overall dataset which we consider consistent with the NSR stresses at a given translation b .

3.2.5 Stress Isotropy and Noise

Not all portions of the stress field are equally important. This is true for two reasons. First, the magnitude of the stresses varies geographically, and while we are not explicitly introducing the strength of the ice into our model, all else being equal, one would expect failure to be more likely in an area with large stresses than in one with small stresses. Second, the closer the surface stress is to being isotropic, the less well defined the expected failure direction is, making disagreements between expected and observed failure orientations more meaningful in highly anisotropic regions.

The need to account for each of these effects stems from the fact that there must be some noise in the real stress field on the surface of the satellite resulting

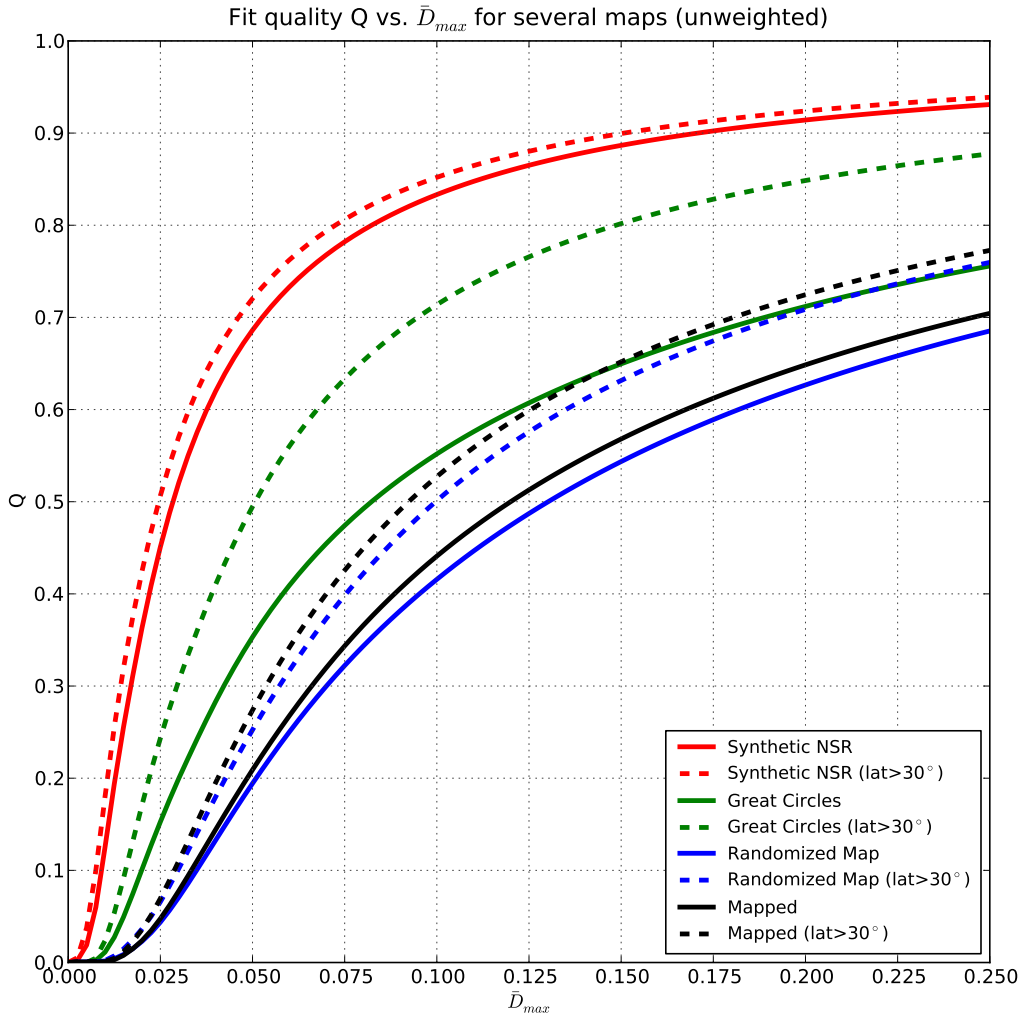


Figure 3.8: The fit quality Q (see Eq. 3.13) as a function of \bar{D}_{max} , for several maps: synthetic NSR features (red), random great circle segments (green), the mapped features randomized and re-sampled (blue) and the mapped features, as mapped (black). The dashed lines show how the map performs when the equatorial regions are excluded (i.e. with any feature having vertices within 30° of the equator removed). As expected, the perfect synthetic features do well in both the global and high-latitude cases. The random great circle segments, having zero sinuosity, do very well when the equatorial regions are excluded, as at high latitude, any orientation is acceptable for some value of b , and sinuosity becomes the main factor in lineament fit to the NSR stresses. The black and blue curves, corresponding to our mapped features, in their mapped locations and randomized (respectively) are essentially indistinguishable.

from prior tectonic activity and inhomogeneities in the lithosphere. When the background noise is capable of significantly perturbing the orientation of failure, our expectations based on the calculated tidal stress field are no longer meaningful. If the background stresses are comparable in magnitude to the tidal stresses, they will clearly be able to perturb the expected orientation of failure. Perhaps less obviously, in the case of large but nearly isotropic stresses even a small background stress can significantly perturb the orientation of the principal components (though not their magnitudes), because the eigenvectors of the stress tensor become very sensitive to any change in the stress field when the eigenvalues are nearly equal.

Unfortunately, because we don't know the magnitude of the background stresses, all we can do is estimate the importance of a fit or misfit at a particular location within a stress field relative to other locations within the same stress field. Therefore we define a location dependent stress weighting function w :

$$w(\theta, \phi) \equiv \frac{\sigma_t(\theta, \phi) - \sigma_c(\theta, \phi)}{\langle \sigma_t - \sigma_c \rangle} \quad (3.10)$$

where σ_t and σ_c are the magnitudes of the more tensile more and compressive principal components of the stresses, which vary as a function of co-latitude and longitude θ and ϕ . This weighting function w indicates the robustness of the predicted failure orientation at a given location. It becomes small as the stresses approach isotropy (as their difference becomes small relative to their magnitudes), and also when their difference is small relative to the global mean stress difference, denoted above as $\langle \sigma_t - \sigma_c \rangle$.

For the lineament A as a whole, we can define an analogous quantity W , which like \overline{D} above will vary with b as we explore the space of possible shell backrotations:

$$W(A, b) = \frac{1}{L_A} \sum_{a \in A} l_a w_a(\theta, \phi - b) \quad (3.11)$$

where L_A is the overall length of the lineament A, l_a is the length of the line segment a within that lineament, and w_a is the value of the weighting function w above, calculated at the midpoint of the segment a .

We then combine $W(A, b)$ with $h(A, b)$ defined above to get $H(A, b)$, which is the quantity we will be looking at in the results as a measure of apparent history of lineament formation activity:

$$H(M, b) \equiv \frac{1}{L_M} \sum_{m \in M} l_m W(m, b) f_{nsr}(m, b) \quad (3.12)$$

with m being a mapped lineament of length l_m , contained in the set of all mapped lineaments M , which has a cumulative length L_M . Examples of several mapped lineaments and their associated $\bar{D}(b)$, $f_{nsr}(b)$, and $W(b)$ curves can be seen in Fig. 3.9.

3.3 Results

With the methods described above we can now ask what characteristics identify a lineament as being compatible with the NSR stresses; the answer is surprisingly vague. The only clear requirements are that the feature be relatively non-sinuous, and that if located within 30° of the equator, it must be oriented east-west. This description is so broad as to make it impossible to confidently identify any particular feature as having resulted from the NSR stresses. However, we can identify some features as being inconsistent with NSR, and it may be possible to identify characteristics of ensembles of features which are diagnostic of NSR. One possible metric is the uniformity of the inferred activity history.

3.3.1 Quality of fit is surprisingly uninformative.

We can construct a gross measure of the quality of the fit for a set of lineaments as a whole to the NSR stress field using the definitions from the previous

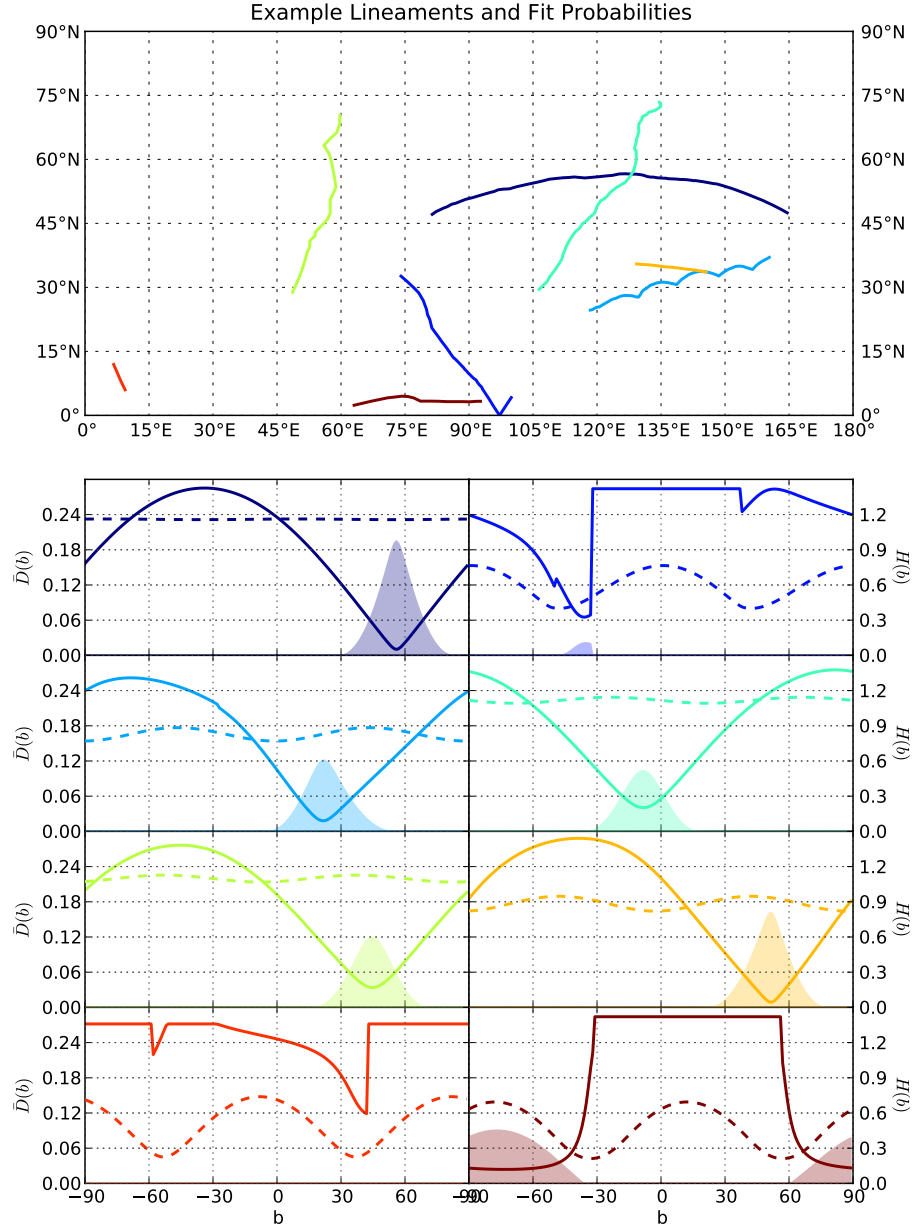


Figure 3.9: Eight lineaments are pictured in the top panel, which is a map representing one quarter of the surface, with longitude and latitude folded to account for the symmetry in the NSR stress field. The lower eight panels show the fit curves corresponding to the lineaments, and are color coded to match them. The x-axis in all of the fit curves is b , ranging from -90° to 90° . The solid lines are the metric of shape similarity, $\bar{D}(b)$ (left y-axes). The dashed lines are tied to the right y-axes, and show the stress weighting function $W(b)$. The filled curves are also tied to the right y-axes, and show $H(b)$ for a “map” consisting of that single lineament. As elsewhere, we have chosen $\bar{D}_{max} = 0.125$

section:

$$Q(M) \equiv \frac{1}{L_M} \sum_{m \in M} l_m \max(f_{nsr}(m, b)) \quad (3.13)$$

and use it look at the performance of various datasets, some of which we know have nothing to do with the NSR stresses. This Q is, loosely, the proportion of the overall mapped length which is retained when each of the lineaments is shifted in longitude by that b which results in its best fit.

Figure 3.10 shows a collection of great circle segments with randomized locations and orientations and the same length distribution as the mapped features, having $Q(\text{GC}) = 0.607$. Fig. 3.12 shows the mapped lineaments with random translations and rotations applied to each one independently, having $Q(\text{Random}) = 0.487$, and Fig. 3.11 shows a perfect synthetic dataset, generated from our calculated NSR stresses and our hypothesized failure mode, with $Q(\text{NSR}) = 0.865$. The great circle segments represent a null hypothesis: that the lineaments are completely random and featureless. The synthetic features have the shapes and orientations that we would expect to see if all of the features agreed with our hypothesis. The randomized map allows us to control for the effect of the shapes of the mapped lineaments, independent of their locations and orientations. The real map from Europa pictured in Fig. 3.1 has $Q(\text{Map}) = 0.512$, virtually indistinguishable from the randomized map, and significantly worse than the great circle segments. If we transform the mapped features to their locations prior to a hypothesized TPW event with a paleo-north pole at 80°E 10°N , we get the map shown in Fig. 3.7, which does marginally worse than the random map, with $Q(\text{TPW}) = 0.446$.

Several things need to be explained in the above results. Why does our synthetic map have $Q < 1$? Why do the great circle segments do significantly better than either our real map or the randomized map? How is it that the

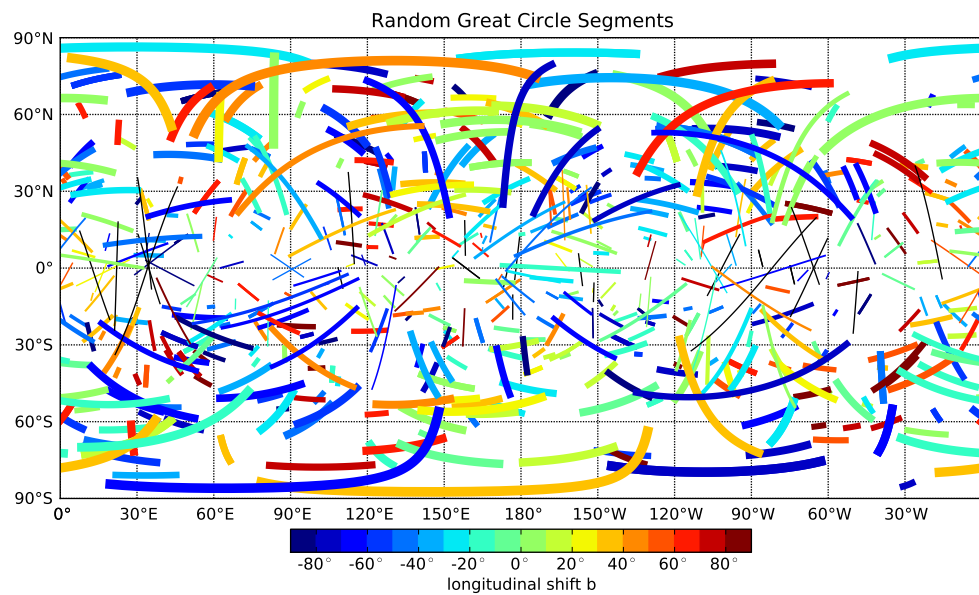


Figure 3.10: A map similar to that shown in Fig. 3.1, but showing a synthetic dataset composed of great circle segments, having random locations and orientations, with feature lengths drawn from the length distribution of the mapped features. This “dataset” also fits the NSR stress field about as well as the mapped features with $Q(GC) = 0.607$, but has a flat distribution of apparent activity through time.

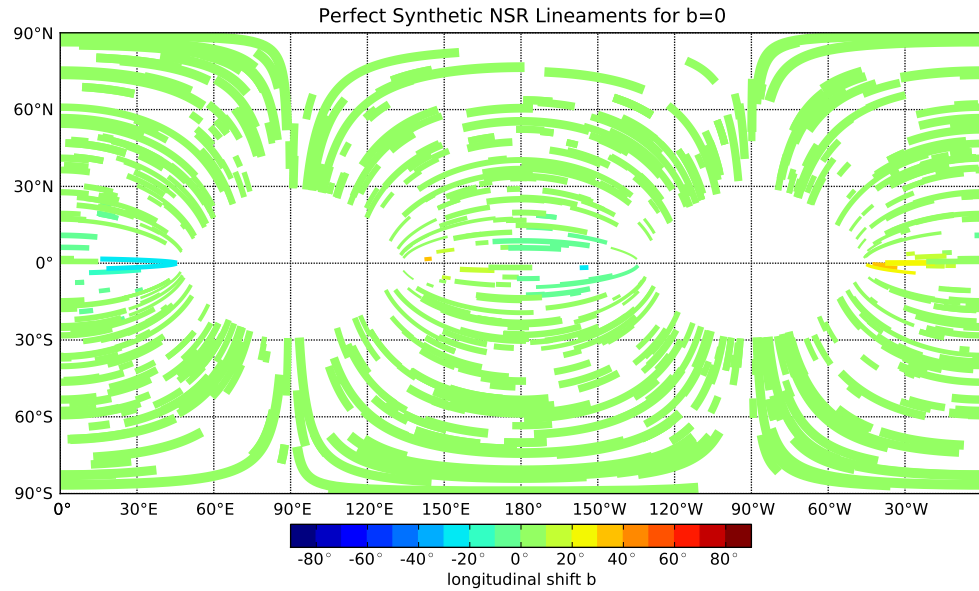


Figure 3.11: A map similar to that shown in Fig. 3.1, but showing a synthetic dataset composed of idealized tensile fractures due to NSR stresses, with random locations. The synthetic feature lengths are drawn from the distribution of mapped feature lengths. All lineaments were formed at $b = 0^\circ$ in the elastic NSR field, and so are symmetric about the Jupiter-Europa axis. Unsurprisingly, this map fits the NSR stresses very well, with $Q(\text{NSR}) = 0.865$.

mapped features appear to fit the NSR stresses no better than the randomized map? It can be seen from Fig. 3.8 that these results are not an artifact of our choice of \overline{D}_{max} .

The synthetic map's performance is better than it might seem, and the remaining discrepancy can be explained. When the shapes of the prototype and the hypothetical lineaments are very similar, \overline{D} is determined primarily by the distance between our chosen initiation point and the prototype feature, and the synthetic NSR features aren't quite great circle segments, so this distance is nonzero. Additionally, the fact that the quantity defining $f_{nsr}(b)$ is a quadratic function of \overline{D} magnifies the apparent misfit: $Q = 0.865$ actually corresponds to an average minimum value of \overline{D} which is less than 0.01. If instead of using the best fit great circle segment midpoint, we choose to initiate the model fracture at the point within the feature which is nearest to that point, we find $Q(\text{NSR}) > 0.99$. That method of choosing the initiation point does not work well for real features though, as their nontrivial sinuosity often means that the nearest point within the feature is a significant distance from the best fit great circle segment midpoint, and does not result in a very good fit. Another consideration is the spacing between the vertices defining the synthetic lineament. Because the NSR features are so close to being great circle segments, it is possible to use relatively large distances between calculations and still get an accurate shape. If the separation between synthetic vertices is greater than the separation between the prototype and synthetic lineaments, then it is that along-lineament separation that will dominate \overline{D} . We avoid this problem by adding a large number of vertices to the model lineaments between the points at which stress calculations are actually performed during their synthesis.

The fact that our actual map fares no better in fitting the NSR stresses than our randomized map should give us pause. If this is true, then what evidence do

we have that NSR is actually taking place?

3.3.2 Sinuosity, location and orientation determine lineament fits.

The tidal potential resulting from NSR can be described entirely using degree two spherical harmonics. This necessarily means that the NSR stresses do not have a detailed structure. When combined with our exhaustive search over the space of possible b values this means that almost any lineament can be made to fit well somewhere within the stress field, with a couple of minor caveats.

The set of synthetic NSR lineaments has a significantly higher Q than all the other datasets primarily because it lacks north-south oriented features in the equatorial regions, as well as equator crossing lineaments. Such features never fit the NSR stresses well enough to have $f_{nsr}(b) > 0$ for any value of b (in Figs. 3.1, 3.12, 3.10, and 3.7 they are drawn in black) and thus do not contribute any of their length to the apparent history of activity. Conversely, at latitudes greater than 30° orientation never plays a decisive role in whether a feature fits the NSR stresses, as can be seen in Figs. 3.1, 3.12, and 3.10, where no feature entirely outside of the low latitude regions is ever excluded. This is because at mid to high latitudes, over any contiguous 180° of longitude, the more tensile principal component of the NSR stresses takes on all possible orientations, and because the synthetic NSR features never deviate much from being great circle segments. The fact that none of our mapped features is ever excluded at latitudes $> 30^\circ$ also suggests that, at least within the range of sinuosities we see in the mapped features, it is not playing a major role in deciding which features are retained and which are excluded.

The sinuosity (S) of a lineament is the ratio of the sum of the lengths of all of its component segments to the length of the spherical geodesic connecting its endpoints. By definition, the great circle segments all have sinuosities of 1.0 (the

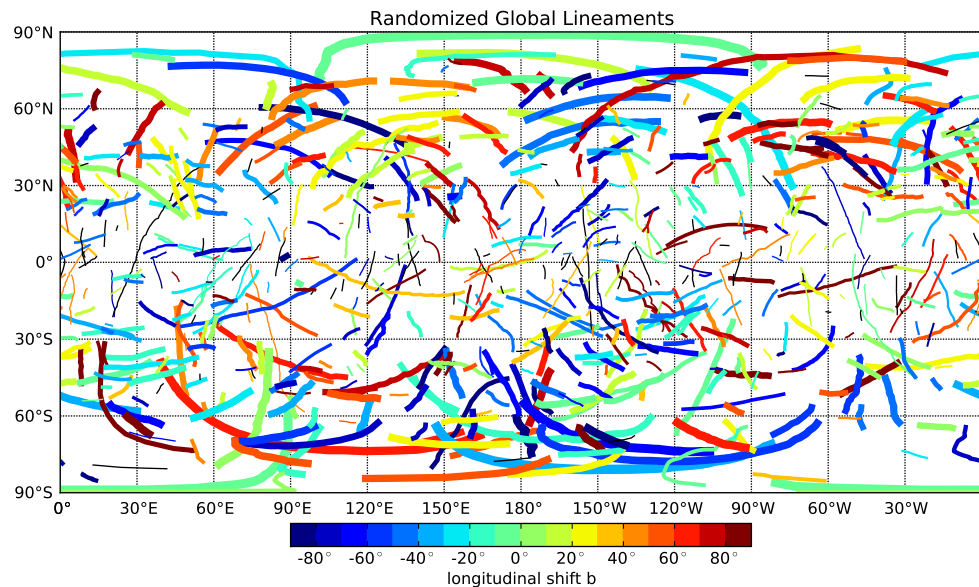


Figure 3.12: A map similar to that shown in Fig. 3.1, but showing a synthetic dataset composed of the mapped lineaments scattered randomly over the surface locations and orientations. Such datasets fit the NSR stress field just as well as the mapped features (with $Q(\text{Random}) \approx 0.487$), but have a more uniform activity history.

minimum possible value). Out of a set of 10,000 synthetic NSR features generated over the entire range of possible locations, more than 90% of them had sinuosities less than 1.01, and none of them had sinuosities greater than 1.025 (values so low as to make one wonder whether they deviate from unity only because of the finite spatial resolution of the calculation). In contrast $\sim 40\%$ of the mapped features had $S < 1.01$ and a few had $S > 1.2$. One consequence of this is that outside of the equatorial regions sinuosity becomes a fairly good predictor of $\min(\overline{D}(b))$ (with $R^2 = 0.324$) while within the equatorial regions the two quantities are uncorrelated.

This means there are only a couple of ways for a feature to be rejected as not plausibly resulting from NSR stresses for some value of b : to be very sinuous anywhere, or to have an overly north-south orientation within the equatorial regions. Moreover, features which do fit well in the equatorial regions tend to do so for a wide range of b values, since the orientations of the stresses don't change much with longitude there, limiting the information contained in such fits (see Fig. 3.9 for illustration). This fit degeneracy combined with the generally low values of $W(b)$ associated with any feature within the equatorial regions means that they play a limited role in the localization of features in the $H(b)$ curve for the map.

These results suggest that while our fit metrics can potentially be used to discern for which values of b a feature might plausibly have been the result of NSR stresses, they can do relatively little to inform us as to whether a particular feature or collection of features is a “good” fit to the NSR stresses, at least for any dataset with the spectrum of sinuosities which we see in our map. The requirements for a feature to fit NSR well are inherently lenient, and in exploring the range $-90^\circ < b < 90^\circ$ we are exerting a powerful selection effect: for some value of b , most lineaments will appear to fit well. If we then discard and ignore

anything that didn't fit well, it should be unsurprising that our survivors match the NSR stresses, as that's exactly what we selected for them to do.

One might legitimately question the exclusion of the north-south oriented features in the equatorial regions from our results. Those lineaments (and others) might well be the products of shear failure, with a different failure geometry than what we have assumed for tensile fracture. However, even when considering only a single well-defined failure mechanism, the requirements imposed by the NSR stresses are very lax. Introducing additional acceptable failure orientations would only further reduce the uniqueness of the fits, and in that event, we would likely have to conclude that no useful information can be gleaned from attempting to fit lineaments to the NSR stresses.

3.3.3 We need new metrics diagnostic of NSR.

If the mapped features are likely to be somewhat imperfect matches to the NSR stresses due to local stresses, pre-existing fractures, and other small and generally random deviations from our model system, and given how easy it is for any relatively straight feature to appear consistent with NSR for some amount of shell rotation, we should not expect to be able to differentiate between a feature which fits NSR well because it was caused by NSR and one which fits NSR well by chance.

Instead of looking how well a map M fits NSR (e.g. via the metric $Q(M)$ defined above), we can also ask whether there are any properties of a set of lineaments which we would consider more or less consistent with the hypothesis of NSR. Any property diagnostic of NSR should yield a positive result for the collection of synthetic NSR features, and negative results for both the random great circle segments and the randomized map, which we know have nothing to do with NSR.

As mentioned above, synthetic NSR lineaments (e.g. Fig. 3.11) have very low sinuosities. The randomized maps share this quality marginally, to exactly the same degree as our original map. The great circle segments have sinuosities of zero. Low sinuosity is necessary to fit NSR, but it is not sufficient, as there are many possible low sinuosity features which do not fit NSR, making it a poor diagnostic.

A conspicuous lack of north-south oriented lineaments in the equatorial regions, as seen in the synthetic NSR map, might indicate that a map results from the NSR stresses. Both the great circle segments and the randomized map have many such lineaments. However, so does our map, and so on that basis it seems unlikely to be related to NSR.

The perfect map also has less cumulative lineament length per unit area in the equatorial regions than in the mid and high latitudes because tensile fractures are precluded from forming in the compressive zones. Both the great circles and the randomized map have uniform lineament density globally, and so also when longitudinally averaged. Our mapped dataset actually has a tendency toward *increased* lineament density in the equatorial regions when longitudinally averaged.

Probably the most unusual thing about Fig. 3.11 is the fact that the lineaments consistently avoid crossing each other. This is the result of their having been created simultaneously, without any shell rotation taking place between the formation of subsequent features. This is an extreme case of a non-uniform activity history. Both types of randomized maps have relatively featureless activity histories, and one can imagine maps which really do result from NSR stresses also having flat histories. If the shell's rotation period is significantly shorter than the time it takes to erase a feature, we would expect their best-fit backrotations to be distributed uniformly, but if the shell rotates slowly compared to the lifetime of a feature, then we may see evidence of transient activity, or the processes which

determine a feature's lifetime, expressed as a non-uniform apparent history. Even subtly non-uniform activity might still be informative if it can be shown to be sufficiently unlikely.

3.3.4 The activity history of our map is very unlikely.

The apparent activity history $H(b)$ which we infer from the mapped features can be seen in Fig. 3.13. It has a peak at $b = +30^\circ$. In comparison to the suite of randomized maps whose activity histories are also shown in that figure, the amplitude of the peak is quite large, and so our map does appear to distinguish itself by having an unusually non-uniform history. *McEwen* [1986] found using Voyager imaging that in aggregate the best fit of the visible features with lengths greater than 20° of arc on the surface was at $b = -25^\circ$, however, that work was comparing the mapped features to an NSR stress field comparable to the viscous endmember, in which $\Delta \gg 1$ and there exists a $\psi \approx 45^\circ$ lag between the potential and the stresses, with the pattern of stresses shifted to the west. In order to compare the two results directly, we need to subtract that 45° from our calculated b values. This means our peak at $b = 30^\circ$ is comparable, in the case of a viscous ice shell, to a peak at $b = -15^\circ$. Given the much larger set of lineaments we include in our analysis, and the differences between our method of comparing stresses to and that of *McEwen* [1986], this amount of disagreement does not seem worrisome.

While we tried to demonstrate that our map of Europa's lineaments is not geographically biased by any of the observational variables discussed in section 3.2.1 and pictured in Figs. 3.3, 3.4, 3.6, and 3.5, it still might be the case that some coherent subset of the map is exerting disproportionate influence over $H(b)$. One visible candidate is the E15REGMAP01 high resolution pole-to-pole imaging swath. These observations between 60°W and 120°W (see Fig. 3.1) look as if they might be predisposed toward the range of b values in which we see enhanced

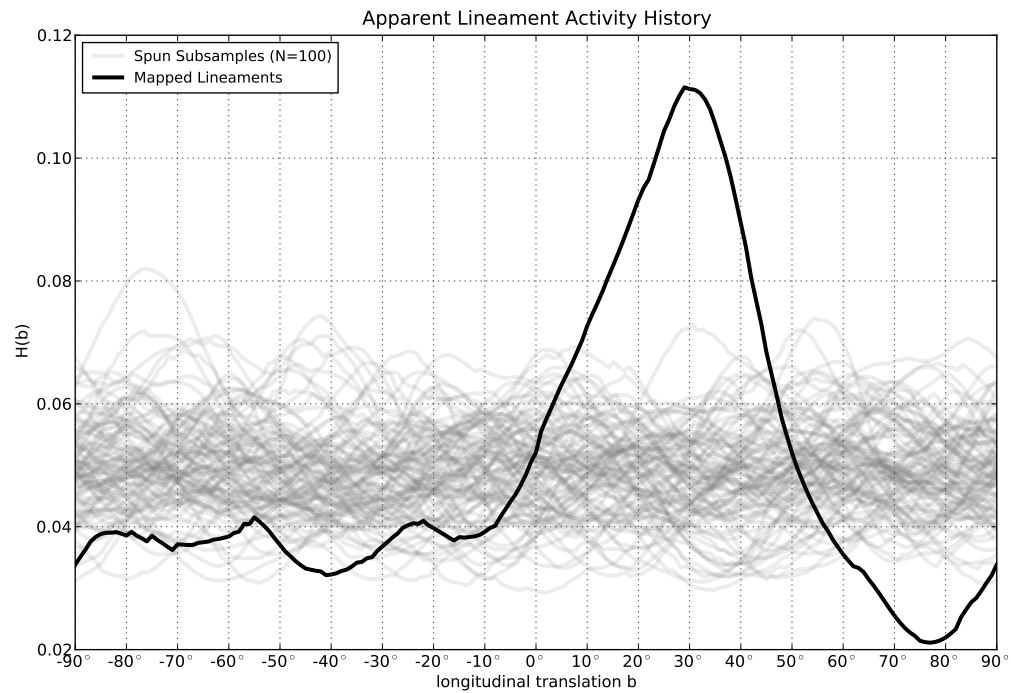


Figure 3.13: The heavy black line is the apparent history of activity $H(b)$ which we infer from our map. The diffuse gray lines are a suite of synthetic lineament maps, each made up of 661 features drawn with replacement from the set of mapped features, and random in longitude. The amplitude of the real map's $H(b)$ curve is very greater than we would expect, based on the randomized curves.

activity. When we remove this swath and plot the resulting activity history (in Fig. 3.14) we see that the $H(b)$ curve for the map without the E15 swath is still generally within the envelope of uncertainty for the map as a whole (compare also with the activity history inferred from the southern portion of the E15 swath, in Fig. 4.10).

In addition to subdividing the set of mapped lineaments geographically, we can segment the dataset based on the values of other lineament characteristics to see if the peak above is present consistently, or limited to some subpopulation. Figures 3.15 and 3.16, show the activity histories of the mapped lineaments separated according to length and sinuosity respectively. The same range of b values displays enhanced activity for all of the different length bins, as well as for the lower sinuosity lineaments making up the overwhelming majority of the cumulative length within the dataset. It also seems possible that the trough at $90^\circ < b < 60^\circ$ is a significant feature consistent across all these subdivisions of the map.

The map displays the same general $H(b)$ curve regardless of what value we choose for \bar{D}_{max} , as the curves are in Fig. 3.17 show. Unsurprisingly at very small (and thus strict) values of \bar{D}_{max} the fact that we have excluded the overwhelming majority of the dataset begins to be an issue, but even down to $\bar{D}_{max} = 0.05$ the major features of the curve are intact. They remain visible but are progressively more muted up to the largest possible value, $\bar{D}_{max} = 0.25$.

A very general measure of the non-uniformity, or dispersion, of any probability distribution or sequence of values having a finite, non-zero mean, such as our calculated $H(b)$, is their *relative mean difference*, or RMD. The RMD is the magnitude of the mean difference between two samples chosen at random from the sequence, normalized by the mean value of the sequence. The most commonly encountered measure of dispersion, the standard deviation σ , can only be applied

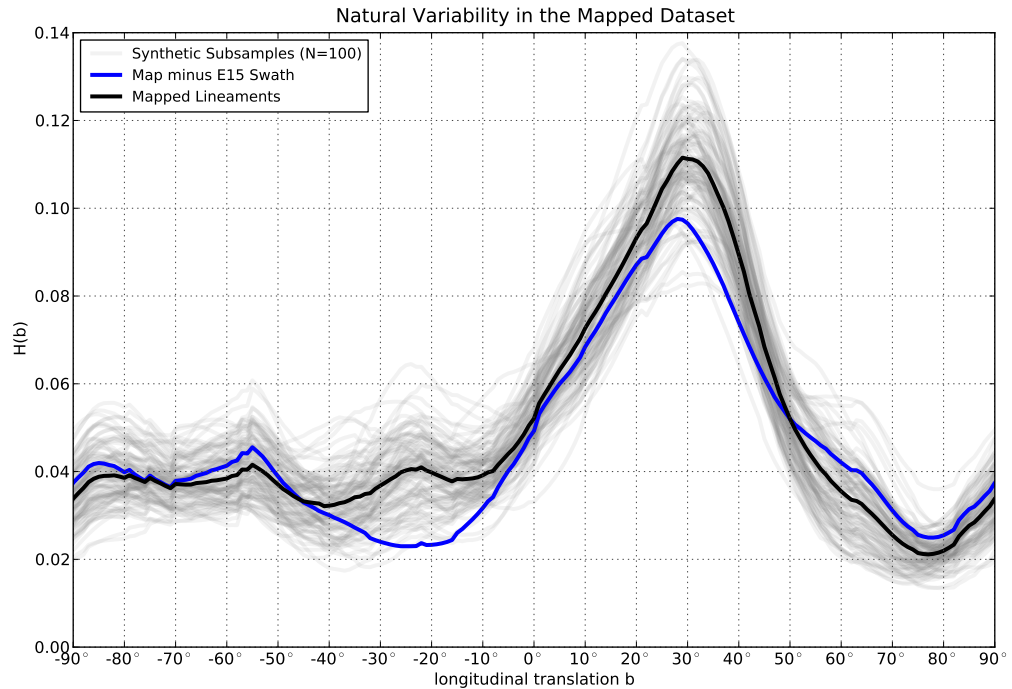


Figure 3.14: Activity history for the mapped features compared to a suite of Monte Carlo resamplings, estimating the dispersion within the dataset. The blue curve is the inferred activity history of the map minus the E15 region, which is comprised of all the features lying between 60°W and 120°W (see Fig. 3.1). The removal of the E15 swath does not have a significant effect on the overall shape of the map's $H(b)$ curve. Compare with Fig. 4.10 which shows the inferred history from the southern portion of the E15 swath itself.

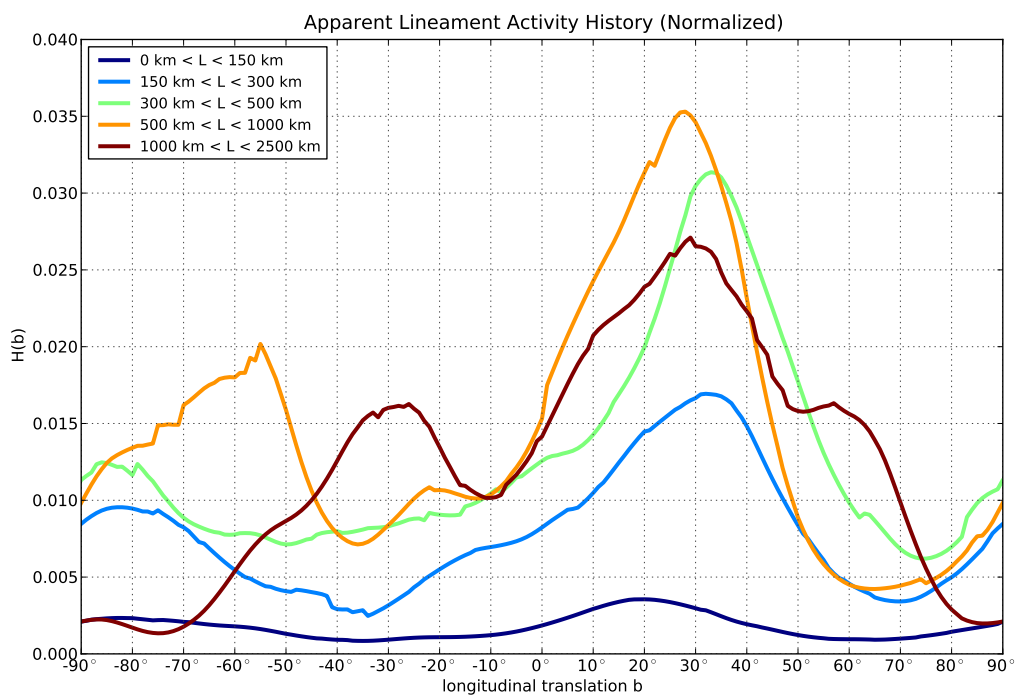


Figure 3.15: Activity histories for the mapped features in their current locations, broken into separate classes depending on the length of the features. Most of the classes have similar histories. The amplitudes of the different curves indicates what proportion of the overall dataset each subclass represents.

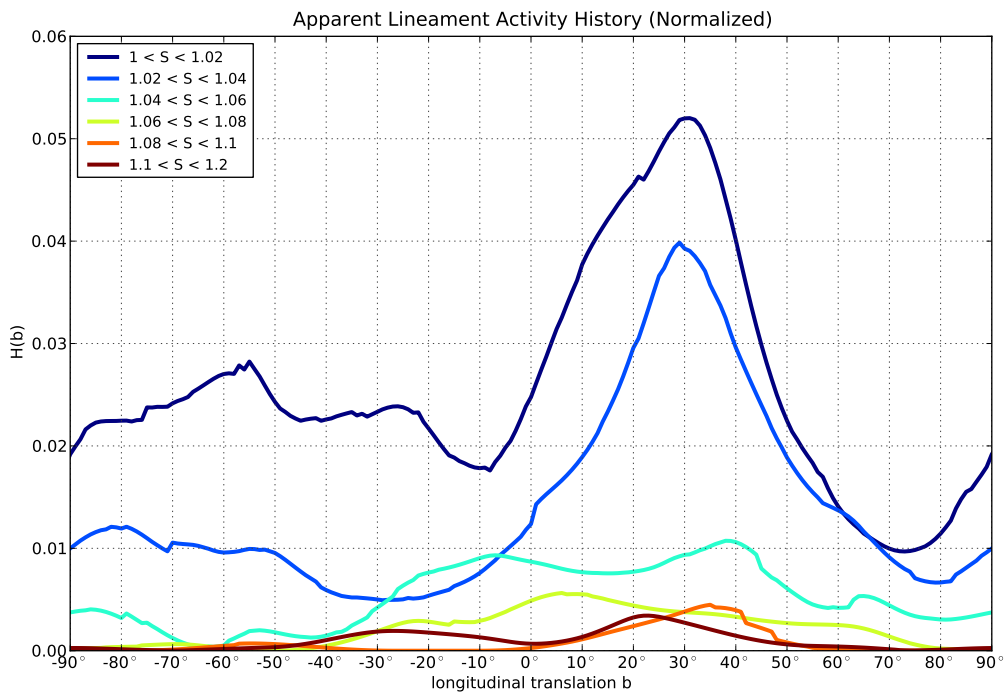


Figure 3.16: Activity histories for the mapped features in their current locations, broken into separate classes depending on the sinuosity of the features. Most of the sub-populations contribute to the peak at $b = +30^\circ$. The amplitudes of the curves are indicative of the proportion of the overall dataset made up of each subclass.

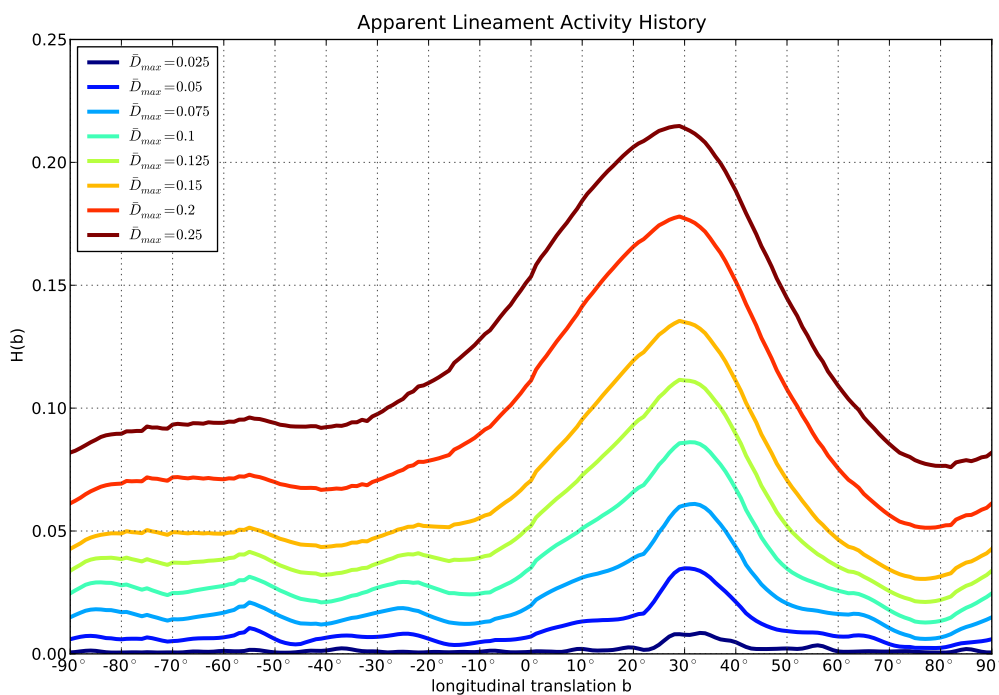


Figure 3.17: Different inferred activity histories for the mapped features in their current locations, as a function of the chosen value of \bar{D}_{max} . Even down to the very strict value of $\bar{D}_{max} = 0.05$ the major features of the curve remaining intact. They become progressively more muted up to the largest possible value, $\bar{D}_{max} = 0.25$.

to unimodal distributions with a central tendency, which is not necessarily what we expect to see with $H(b)$. In our application it makes sense to use the RMD, instead of just the mean difference because when lineaments fit NSR better on average (increasing the mean of the distribution), all else being equal, we ought to expect the dispersion in $H(b)$ to increase as well. This is because both perfect and imperfect NSR features have a minimum possible $H(b)$ value of zero (if some portion of the inferred history has no apparent activity). At the same time, the maximum possible value of $H(b)$ will increase as the quality of the fit between the lineaments and the features increases. Here we are interested in the component of the magnitude of the variation in $H(b)$ that comes from a concentration of activity within some range or ranges of b values, and not in the portion of the magnitude that results from the map being capable of fitting NSR better. Given a finite sequence y_i for $i = 1$ to n , the RMD is:

$$RMD(Y) = \frac{\sum_{i=1}^n \sum_{j=1}^n |y_i - y_j|}{(n-1) \sum_{i=1}^n y_i} \quad (3.14)$$

To determine whether the moderate peak we see in the activity history of our mapped features is statistically significant we need to estimate the distribution of $RMD(H(b))$ values which one would expect to see by chance. Thus we created several large populations of lineament maps for comparison, and calculated $RMD(H(b))$ for each of them. The resulting distributions can be seen in Fig. 3.18.

3.3.4.1 The Spin Cycle

The first population of maps randomizes the longitudinal location of each of the mapped features independently, preserving their latitude, shape, and orientation. This is computationally cheap because their individual fit curves $f_{nsr}(b)$ do not have to be re-calculated. Instead they are simply shifted in b along with

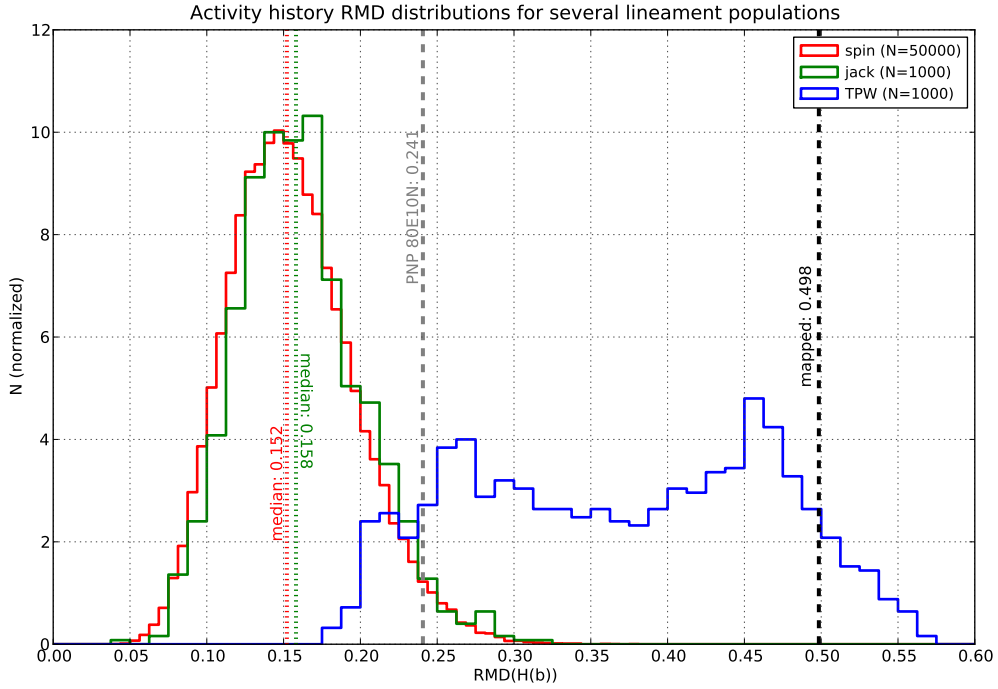


Figure 3.18: The relative mean difference (RMD) is the metric we are using to describe the non-uniformity of the apparent activity history of a set of mapped features as a function of shell rotation ($RMD(H(b))$). Here we see three different populations of maps and their distribution of $RMD(H(b))$ values. The blue distribution is made up of the mapped global lineaments, transformed according to 1000 different paleopoles, evenly spread around the globe. The green and the red curves are for two different kinds of randomizations of the map. In red is purely longitudinal randomization (of the kind used to generate the gray curves in Fig. 3.13), and in green complete randomization of location and orientation. The similarity of these two populations suggests that purely longitudinal randomization (which can be done much faster) is sufficient. The thick dashed line at $RMD(H(b)) = .499$ corresponds to the global lineaments undergoing NSR about the current pole. It is far out in the tails of the randomized distributions, indicating that the non-uniformity of the global map is not random chance. It is also near the upper end of the TPW population, but it seems likely that a significant portion of the TPW distribution has an $RMD(H(b))$ which is statistically equivalent to the current pole, and so this measurement is unlikely to argue persuasively for any particular pole of rotation.

the lineament and summed again to generate a new $H(b)$ curve. However, this population will preserve any bias that our mapped dataset has in the distribution of the features in latitude, and so may not represent a truly random distribution well.

The most non-uniform theoretically possible activity history within this population corresponds to the map pictured in Fig. 3.19, in which each of the mapped features has been shifted to the location within the stress field which it best fits. That map yields $RMD(H(b)) = 1.66$. The histogram of $RMD(H(b))$ values for 50,000 samples from this population is shown in 3.18. It has a median value of $RMD(H(b)) = 0.152$, and the right hand tail extends only as far as $RMD(H(b)) \approx 0.312$.

3.3.4.2 Playing Jackstraws

The second population of maps we created are similar to the one shown in Fig. 3.12, consisting of a sampling, with replacement, of the mapped dataset, having the same number of features as the original map. The chosen lineaments are then scattered uniformly over the surface, with random orientations. Calculating $H(b)$ for these maps is more computationally intensive than the first population above, but completely randomizes the location and orientation while maintaining the same distribution of lengths, sinuosities, and shapes as our original map. The resulting distribution (with $N=1000$) is also shown in Fig. 3.18 and is very similar to that of the first population, with a median $RMD(H(b)) = 0.158$, and an extreme right hand tail extending to slightly greater values, despite the much smaller number of samples.

Although we cannot precisely quantify the probabilities as we do not know the true underlying distribution (it is visibly non-Gaussian), if drawn from either of the above two populations, our map, with $RMD(H(b)) = 0.499$, is exceedingly

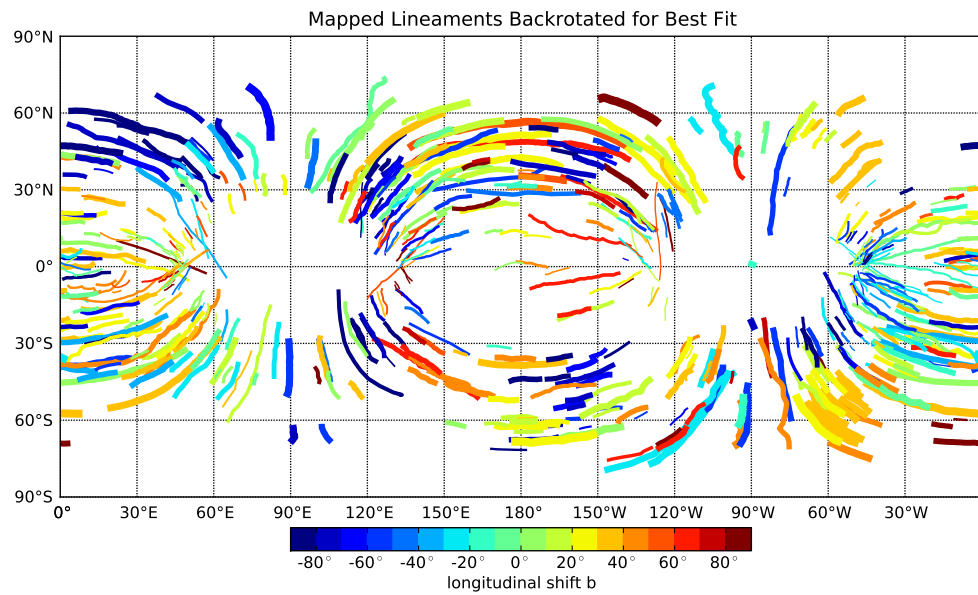


Figure 3.19: A map similar to that shown in Fig. 3.1, but with all the lineaments transformed to the longitude at which they best fit the NSR stress field, or equivalently, translated to show their location relative to the stress field at their most likely apparent time of formation.

unlikely to be the result of random chance.

3.3.5 The current pole of rotation may not be special.

Finally, we explored the behavior of $RMD(H(b))$ for maps which simulate a TPW event, preserving the locations and orientations of the lineaments relative to each other, but transforming their overall positions in tandem. Figure 3.20 shows how $RMD(H(b))$ varies as a function of paleopole location, with 1000 randomly selected paleopoles scattered uniformly across the surface of the satellite. A histogram of the resulting $RMD(H(b))$ values is shown in Fig. 3.18.

3.3.5.1 Moon Tipping

The hypothesized pre-TPW map pictured in Fig. 3.7, with its paleopole located today at 80°E , 10°N as suggested by [Schenk *et al.*, 2008], has $RMD(H(b)) = 0.241$, which is well within the upper shoulder of $RMD(H(b))$ distributions for the randomized lineament populations discussed above, and smaller than $\sim 90\%$ of the $RMD(H(b))$ values calculated for possible paleopoles, as can be seen in 3.18. The present day pole of rotation yields $RMD(H(b)) = 0.499$, far larger than random chance can explain. How do these values compare to the range of possible values if we assume the freedom to re-orient the map as a whole however we wish?

The map of $RMD(H(b))$ values as a function of paleopole location in Fig. 3.20 and the histogram in Fig. 3.18 show that the modern pole is fairly close to having a maximal $RMD(H(b))$, beating out 90% of the samples calculated globally. However, it is unclear how statistically significant this result is. To find out, we would need to use a bootstrap Monte Carlo method to estimate the uncertainty on the measured value of our present-day map's $RMD(H(b))$, and thus the likelihood of our dataset happening by chance to generate a peak in

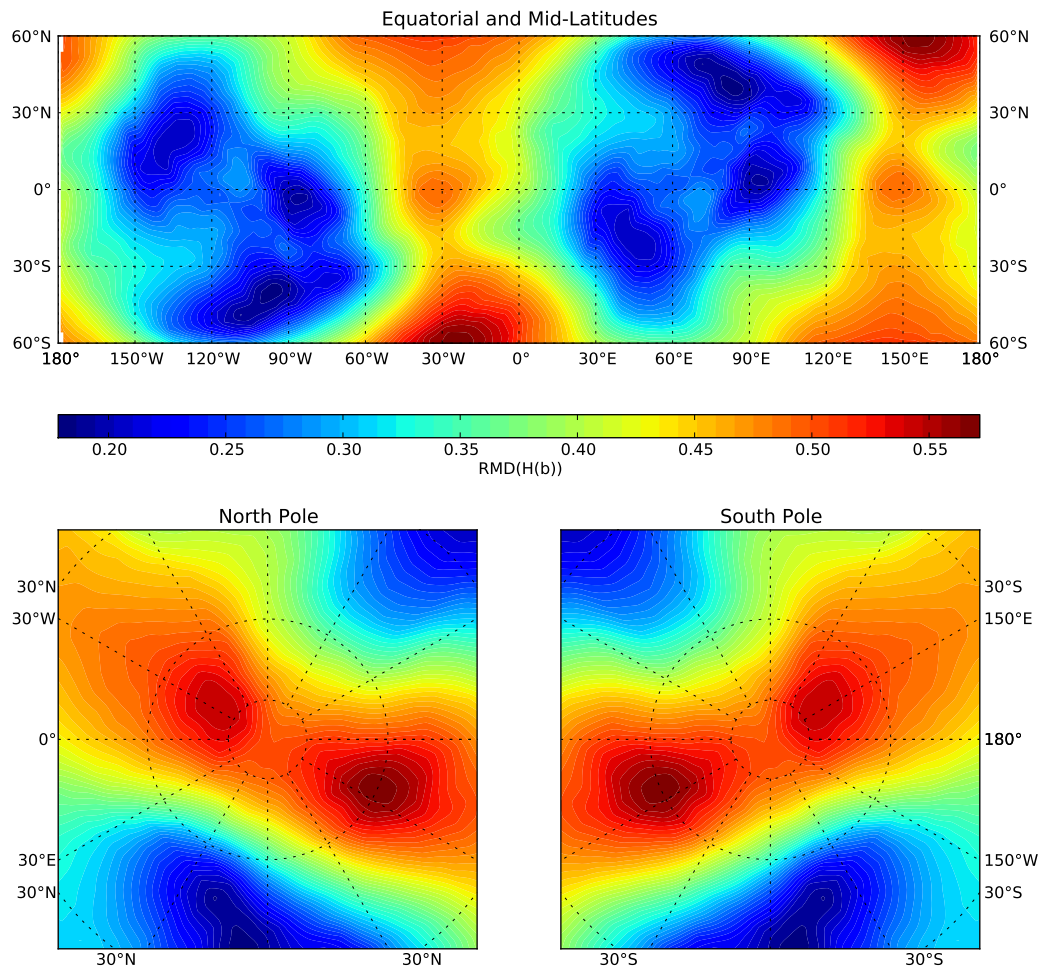


Figure 3.20: The non-uniformity of the apparent NSR lineament activity history, as measured by $RMD(H(b))$ for the mapped features re-oriented to 1000 possible paleopoles of NSR, uniformly distributed over the surface of Europa. The current pole of rotation results in an RMD greater than that of $\sim 90\%$ of the possible poles, but the statistical significance of this fact has not yet been measured. It may be that a fair proportion of the possible poles are statistically indistinguishable from the current one.

$RMD(H(b))$ like the one we observe near 70°N , 150°E , where $RMD(H(b)) = 0.57$. If that value is significant, then this map may be taken as support for the hypothesis that the features we mapped are the result of NSR that took place about that other pole. On the other hand, if that maximally non-uniform pole is *not* significant, then it is likely that at least one third of all possible paleopoles result in $RMD(H(b))$ values which are equivalent to that of the current pole, and our map cannot help us much in discriminating between possible paleopoles.

3.4 Conclusions

Our initial assumptions were that non-synchronous rotation of the ice shell has taken place, that it has been a dominant source of stress in Europa’s lithosphere, and that the tectonic features we see are primarily the result of tensile fractures. If these assumptions are valid our results suggest several scenarios, and provide evidence against others. However, in light of how difficult it is to conclusively link any individual feature to NSR, it may be prudent to re-examine those assumptions.

3.4.1 Three stories about NSR

There are many ways one might envision NSR being responsible for the particular $H(b)$ curve we observe in the mapped features. Here we describe three possibilities; they are not mutually exclusive, and might well have occurred in parallel.

It is important to note in interpreting these curves that the $\overline{D}(b)$ values which we are measuring are a function of where relative to the NSR stress field we synthesize our hypothetical lineaments, and so are affected not only by how much shell rotation has taken place since the lineament formed, but also by the phase shift separating the potential and the stress field, as discussed in Section

2.6.3. In effect, the b we are measuring is really:

$$b = -(\psi + x_{nsr}) \quad (3.15)$$

where ψ is the phase shift, and x_{nsr} is the longitudinal translation due to non-synchronous shell rotation (with all quantities taking east as positive). Somewhat counterintuitively this means that, for example, a lineament with a minimum $\bar{D}(b)$ at $b = +30^\circ$ (i.e. to fit the elastic NSR stresses, the feature must be shifted 30° to the east) could still have been formed in the recent past if the shell is undergoing prograde NSR, because the stresses may be displaced up to 45° to the west, depending on the value of Δ_{nsr} .

Because the NSR stress field is periodic, repeating every 180° of longitude, it is not possible to determine whether a particular feature formed in the most recent shell rotation or in the more distant past. Because we do not know for certain whether the shell's rotation is prograde or retrograde, we cannot know whether the features are being placed in chronological, or reverse chronological order. However, additional information, such as the cross-cutting relationships between features discussed in Chapter 4, may help clarify these issues.

3.4.1.1 Steady state formation, activity, quiescence, and erasure.

In this formation scenario, it is important to conceptually disentangle lineament formation from visibility. By *formation* we mean the fracturing of the ice, which ultimately determines the shape of the feature. The trajectory of the fracture is a function of the NSR stresses at the time the ice breaks. The fracture may or may not become *visible* immediately after formation. So long as the ice does not anneal, the feature may become active and thus visible at a later date. This delay could conceivably be a significant fraction of the shell's NSR period.

For instance, if the ridges and lowered albedo associated with the lineaments

are the result of shear heating [Nimmo *et al.*, 2007], the time between formation and visibility would be determined by how long it takes for friction in the fracture to raise the temperature to the threshold at which the surface expression of that heating becomes apparent. Visibility might also be more directly dependent on the re-orientation of the ice shell, with shear heating only becoming significant after a fracture has rotated into a region of the NSR stress field where the most tensile principal component is no longer orthogonal to the fracture, allowing greater pressures build up across it, enhancing frictional heating.

Whether a lineament ended up in our map is a discrete event. Either it was mapped (because we could see it) or it wasn't (because we couldn't) but whatever process leads to a fracture becoming visible is likely to be continuous, with the feature's probability of being mapped increasing as that process acts over time. Thus we can imagine a scenario in which a fracture forms and immediately becomes active, but only gradually becomes visible. The longer it has been active, the more visible it becomes, and the greater the likelihood that it is included in our map. This would result in $H(b)$ increasing with b , as we see in the first 30° of the activity history for our mapped features.

Imagine then that after some finite period of activity, which is significantly shorter than the rotation period of the ice shell, the feature becomes quiescent. The rate of resurfacing then becomes the primary determinant of visibility, and the feature slowly fades into the background as it is overprinted by new fractures and the ensuing ridges, and as sputtering of the water ice by energetic particles deposits bright frost, obscuring albedo features. This results in $H(b)$ decreasing as b increases, and in combination with the gradual increase in prominence described above, could generate a local peak in $H(b)$ like the one that we see.

The shape and size of this peak would depend on the rate of fracture formation, the active lifetime of the features during which visibility increases, the rate

at which visibility increases while active, the rate at which visibility is decreased by resurfacing processes once a feature becomes quiescent, and the rotation period of the shell.

There is no *a priori* reason to expect that the rates at which lineaments become visible and at which they are erased ought to be comparable, but in this scenario, the fact that the peak we see in $H(b)$ is nearly symmetric would seem to suggest that they are. This might be the case if the primary resurfacing process were overprinting by new lineaments (as opposed to e.g. impact cratering or frost deposition). If that were true, then older features (which formed at larger values of b) might on average be shorter than newer ones, as they are progressively bisected by newly superimposed lineaments, resulting in a negative correlation between lineament length and the value of b which results in the best fit to the NSR stresses. It turns out that for the dataset as a whole these variables are entirely uncorrelated, with $R^2 < 0.01$.

One could imagine that far beyond the peak you would see a kind of saturation, after which discrete resurfacing events would no longer reduce the average length of mapped features, or that in the case of a delay between fracture formation and feature prominence, that the side of the peak toward $b = 0^\circ$ would not have this correlation, but it is not even present for the subset of the mapped features which have $\min(\bar{D}(b))$ with $30^\circ < b < 60^\circ$ where within this scenario we would expect erasure to be the dominant process. If instead resurfacing takes place homogeneously, for example by frost deposition, we might not expect to see any correlation between the b which minimizes $\bar{D}(b)$ and feature length, but we would also not expect to find roughly the same rates for both the increase and decrease in feature visibility.

However, we know there are significant number of features in the map which cannot be the result of tensile fracture due to stresses from NSR about the current

pole. Any lineament in the equatorial regions oriented largely north-south must be the product of some other process. This suggests that some proportion of the overall map outside of the equatorial regions may also be unrelated to NSR. To get some idea of the minimum fraction of NSR lineaments that would have to be from NSR in order for us to get a peak like the one we see, we can create a series of synthetic datasets mixing together randomized features and NSR features, and compare them to our observed dataset. The results of one such analysis can be seen in Fig. 3.21. The gray curves which envelop the $H(b)$ curve for our mapped dataset were generated by subsampling the mapped dataset, with 60% of the features having randomized longitudes, and 40% of them being assigned b values having a normal distribution with a mean of 30° and a standard deviation of 15° . Activity histories similar to the one we observe can thus be the result of only a minority of the mapped features contributing to the peak, meaning that the lack of a correlation between best-fit b and lineament length on the downward slope of the peak in activity should not be taken as strong evidence against this scenario. Interestingly, the width and height of the observed peak cannot be reproduced without introducing a significant dispersion into the distribution of translations, which suggests that the peak records a significant interval of activity, and not a single spike.

3.4.1.2 An isolated episode of lineament formation

In contrast to the steady state, uniformitarian explanation above it is also possible to get a peak in $H(b)$ through a singular episode of lineament formation and features which become visible on a timescale short compared to the rotation period. To do so, it must be possible for the shell to sometimes rotate without creating new fractures, otherwise there would always be significant activity apparent for small values of b . At first this might seem surprising, as our entire hypothesis

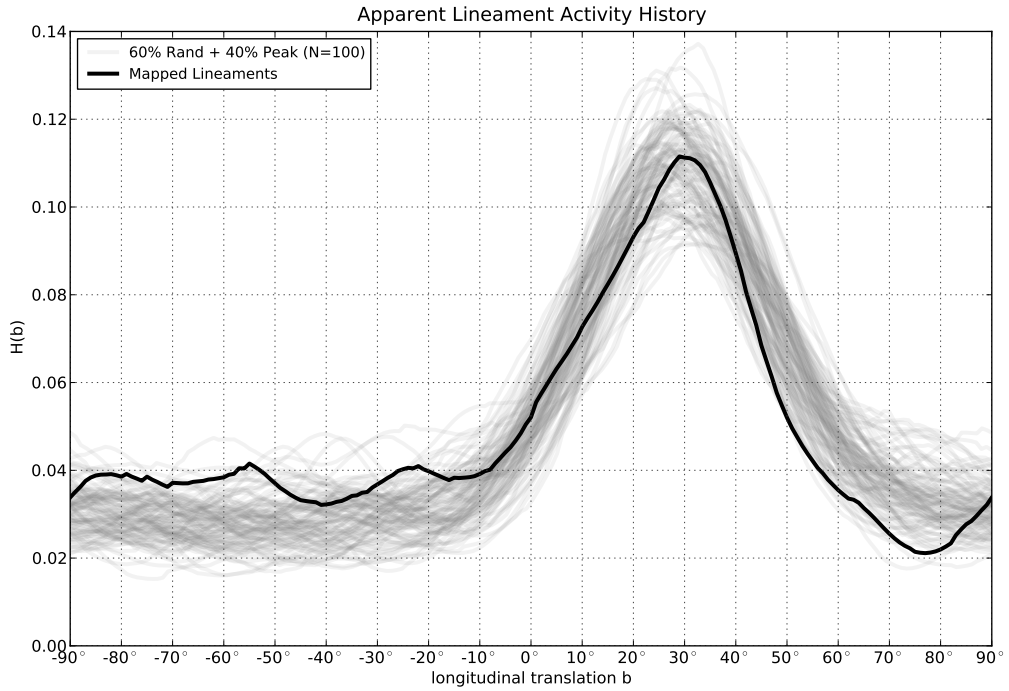


Figure 3.21: To estimate the minimum fraction of the mapped lineaments that would have to be from NSR to generate a peak in $H(b)$ like the one we see, we created a series of synthetic datasets mixing two populations of lineaments, both subsampled from the set of mapped features. The first population has been translated by a random amount in longitude, and the second has translated by their best-fit value of b , plus a random value drawn from a normal distribution with a mean value $\mu = 30^\circ$, in order to align their peak in apparent activity with that of the mapped dataset. We then varied the standard deviation σ of the normal distribution, and the mixing ratio of randomized and coherent lineaments to find a combination which was consistent with the $H(b)$ curve of the map. The gray curves shown here correspond to populations made up of 60% randomized features, and 40% normally distributed coherent features with $\sigma = 15^\circ$. Activity histories similar to the one we observe can thus be the result of only a minority of the mapped features actively contributing to the peak. The width and height of the observed peak cannot be reproduced without a significant dispersion in the amount of translation added to the coherent fraction.

relies upon rotation of the shell generating the stresses responsible for the lineaments, but the creation of fractures is dependent on the ice shell's response to the NSR stresses being elastic. If instead the response is sometimes viscous, then it may be possible for the shell to rotate and effectively relax away the resulting stresses, avoiding the formation of new features. This would suggest that around $b = 30^\circ$ the shell experienced a period of elastic response, and that for most of the subsequent rotation the response has been viscous.

Transitions between the two types of response might conceivably be related to transitions between convective and conductive heat transport within the shell, and the corresponding change in the shell's temperature profile, or to periodic episodes of significant tidal dissipation. Changes in the shell's temperature profile might also influence how feature visibility evolves with time, as faults and fractures that have propagated to a given depth would be exposed to different temperature ice in the two regimes.

3.4.1.3 Phase lag in a viscoelastic shell.

Confusing both of the above scenarios is the possibility of a viscous phase lag as described in Chapter 2 and *Wahr et al.* [2009]. For a significant range of plausible values of Δ (Eq. 2.22), tensile NSR stresses remain large (\sim MPa), but lag the tidal potential because the shell's response is not instantaneous. This phase lag is capable of shifting the peak up to 45° in longitude from where we would expect to see it for elastic stresses. This effect cannot necessarily be disentangled from the displacement of the peak by a delay between formation and visibility. Both processes act to increase the magnitude of the value of b which we measure. Shell rotation does this by shifting the features in the direction that the shell is turning. Viscous relaxation does it by translating the pattern of stresses in the opposite direction as the shell is turning, giving us the relationship mentioned

above, $b = -(\psi + x_{nsr})$.

Assuming prograde NSR means $x_{nsr} \geq 0^\circ$ and $-45^\circ \leq \psi \leq 0^\circ$ which implies $0^\circ \leq x_{nsr} \leq 15^\circ$ and $-45^\circ \leq \psi \leq -30^\circ$. Looking at Fig. 2.2c, we can see that this would correspond to $\Delta_{nsr} \geq 1$, yielding maximum tensile stresses due to NSR of ~ 1.75 MPa. If instead we assume retrograde NSR, meaning $x_{nsr} \leq 0^\circ$ and $0^\circ \leq \psi \leq 45^\circ$, then all possible values of ψ are available, and all we can say is that $-75^\circ \leq x_{nsr} \leq -30^\circ$. In both of these scenarios, we are assuming the direction of shell rotation has been consistent throughout the period recorded by the lineaments, and that less than 180° of shell rotation has occurred since the lineaments responsible for the peak in $H(b)$ formed.

3.4.2 Things that didn't happen on Europa.

Some have suggested that the cross cutting relationships between lineaments indicate that many shell rotations have taken place and are recorded by the prominent visible surface features [Sarid *et al.*, 2004; Hurford *et al.*, 2007]. The apparent concentration of activity within a small contiguous subset of the distinguishable b values argues against this possibility. Obtaining our localized peak in $H(b)$ while preserving features from many subsequent rotations of the shell would require a periodicity in the rate of lineament formation, with enhanced activity having taken place every $n \times 180^\circ$ (where n is an integer). It seems to us more plausible that old features sometimes re-activate, confusing their pre-existing superposition relationships, or that the NSR stresses are not everywhere and always so dominant as to preclude the formation of lineaments having other orientations. It is especially easy to change the expected orientation of failure in regions with nearly isotropic stresses, and the fact that we can reproduce the observed non-uniformity in $H(b)$ with only 40% of the features contributing to the peak suggests that we would do well to admit our dataset is unlikely to be well explained by a single

cause.

Our results also argue against the hypothesis that the surface records tensile fractures resulting from NSR about any pole other than the current one, including the suggested paleopole at 80°E, 10°N [Schenk *et al.*, 2008]. This is not to say that TPW has not occurred, but rather that if it did, we have no strong indication from the mapped features of NSR prior to the re-orientation event.

3.4.3 Reconsidering our assumptions

We can confidently say that some of our initial assumptions are wrong, at least some of the time, because we see north-south features in the equatorial regions. Thus we know the shell must have experienced significant stresses other than NSR, failure modes besides tensile fracture, or tensile fracture due to NSR while rotating about some other pole.

Furthermore, we have shown that the existence of lineaments which fit NSR well does not constitute evidence that NSR stresses are present, because while most low sinuosity features fit NSR well at some longitude, low sinuosity alone is not particularly diagnostic of the NSR stresses. In contrast consider the cycloidal ridges, whose shapes have so far only been effectively explained by the time-variable diurnal tides [Hoppe *et al.*, 1999c; Hoppe, 1998; Hurford *et al.*, 2007]. If we limit ourselves to considering purely geographic characteristics (shapes, locations, orientations), then only ensembles of lineaments can be diagnostic of NSR. The only characteristic we have yet found that is potentially diagnostic of NSR and which identifies our mapped features as unusual is the non-uniformity of their $H(b)$ curve. However, there may well be other lineament formation processes capable of producing a similarly non-uniform $H(b)$, meaning that non-uniformity by itself is not necessarily a strong indicator that NSR has taken place.

The fact that only paleopoles within an area covering a small fraction of

the surface near the current pole result in $H(b)$ curves as non-uniform as that of our map is interesting, and provides perhaps the strongest evidence that NSR has taken place, that it has been about the current pole, and that there is no reason to invoke TPW in explaining the lineaments we mapped, but a more robust statistical analysis is really required to assess the significance (or insignificance) of this result.

Non-synchronous rotation may not be the only explanation for our observations, but it is one possibility, and it is not unduly complicated, but we must note that even if we take NSR for granted, there are still several possible stories consistent with our results.

Chapter 4

Geological Superposition Networks

4.1 Introduction

Europa lacks the high density of craters and the well understood impactor population which in combination have allowed us to accurately determine the relative, and in some cases absolute, ages of surfaces in the inner solar system. Fortunately Europa’s extensive system of lineaments provides us with another potential source of temporal information: the superposition relationships visible where two lineaments intersect each other.

A single linear feature may have many intersections with other features along its length, without occupying very much surface area, and so the amount of temporal information potentially available per unit area is very high compared to, for instance, a system of overlapping lava flows which can only intersect other features along their perimeters, or small impact craters, which while plentiful on many planetary surfaces, generally only “intersect” a single geologic unit. In contrast, a long, continuous linear surface feature potentially has the ability to partition the set of features it intersects into two disjoint classes (those which existed before it appeared, and those which formed subsequently) without significantly precluding each of those other features from themselves having a multitude of intersections, further partitioning the set of mapped features into distinct temporal, or stratigraphic, classes.

Careful mapping of Europa's lineaments and the superposition relationships evident at their intersections thus may allow us to infer a great deal about the relative chronology of tectonic activity on the satellite, but only under the following conditions:

- (1) Superposition relationships at the intersections must be clear.
- (2) Mapped features must form a connected network.
- (3) It must be possible to accurately identify segments of lineaments as being part of a single geologic structure, despite the fact that they are periodically interrupted by intersections with other features.
- (4) Individual mapped features must be active along their entire length on timescales which are short relative to the interval between the formation of two intersecting features, otherwise relative times of formation are not well defined.

Furthermore, the amount of temporal information ultimately available from the analysis will depend on several characteristics of the map, including:

- (1) the density of intersections along the mapped features,
- (2) the length distribution of the mapped features,
- (3) the particular geometric arrangement of the features in relation to each other, and
- (4) the order in which the lineaments formed.

The last point may require some explanation. For example, imagine a collection of linear features in which half are oriented north-south, and half east-west,

forming a regular rectilinear grid in which east east-west oriented feature intersects every north-south oriented feature. If all of the north-south features formed before all of the east-west features, then we will not be able to infer anything about the order in which the individual features within one of these classes formed. In contrast, if the order of formation is such that the two classes alternate, with one feature from each being formed at a time, then the order of lineament formation will be completely specified by their superposition relationships.

The amount of information potentially contained in the lineament intersections is large enough that extracting it manually is impractical. Even in a small area, one may find hundreds of lineaments, having thousands of intersections. Disentangling them by hand is labor intensive and error prone. Additionally, it is important to be able to distill and display the most useful information out of this large pool of data. To perform these tasks in a repeatable way, such that human subjective bias is minimized and the limitations of the information extracted can be quantified, an algorithmic approach is desirable. The approach implemented here is generally applicable to any set of features that have clear superposition relationships.

4.2 From maps to graphs

In order to manipulate the map of features and intersections algorithmically, it must be encoded in a data structure representing the relevant information. The natural choice in this case is a construct known in discrete mathematics and computer science as a *directed graph* or *digraph*. A digraph can be visualized as a set of points connected by unidirectional arrows. Each point is known as a node or vertex and each arrow is known as an edge. Nodes and edges may each have data associated with them.

When converting the map to a digraph, each node represents a mapped

feature, and each edge represents a crosscutting relationship. If there exists an edge from node A to node B, it implies that the features A and B intersect each other, and that at their intersection B appears to cross-cut A. The arrow representing the intersection is thus aligned with the arrow of time. We call such a directed graph a geological superposition network, or GSN.

4.2.1 Ideal GSNs

Initially, let us assume that each feature is active for a single span of time that does not overlap the period of activity of any of the features it intersects, and that all intersections allow us to unambiguously identify which feature is superimposed. In this idealized world the graph representing the features and their crosscutting relationships has a particular structure: if one were to traverse such a graph, traveling from node to node along the directed edges, once a given node had been visited it would never again be encountered. This kind of graph is known as a *directed acyclic graph* or *DAG*. An example DAG corresponding to a random synthetic lineament map is shown in 4.1.

DAGs have the property that they can be *topologically sorted*, which means for any DAG there exists an ordering (and usually many orderings) of the nodes such that when the graph is drawn with all of the nodes laid out linearly, according to that ordering, all of the edges in the graph point in the same direction. If one were to traverse a graph so ordered, travel is only possible in one direction down the list. In a GSN the directed edges represent temporal relationships and so when a GSN is topologically sorted, the features are being ordered temporally, to the extent that their order of formation is constrained by their crosscutting relationships.

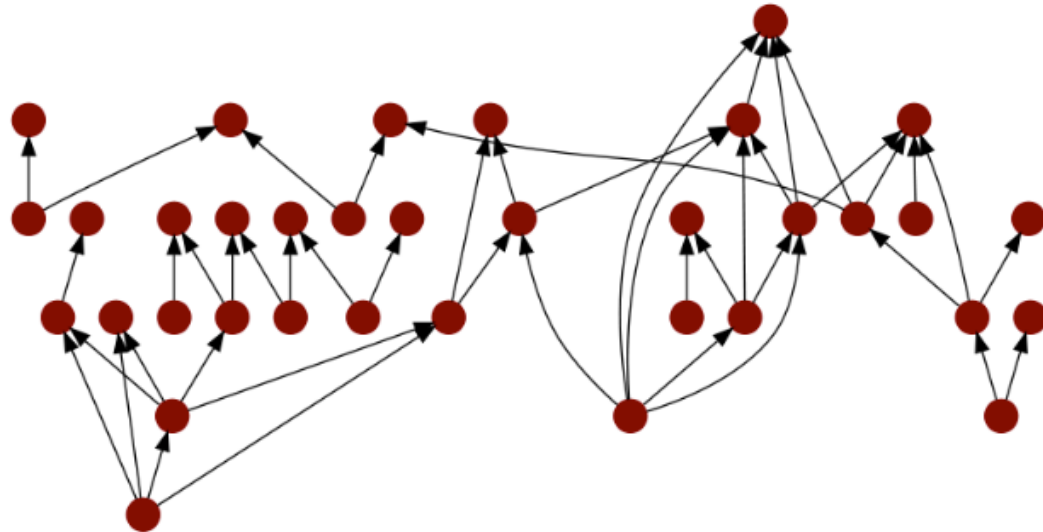


Figure 4.1: A schematic illustration of an idealized acyclic GSN, representing one connected component of a synthetic map composed of random great circle segments, assigned an arbitrary order of formation. Note that all of the arrows point upward, indicating that the vertical ordering is consistent with the mapped stratigraphic relationships. Any rearrangement of the nodes in the graph which results in all the arrows pointing upward is a valid stratigraphy. The synthetic map has 35 lineaments (nodes) and 46 intersections (edges), but because of the additional indirectly implied stratigraphic relationships (paths), about 10% of the 1190 total possible binary ordering relations are defined. This level of GSN completeness is typical for the sparse distribution of lineaments we see at the global scale on Europa. Note that the longest path within this GSN involves only 6 features, and there exist no paths between most pairs of nodes, meaning the map provides no information about their relative times of formation. As the number of features contained in the map increases, it becomes very difficult to draw the corresponding graph in a visually understandable way.

4.2.2 GSNs only yield partial orders

The stringency of the constraints placed on the order of formation will depend on the geometry of the map, and thus the structure of the resulting GSN. Only in exceptional circumstances, such as the example of the rectilinear grid given above, will the order of formation be completely unambiguous, with each feature assigned a unique age, relative to all the others. The vast majority of GSNs corresponding to realistic maps have many valid topological sorts, all of which are consistent with the observed superposition relationships. This means that there is some irreducible ambiguity in the order of formation. We can quantify this ambiguity in at least two ways: first, in terms of the entropy of the system and how much it is reduced as a function of our observed stratigraphic relationships; and second by using the GSN to generate a *partial ordering* over the set of mapped features.

4.2.2.1 Calculating the reduction in entropy

First consider the entropy of the system, S , defined as $-\log(N)$ where N is the number of distinguishable states available to the system, and how much it is reduced as a result of the constraints implied by the observed stratigraphic relationships. For a given set of n features, there are $n!$ possible orderings (states) available. Each observed superposition relationship may exclude some subset of those possible orderings. If in combination, all the observations permit only m possible orderings, then the reduction in entropy ΔS is:

$$\begin{aligned}\Delta S &= -\log(n!) - (-\log(m)) \\ \Delta S &= \log\left(\frac{1}{n!}\right) + \log(m) \\ \Delta S &= \log\left(\frac{m}{n!}\right)\end{aligned}\tag{4.1}$$

If ΔS were readily calculable, it would tell us the information content of the GSN, and place a hard upper bound on the accuracy with which we could reconstruct the original order of feature formation, based on the observed superposition relationships.

Unfortunately, the number of states excluded by a particular observed relationship is in general dependent on what other particular unconstrained orderings have been chosen, which means that counting the states available becomes a problem of combinatorial enumeration: listing possible states and either accepting or rejecting them depending on whether they violate any of the observed constraints. In general, this is not a computationally tractable problem. In some circumstances a sampling approach in which a large number of randomly generated orderings are checked for validity, and the proportions of those accepted and rejected is recorded may produce a decent estimate of how many states have been excluded. Unfortunately, this approach only works when the number of acceptable and the number of excluded states is comparable, i.e. when the system is very poorly constrained. GSNs corresponding to realistic maps containing interesting numbers of features do not usually fall into this category. Instead, they tend to exclude the vast majority of the $N!$ possible orderings (while still admitting an astronomical number of them, in absolute terms), meaning that even if billions of random orderings are tested, absolutely all of them are very likely to be rejected as invalid (even $20!/10^9$ is still $\sim 10^9$, and the high resolution Galileo imaging swaths allow networks consisting of hundreds of features to be mapped).

4.2.2.2 GSN completeness and partial orders

Another much more tractable approach to quantifying the ambiguity remaining after all the visible superposition relationships have been taken into account, is to consider what fraction of the possible binary ordering relations have

been defined by the GSN. In a GSN having n nodes (representing a map having n features) there are $n(n - 1)/2$ possible combinations of two nodes (n_1, n_2). Their stratigraphic relationship is defined if either n_2 is *reachable* from n_1 (denoted n_1Rn_2) or n_1 is reachable from n_2 (n_2Rn_1). If neither node is reachable from the other, then their stratigraphic relationship is undefined. So long as the GSN is a DAG, at most one of these relations will be true. The reachability R is a binary relation which can be intuitively understood in the context of a directed graph as indicating that a path (a continuous series of directed edges) exists from one node to another. More formally it is defined as the transitive closure of the binary relation defined by the ordered sets of nodes which define the edges of the graph.

We call the fraction of the possible relationships which are defined by the GSN its *completeness*, C . How complete a GSN is depends both on the number and the density of intersections along features within the GSN, and so completeness depends indirectly on the length distribution of the mapped features relative to the length scale of the area it covers. Realistic map densities and geometries tend to result in GSNs which are very incomplete. As an example, for the lineaments mapped from the global imaging mosaic used in Chapter 3, or for randomly distributed and oriented great circle segments having a similar length distribution and global average lineament density (length per unit area) with an artificially imposed random order of formation (from which the superposition relationships at the intersections are inferred) in general we find $0.01 < C < 0.1$. Areas with above average lineament densities mapped using higher resolution imaging will result in significantly more complete local and regional GSNs, but even the densely lineated southern portion of the 200 meter per pixel E15 regional mapping mosaic still has $C < 0.25$ (see Fig. 4.2). Ultimately this means that the intuitive goal of creating a global, or even regional stratigraphic column, and assigning many individual features to unique locations in a relative chronology, is not feasible.

Complete relative chronologies can be generated for small subsets of the mapped features, but these chronologies are not sufficiently interrelated to allow much useful generalization.

4.2.3 Using GSNs to corroborate an ordering hypothesis

While we may be unable to construct well defined stratigraphic stacks, there is still a great deal of temporal information encoded in the GSN. The challenge is finding a way to utilize it effectively despite the fact that it is incomplete. One option is to use the incomplete information within the GSN in combination with another dataset or conjecture that implies something about the order of feature formation, and to measure the agreement or disagreement between the two. If the superposition relationships in the GSN are significantly more consistent with the hypothesized ordering than with a null hypothesis of features with a random order of formation, it can be said to corroborate the hypothesis. Conversely if the GSN is significantly less consistent with the hypothesized ordering than chance would predict, it contradicts the hypothesis. In order to use the GSN in this way, we must first be able to unambiguously state an ordering hypothesis, and second we need to define a metric of agreement or disagreement between that hypothesis and the stratigraphic relationships encoded within the GSN.

4.2.3.1 Stating an ordering hypothesis

The most straightforward type of ordering hypothesis would be a total ordering of the mapped features, in which all possible $n(n - 1)/2$ binary relations are defined, and each feature is assigned a unique location in the hypothetical chronology. To state such a hypothesis one needs only to list the features in their hypothetical order of formation, e.g. $(x_1, x_2, \dots, x_{n-1}, x_n)$. The relation x_iPx_j , indicating whether we would expect x_j to be reachable from x_i in the GSN, based

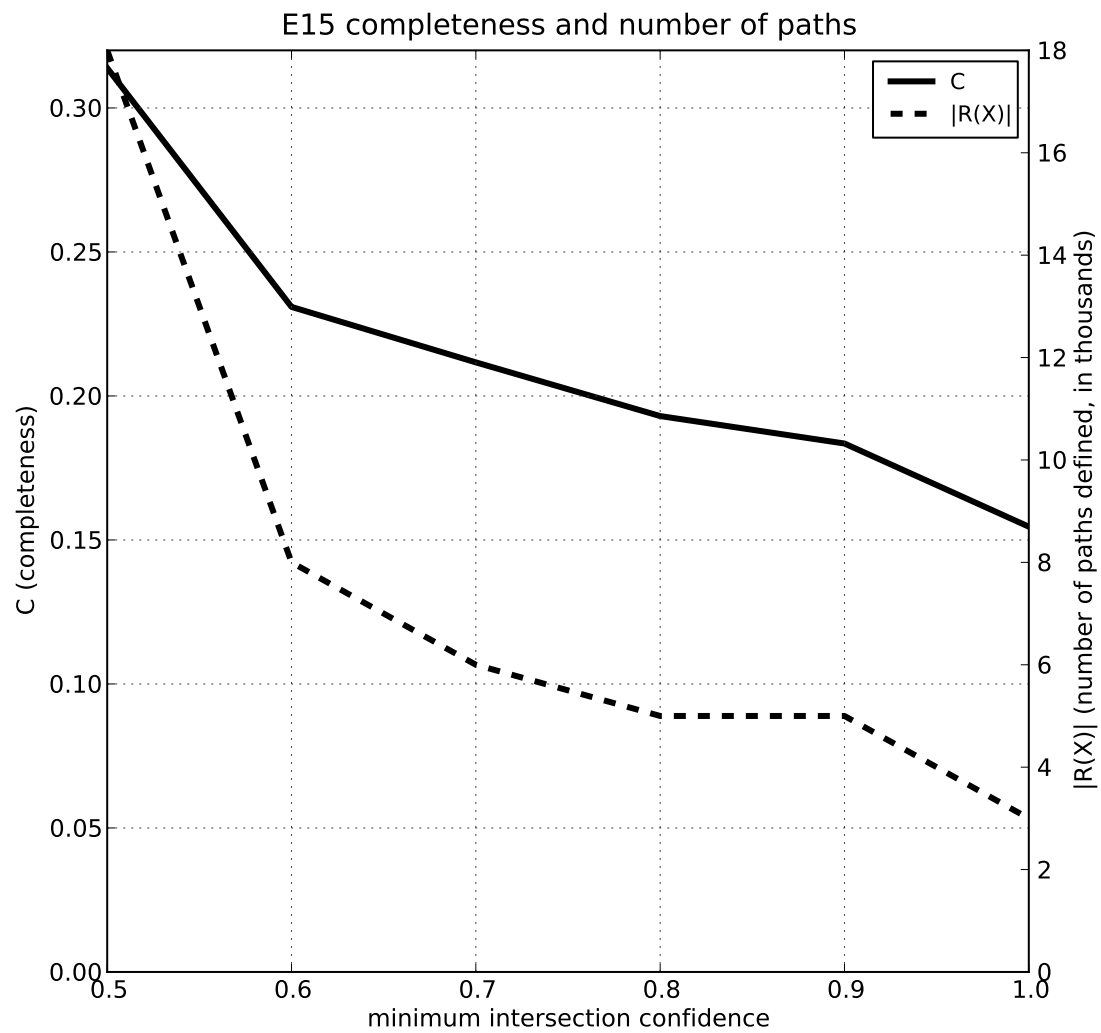


Figure 4.2: The number of paths defined, $|R(X)|$, drops sharply when the $k = 0.5$ intersections are discarded because those edges create a large number cycles in the GSN. The completeness also drops, but by a smaller amount, because those paths excluded primarily have very low confidences, and thus do not contribute much to the GSNs completeness. For the rest of the range the two metrics drop at roughly the same rate as graph connectivity gradually degrades.

on our hypothesized ordering, is true if $j > i$, and false if $j < i$, for $1 \leq i, j \leq n$ and $i \neq j$.

We might also wish to be able to state a hypothesis consisting of only a partial order of the mapped features. This would be the case if we were interested in testing whether a lineament's age is correlated with an apparently discrete characteristic such as its morphology (single ridge, double ridge, triple band), or albedo (bright vs. dark), where we wish to imply a stratigraphic relationship at any intersection involving features from different classes, but do not intend to make any statement about our expectations at intersections between features in the same class. E.g. if our hypothesis is that dark features are younger than bright features, we don't intend to imply anything about the temporal relationship between two bright features, or two dark features, and simply using an ordered list as suggested above with all light features listed before all dark features would spuriously define those intra-class relationships.

Additionally, even if we are investigating the temporal implications of a continuously variable characteristic such as amount of longitudinal translation required to align a feature with the NSR stress field, we might prefer to use a finite number of discrete bins. In the case of NSR, this would make sense because we expect there to be some noise or other coherent stress fields (e.g. resulting from the diurnal eccentricity tides) present in the lithosphere which are unrelated to the NSR tidal forcing, modulating the orientation of failure. In a pure NSR field, two features that formed at nearly the same time would virtually never intersect each other, but with the addition of other more spatially and temporally variable components, intersections become more likely. If we avoid making definite statements about such intersections in our hypothesized ordering by binning the continuous values, we are in effect saying that the uncertainty in our hypothesized ordering is of the same magnitude as the width of the bins. As such, it would be

more accurate to state that uncertainty explicitly, and to only include ordering relations in our hypothesis involving two features separated along the continuum by an interval which is greater than the stated uncertainty. This refinement has not yet been implemented in the analysis discussed below.

So long as we continue to assume that the mapped features correspond to geologic structures having well defined non-overlapping periods of activity, stating a hypothesis consisting of a partial order may be done using a chronologically ordered list of *sets* of features, $(y_1, y_2, \dots, y_{m-1}, y_m)$ where m is the number of distinct stratigraphic classes, and each set y is made up of one or more of the n mapped features, which are considered to be stratigraphically equivalent. The binary ordering relation $x_i Px_j$ is then defined to be true for any $x_i \in y_i$ and $x_j \in y_j$ if $j > i$, and false if $j < i$ for $1 \leq i, j \leq m$ with $2 \leq m \leq n$ and x_i and x_j are said to be *comparable*. If $i = j$ the relation is undefined, and x_i and x_j are said to be *incomparable*. Unless every set y contains only a single feature (i.e. $n = m$) the overall number of ordered binary relations defined will be less than $n(n - 1)/2$, and will vary depending on how evenly distributed the features are across the discrete bins, and how many bins there are.

For simplicity, we will use $P(X)$ (or analogously $R(X)$) to denote the set of ordered pairs of elements $(x, y) \in X$ for which the binary relation xPy is true, and $\overline{P}(X)$ to denote those for which it is false (which is identical to the set of ordered pairs for which yPx is true).

4.2.3.2 Agreement and Significance

Given the set of mapped features X and the partial order $P(X)$ defined by our hypothesized order of formation, in combination with the reachability $R(X)$, also a partial order over the same set of features, but defined by the GSN, we can define the agreement between them as the number of ordering relations which

are true in both orderings, divided by the number of ordering relations which are defined by both orderings, or:

$$A(P, R, X) \equiv \frac{|P(X) \cap R(X)|}{|P(X) \cap R(X)| + |P(X) \cap \bar{R}(X)|} \quad (4.2)$$

implying $0 \leq A(P, R) \leq 1$.

In order to evaluate the significance of a calculated A value, we need to compare it to the range of values which one might reasonably expect to encounter by chance. If our hypothesized order of formation only defines a small fraction of the possible binary ordering relations, i.e. if either $|P(X)| \ll |X|(|X| - 1)/2$ or $|R(X)| \ll |X|(|X| - 1)/2$, then it may not be so unlikely that we would occasionally find $A \approx 1$ or $A \approx 0$ purely by chance. A straightforward null hypothesis is a completely random total ordering of X , resulting in a binary ordering relation $P_{rand}(X)$, but this is not ideal, because in cases where $|P(X)| \ll |P_{rand}(X)|$ the dispersion in $A(P_{rand}, R, X)$ will be much smaller than for $A(P, R, X)$, leading us to erroneously conclude that extreme values of $A(P, R, X)$ are more significant than they really are. A better option is to construct our null hypothesis such that its set of binary ordering relations, $P_0(X)$ has the same size as $P(X)$. One easy way to do this is to ensure that the null hypothesis has the same overall structure as our real hypothesis, i.e. to ensure that for each stratigraphically equivalent set of features $(y_1, y_2, \dots, y_{m-1}, y_m)$ in our real hypothesis, there is a set having the same size in the same location in the ordered list of sets of features $(y'_1, y'_2, \dots, y'_{m-1}, y'_m)$ in our null hypothesis, or for i an integer $1 \leq i \leq m$, $|y_i| = |y'_i|$.

We then calculate $A(P_0, R, X)$ for a large number of such structurally similar instantiations of $P_0(X)$, randomizing which members of X make up the various sets in the ordered list, and from the resulting distribution, calculate the apparent probability that the agreement between our real hypothesized order of formation

and the superposition relationships we have actually mapped is due to chance. It is of course also possible to evaluate the relative strength and significance of two real competing hypothesized orders of formation P_1 and P_2 by looking at $A(P_1, R, X)$ and $A(P_2, R, X)$, in which case some measure of the dispersion σ in the distribution of A values for the null hypotheses corresponding to each of those competing hypotheses can be used as uncertainties on the measurements, with one hypothesis being distinguishably better than the other only when $|A(P_1, R, X) - A(P_2, R, X)| > \max(\sigma(P_1), \sigma(P_2))$.

4.2.4 Real world GSNs

In all of the above, we have been making several assumptions for the sake of simplicity:

- (1) Superposition relationships are completely unambiguous at feature intersections.
- (2) Each feature has a discrete interval of activity which does not overlap the interval of activity of any of the features it intersects.
- (3) Features, when they are active, are active along their entire length.
- (4) Features as mapped accurately correspond to a particular geologic structure.

The result being that the GSN is represented by a directed acyclic graph, or DAG.

In the real world, all of these assumptions are likely false to some degree. Many intersections are somewhat, but not entirely ambiguous, with one of the two possible superposition relationships appearing more probable. We do not know for sure that lineaments are only active for relatively brief, discrete periods of time, along their entire length. Mapping errors may occur when two actually unrelated

geologic structures appear to be one. At the very least, we would like to be able to identify when our assumptions have been violated by our dataset, and we would prefer to be able to adapt the GSN model described above to remain functional even when our assumptions turn out to be imperfectly obeyed.

4.2.4.1 Admitting ambiguity in GSNs

The implication of assuming that the superposition relationships are unambiguous is that the edges in the GSN are unweighted. That is, the existence of an edge is a binary statement: either it's there or it's not, and all the edges which exist are of equal significance, or weight. Similarly, the comparability of two mapped features via the reachability relation R is binary: either two features are comparable or they're not, and it does not make any difference how many separate observed superposition relationships had to exist in combination to ensure that those features were comparable (i.e. how many edges had to be traversed in the graph to connect two nodes). However, we may also construct a GSN with edges having unequal weights, representing the relative confidence which we have in the ordering of the intersections that they represent. The correct method of assigning the numerical values of those weights will depend on how we intend to use the GSN.

We may assign each mapped intersection between two features n_1 and n_2 a confidence $0.5 \leq k(n_1, n_2) \leq 1.0$ representing our (admittedly subjective) estimate of the probability that n_1 is crossed by n_2 . If $k = 0.5$ the intersection is completely ambiguous, and if $k = 1.0$ it is completely well defined. We exclude $k < 0.5$ because such values would imply that our ordering of the features (the direction of the edge in the GSN) was incorrect, and instead we always choose to order the pair of features such that their more likely relationship is described.

The weight of a path within the GSN relating two features which consists

of more than one such uncertain relationship ought to be the product of the confidences, which we are treating as probabilities. For example if $k(n_1, n_2) = 0.9$ and $k(n_2, n_3) = 0.8$ and $k(n_3, n_4) = 0.7$ then the probability that we can correctly infer that n_1 formed before n_4 is $0.9 \times 0.8 \times 0.7 = 0.504$. However, algorithms which operate on weighted graphs generally assume that the length of a path made up of multiple edges is the sum of the weights of the individual edges, and that when calculating an optimal path, a shorter path is preferable, so we must transform our confidence values before assigning edge weights $w_{i,j}$ based on them. The appropriate transformation to convert between products and sums is the logarithm:

$$w_{i,j} = -\log(k(n_i, n_j)) \quad (4.3)$$

and we can then define a function $K(n_a, n_b)$ which defines the confidence we have in the stratigraphic relationship between features represented in the GSN by nodes n_a and n_b if n_b is reachable from n_a . To do this, we use Dijkstra's algorithm [Dijkstra, 1959] to find the shortest path from n_a to n_b in the GSN, i.e. the set of directed edges leading from n_a to n_b having the least sum, $W_{a,b}$. To convert that sum from a weight back into a confidence, we simply invert the transformation above:

$$K(n_a, n_b) = \exp(-W_{a,b}) \quad (4.4)$$

and calculate this value for all pairs of nodes in the GSN which are reachable from one another.

One could also construct a more complex metric, taking into account all the paths between reachable nodes shorter than some threshold value, instead of only the shortest path. We might then allow any stratigraphic relationships which are consistently corroborated in multiple ways to carry more weight in the analysis. However, this possible refinement is not explored further in this work.

With this more continuous notion of reachability and the implied stratigraphic relationships, the calculation of a GSN's completeness and its agreement with a hypothesized ordering will change somewhat, but before addressing that we must consider another kind of ambiguity: the potential existence of cycles within the GSN.

4.2.4.2 Cyclical GSNs

If we relax the assumptions we made when discussing ideal GSNs, then we must admit the possibility that the directed graphs representing them will no longer be acyclic. This means we may encounter sets of logically inconsistent stratigraphic relationships, or equivalently that the binary relation describing the connectivity of the graph is no longer transitive. For example, if two features represented by the nodes n_1 and n_2 have an intersection, with $k(n_1, n_2) = 0.5$, that's the same as saying $k(n_2, n_1) = 0.5$, and the GSN can only be logically consistent if either both or neither edge is included. If both are included then you have a loop between them, and their stratigraphic relationship is encoded, accurately, as being completely ambiguous. This difficulty is easy to avoid by not including such uninformative intersections in the GSN, but if a significant number of the mapped stratigraphic relationships are of low confidence, it's likely that some of them will have been categorized incorrectly, resulting in longer cycles within the graph. We can raise the threshold confidence until no cycles remain, but that potentially discards a significant amount of real information. If only 5% of the intersections with $k = 0.6$ are incorrect, is it better to throw them all out, or to deal with the ambiguity that's been introduced? Of course, it's also possible that genuine cycles exist due to re-activation, or non-instantaneous activity, and it would be interesting to identify them and inspect the features involved to try and understand what, if anything, distinguishes them from the other features not

involved in cycles.

If we calculate the confidences of the shortest paths between all pairs of nodes in the GSN and find that both $K(a, b)$ and $K(b, a)$ are defined, then their stratigraphic relationship is more ambiguous than if a path only existed in one direction between a and b , but it may not be completely ambiguous. If $K(a, b) = 1.0$ and $K(b, a) = 0.3$ then it would seem more likely that a formed before b than vice versa. We can let our *net confidence* in the stratigraphic relationship between a and b be:

$$K_{net}(a, b) = |K(a, b) - K(b, a)| \quad (4.5)$$

Additionally, if both $K(a, b)$ and $K(b, a)$ are defined, then we know there exists a cycle involving all the nodes in the shortest paths connecting a and b .

In general, if there are cycles in the graph there will many of them, but not all of them are equally interesting. The higher the confidence of the cycle, and the fewer edges it involves, the more likely it is to be significant and the easier it will be to inspect. By concentrating only on those cycles which are composed of shortest paths, we narrow our investigation dramatically, and make the task of enumerating the cycles much easier. Additionally, if we find there are no cycles composed of shortest paths with a specified minimum confidence K_{min} , then we know there are no cycles at all having that minimum confidence. It is also desirable to ensure that the uncertainty is not concentrated on one side of the cycle. For instance, the set of all shortest path cycles having $K_{min} > 0.5$ might include a circuit made of three nodes (a, b, c) , with $K(a, b) = 1.0$, $K(b, c) = 1.0$, and $K(c, a) = 0.5$. This cycle meets our criteria, but includes an intersection which is not informational. We can avoid this kind of situation, by requiring that both the forward and reverse paths have a minimum confidence of $\sqrt{K_{min}}$.

To further reduce the number of cycles enumerated, without losing any

useful information, we can also make sure that we only report a single cycle from any *isomorphic group*, that is, any set of cycles in which each contains the same set of nodes and edges, but with different specified source and target nodes (a, b).

In a GSN which is initially a DAG and which also contains many long paths and many different possible routes between pairs of nodes, as do the GSNs representing realistic maps, the reversal of a single high confidence intersection generally results in a large number of high confidence cycles being created. This is equivalent to what would be expected from a localized episode of lineament reactivation or the simultaneous activity of two intersecting features. Large numbers of cycles may also be created if there are many ambiguous intersections, and some of them have been categorized incorrectly, but the cycles in those cases will have much lower confidences, most will be easily screened out using even a modest value of K_{min} .

The presence of many high confidence shortest path cycles in the GSN is thus interesting in its own right, because it indicates the existence of, and highlights the potential locations of interesting geologic activity. It would also indicate that the assumptions underlying the use of GSNs to infer stratigraphic relationships are being violated. However, so long as there are a significant number of pairs of features for which K_{net} is close to unity, the technique should still be fruitful.

4.2.4.3 Completeness, agreement, and significance in ambiguous GSNs

We can now refine our definitions of an ambiguous or continuous GSN's completeness, its agreement with a stated ordering hypothesis, and the significance of that agreement in the light of the previous section. Given a GSN containing the set of features X , implying the reachability relation $R(X)$, the completeness

becomes:

$$C \equiv \frac{\sum_{(x,y) \in R(X)} K_{net}(x, y)}{|X|(|X| - 1)/2} \quad (4.6)$$

and the agreement with a hypothesized ordering $P(X)$ becomes:

$$A(P, R, X) \equiv \frac{\sum_{(x,y) \in P(X) \cap R(X)} K_{net}(x, y)}{\sum_{(x,y) \in P(X) \cap R(X)} K_{net}(x, y) + \sum_{(x,y) \in P(X) \cap \bar{R}(X)} K_{net}(x, y)} \quad (4.7)$$

and the definition of significance remains the same, but uses this continuous definition of agreement.

4.3 Mapping E15

We can now apply the above analytical methods to set of features on Europa. To increase the chances of obtaining a significant result it makes sense to focus on a region with a high lineament density, and choosing an area with high resolution imaging coverage will increase the confidence of the mapped intersections. The southern portion of the E15 regional mapping swath from the Galileo mission, seen in Fig. 4.3, satisfies both of these criteria. The images were transformed to a Mercator projection, and a georeferenced mosaic was created for mapping using the qGIS software package.

First, a total of 168 linear features were mapped, of which 164 were members of a connected network having a cumulative length of 29,000 km. The location of all of the 729 intersections between these features was calculated, and each of the intersections was inspected individually and assigned one of six confidence values $0.5 \leq k \leq 1.0$, in discrete intervals of 0.1, based on how apparent the superposition relationship was. The unique id of the top and bottom lineament at the intersection was also noted.

The mapped lineaments are shown in Fig. 4.6 and the distribution of intersection confidences is shown in Fig. 4.7.

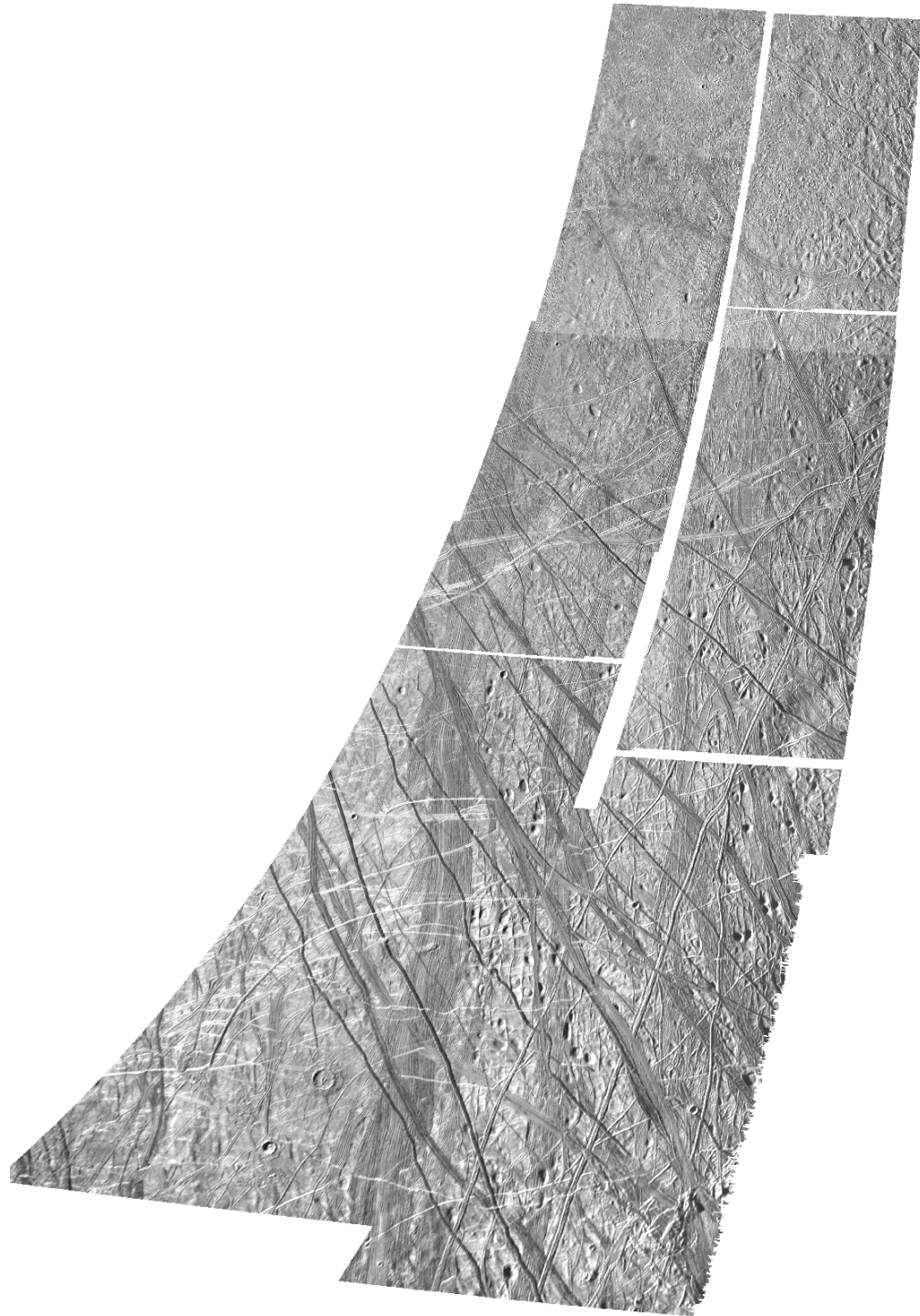


Figure 4.3: The southern portion of the E15 regional mapping mosaic. The average resolution of the mosaic is ~ 200 m/px, and the region is densely lineated, making it a good candidate for analysis using GSNs. See Figs. 4.4 and 4.5 for closeups of several intersections, displaying the entire spectrum of confidence values.

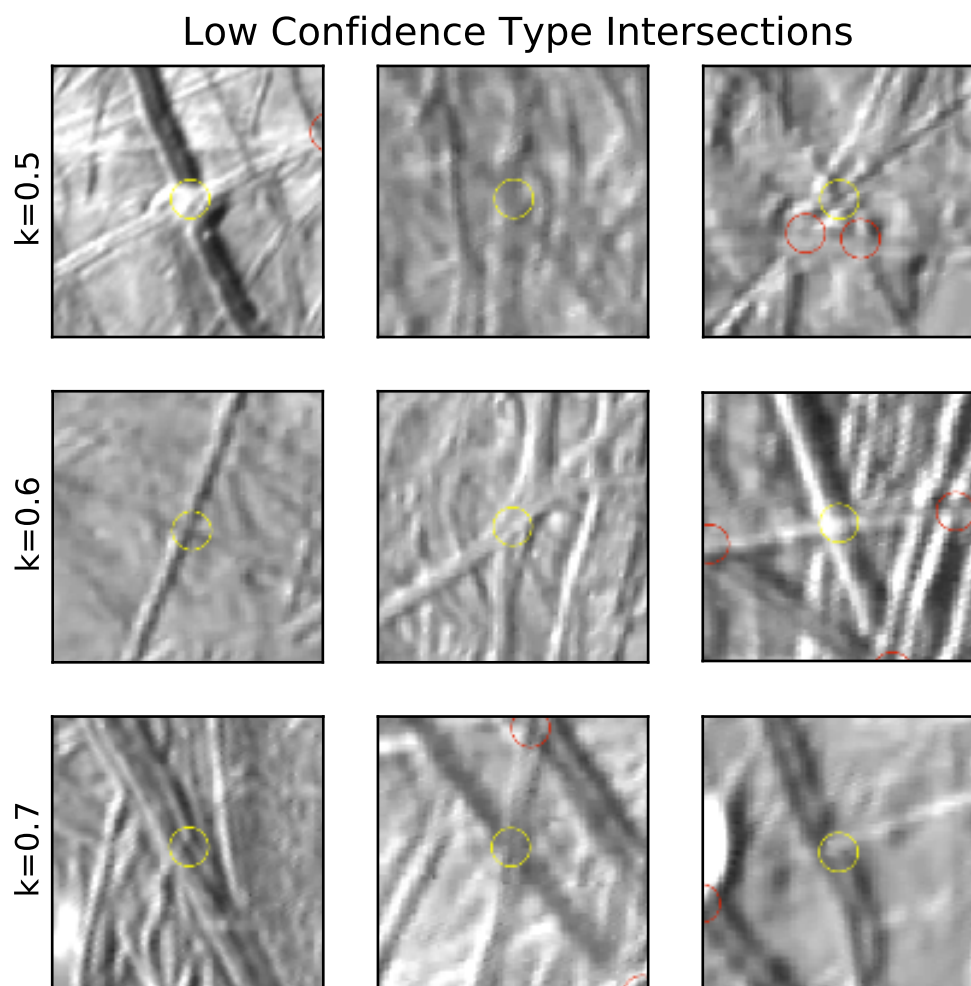


Figure 4.4: Three examples of intersections for each of $k = (0.5, 0.6, 0.7)$. The intersection in question is highlighted with a yellow circle. Low confidence intersections are generally the result of disrupted terrain, low resolution, similar albedo features intersecting one another.

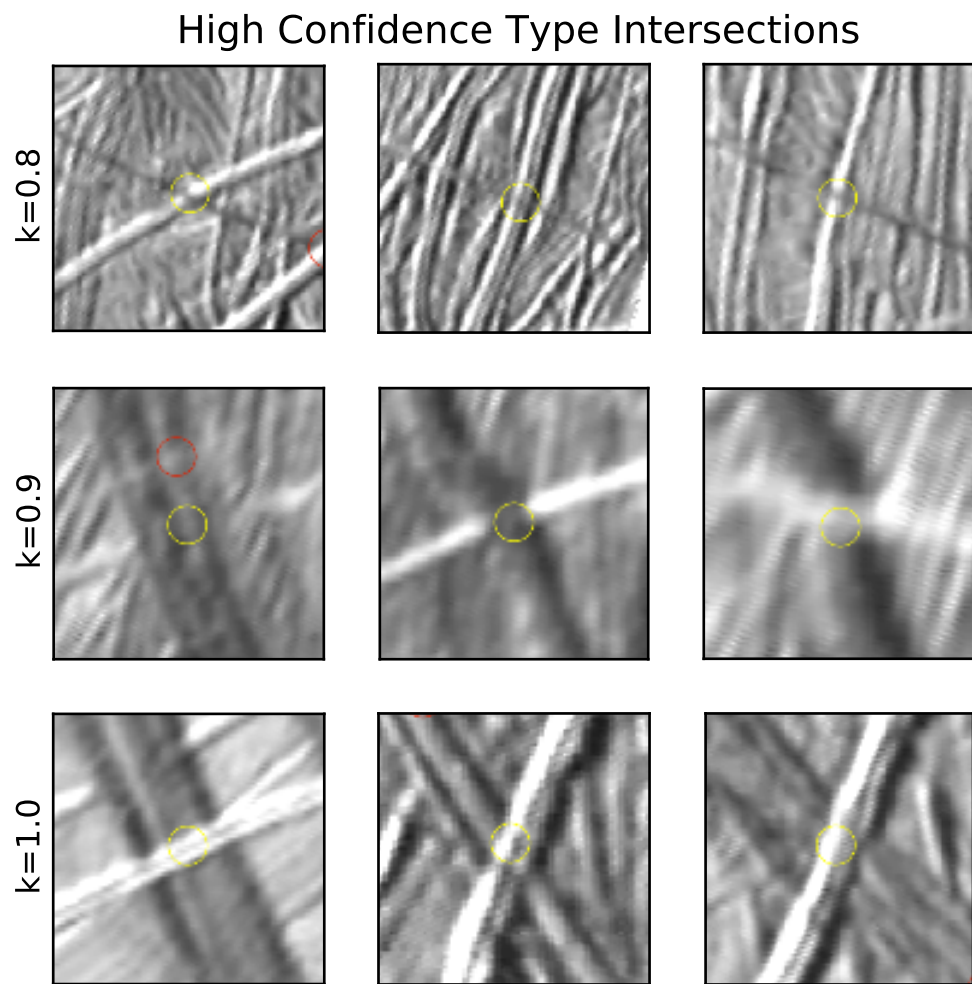


Figure 4.5: Three examples of intersections for each of $k = (0.8, 0.9, 1.0)$. The intersection in question is highlighted with a yellow circle. High confidence features usually have significant width, or multiple apparent structures all disappearing and re-appearing together.

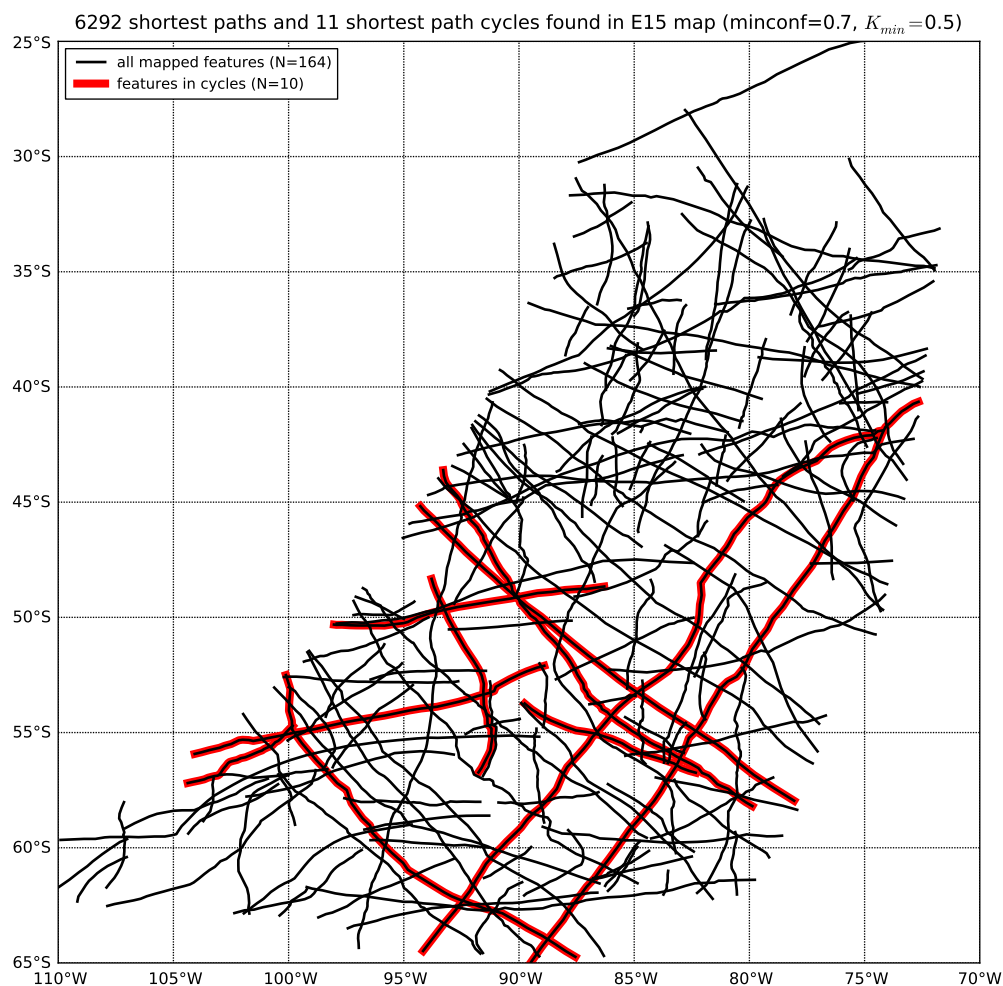


Figure 4.6: The lineaments mapped from the imaging mosaic in Fig. 4.3, Lineaments highlighted in red participate in at least one shortest path cycle with a path confidence $K_{\min} \geq 0.5$ when intersections having $k \geq 0.7$ are included. Even when no constraint is placed on K_{\min} the GSN remains highly acyclic, with 16 features participating in a total of 56 cycles. Thus our assumption that features in general have a well defined, unique period of activity appear to be justified.

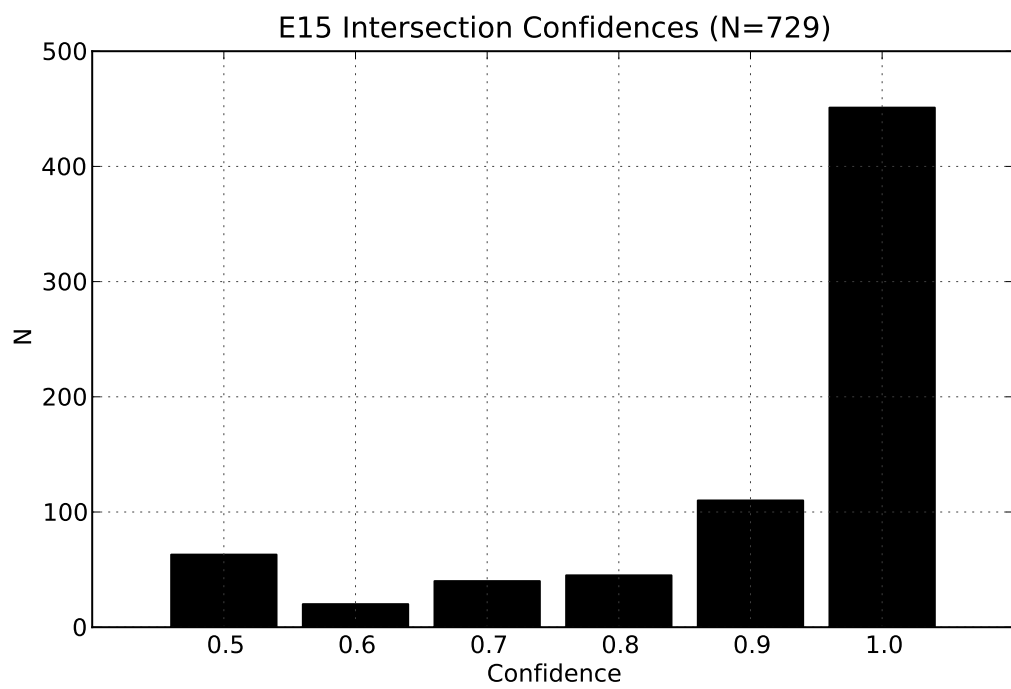


Figure 4.7: A large majority of the mapped superposition relationships are fairly unambiguous.

4.4 Results: Does the E15 GSN corroborate NSR?

Even with the relatively high resolution imaging and high lineament density in the E15 region, the GSN derived from the map is far from being complete. The relationship between the minimum allowable intersection confidence and both the GSN's completeness and the total number of ordering relationships defined to any degree, $|R(X)|$, is shown in Fig. 4.2. The overall distribution of path confidences is shown in Fig. 4.8. Unsurprisingly, much of the GSN's connectivity comes from the completely ambiguous $k = 0.5$ edges. For consistency, those edges are added in both directions between the features they relate, since neither one nor the other ordering has been deemed more probable. This results in a vast number of cycles within the graph.

Once those lowest confidence edges are removed, the GSN becomes much closer to being acyclic. The relationships between the number of shortest path cycles in the graph, the lowest confidence edges included, and the minimum required path confidence K_{min} for the entire cycle are can be seen in Fig. 4.9, which shows that there are at least a few cycles that persist even with fairly strict confidence requirements. If we require $K_{min} > 0.5$, only 10 features participate in a total of 11 shortest path cycles. Those features are highlighted in Fig. 4.6. Removing any constraint on K_{min} , but requiring that all intersections in the GSN have $k \geq 0.7$ only increases the total number of shortest path cycles to 56, and the number of features participating in them to 16, which is remarkably close to being acyclic, considering that under those same criteria we find that the GSN has a completeness $C = 0.213$ and $|R(X)| = 6,292$ (out of $(164 \times 163)/2 = 13,336$ possible), i.e. fewer than 1% of the shortest paths in the GSN result in apparently inconsistent cyclic stratigraphic relationships. This is heartening, because it suggests that our initial assumptions about lineament activity are generally justified. The features

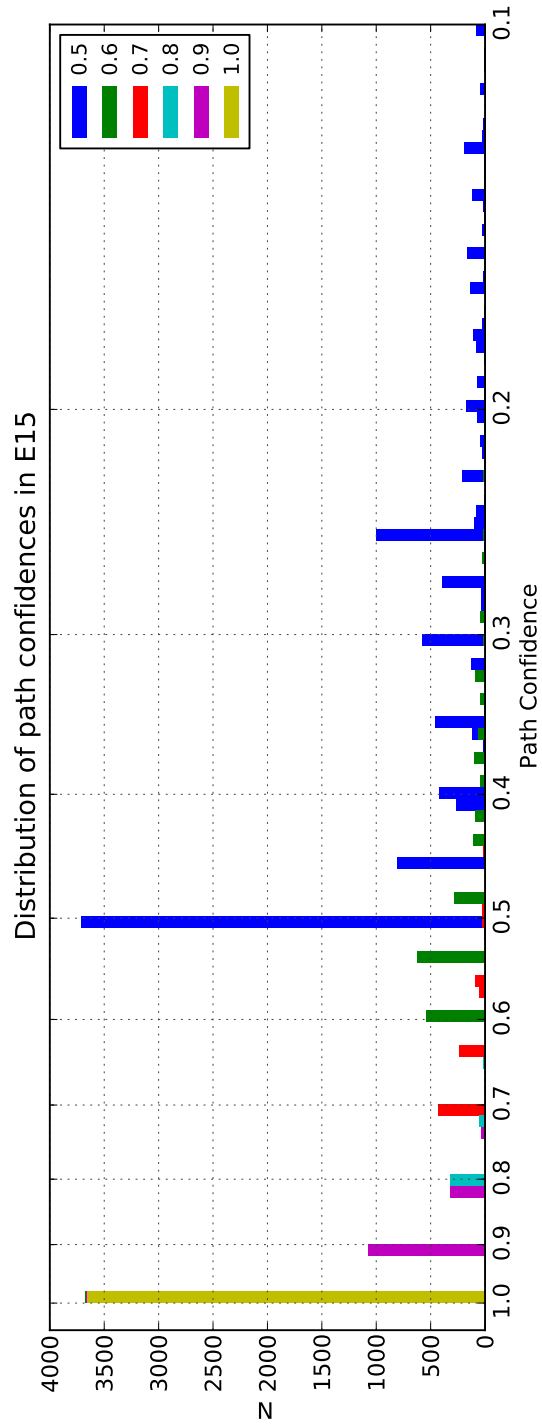


Figure 4.8: As the minimum required intersection confidence is reduced, more and more low confidence paths appear in the GSN. Histogram is color coded by the minimum intersection confidence which must be included for a particular path confidence to be present. Because there are only 6 possible intersection confidences, the distribution of path confidences is highly quantized. Note that the x-axis (and the bin widths) are logarithmic.

and intersections involved in the few high confidence cycles warrant further investigation, but for the present work, we will be content to proceed knowing that in general, the stratigraphic relationships between features are well defined, and we can thus hope to use the GSN to either corroborate or contradict another independent ordering hypothesis.

The non-uniform apparent history of lineament formation activity as a function of shell rotation that we found in Chapter 3 suggests that less than half a shell rotation is clearly recorded by the lineaments, if they are the result of tensile fracture due to the NSR stress field. If we again use the amount of shell rotation required to align a mapped feature with the expected orientation of failure in the NSR field as a proxy for time, and apply it to the features mapped in the E15 region, we can generate an ordering hypothesis to compare against the GSN. The apparent NSR activity history for the E15 map is shown in Fig. 4.10. It resembles the global activity history shown in Fig. 3.14 and 3.13, though neither the peak at $b \approx 30^\circ$ nor the subsequent trough at $b \approx 75^\circ$ appear as statistically significant. However, this may be partly the result of greater dispersion in the $H(b)$ curves for the longitudinally randomized set of features, which is significantly smaller in this case than for the global lineament map.

Similar work attempting to infer a history and quantity of NSR based on cross cutting relationships has been done by e.g. [Sarid *et al.*, 2004]. That work made the explicit assumption that every observed intersection had to be respected, discounting the possibility that the orientation of some features might be significantly perturbed by sources of stress other than NSR, and also setting aside the possibility of re-activation. Their result was that multiple full shell rotations were required to explain the observed superposition relationships, and that either faster or slower than synchronous shell rotation were roughly equally plausible.

We are approaching the topic from what one might call the other side,

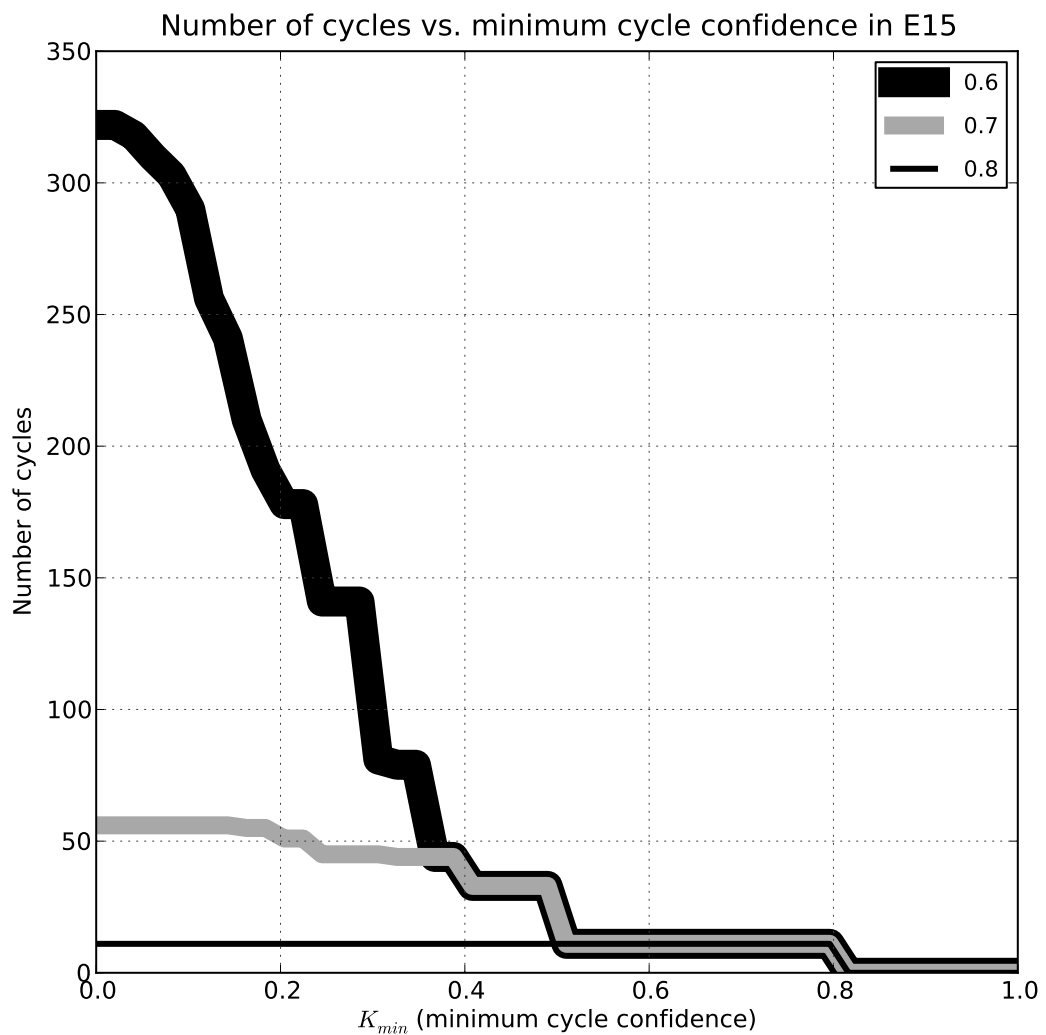


Figure 4.9: As K_{min} , the minimum acceptable cycle confidence is raised, the number of cycles in the GSN drops dramatically, until only a few in a single small geographic cluster remains. For a given K_{min} , the lower the minimum intersection confidence, the more cycles may be included. The curves converge because at large values of K_{min} , the requirement that the confidence of both the paths to and from the target node in the cycle exceed $\sqrt{K_{min}}$ becomes more stringent than the minimum allowed intersection confidence.

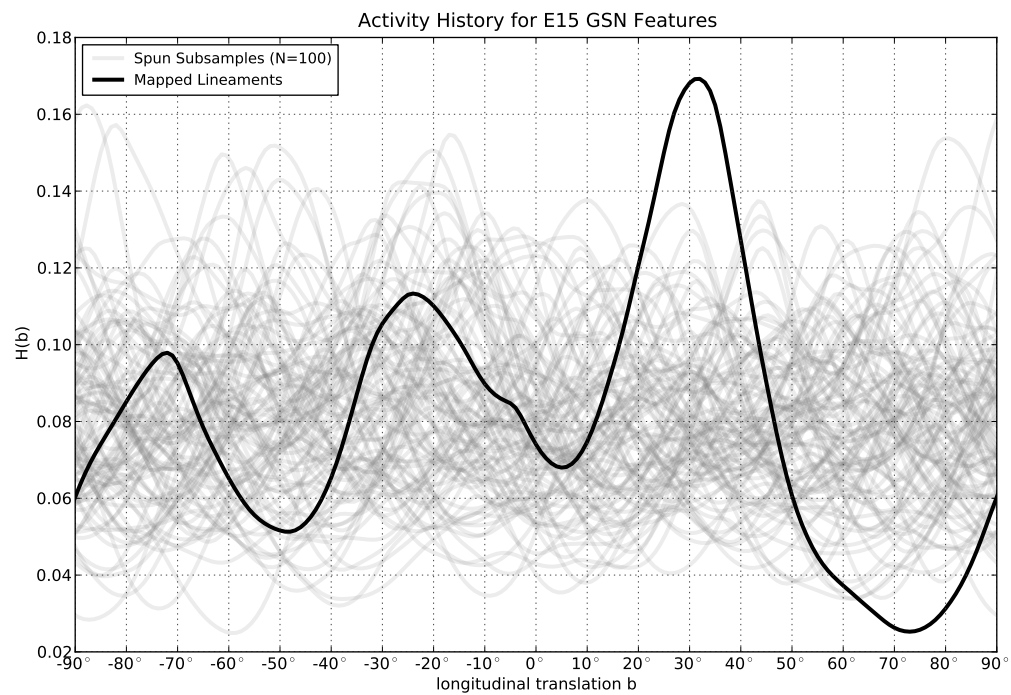


Figure 4.10: The lineaments mapped in the E15 region have an apparent NSR activity history similar to (though somewhat less significant than) that of the global lineaments discussed in Ch. 3, despite having been mapped at much higher resolution. Compare Fig. 3.13.

based on the results in Ch. 3, and instead asking what fraction of the temporal relationships implied by the observed intersections are respected if we assume that less than 180° of shell rotation has taken place, and is that proportion greater than would be expected by chance? Additionally, if we obtain a significant result it will only be able to argue for one of the two directions of shell rotation, as reversing the hypothesized ordering would reverse all of the implied temporal relationships within it. If the agreement A is a function of the map and the ordering, and we denote prograde rotation as NSR^+ and retrograde rotation as NSR^- , then if we find $A(E15, NSR^+) = p$ we will also obtain $A(E15, NSR^-) = (1 - p)$

The results of the comparison can be seen in 4.11. The thick black vertical line is the actual agreement, $A(E15, NSR^+) = 0.707$, and is more than 5σ away from the mean of the randomized distribution. This argues very strongly against both the null hypothesis of a random order of formation and the possibility of retrograde rotation, if we attribute the lineaments to NSR stresses. Suggestively, this is roughly the level of agreement we would expect to see if the map were made up of a mix of 40% NSR features, and 60% random, uniformly distributed features – the proportions which we found in attempting to reconstruct the peak in the $H(b)$ curve from the global map. This is because we would expect all the intersections between features in the 40% of the map which makes up the peak to respect the NSR ordering constraints, as well as roughly half of the intersections between the 60% (an additional 30%) of the mapped features that are random, and anything else in the map.

It is somewhat less clear whether this result strongly argues *for* the NSR hypothesis. As in the previous chapter, there is a basic problem with NSR, which is that while it does make predictions about what we should observe, those predictions are very simple, and it is not too difficult to imagine that other processes which we have not considered in detail might be equally or more consistent with

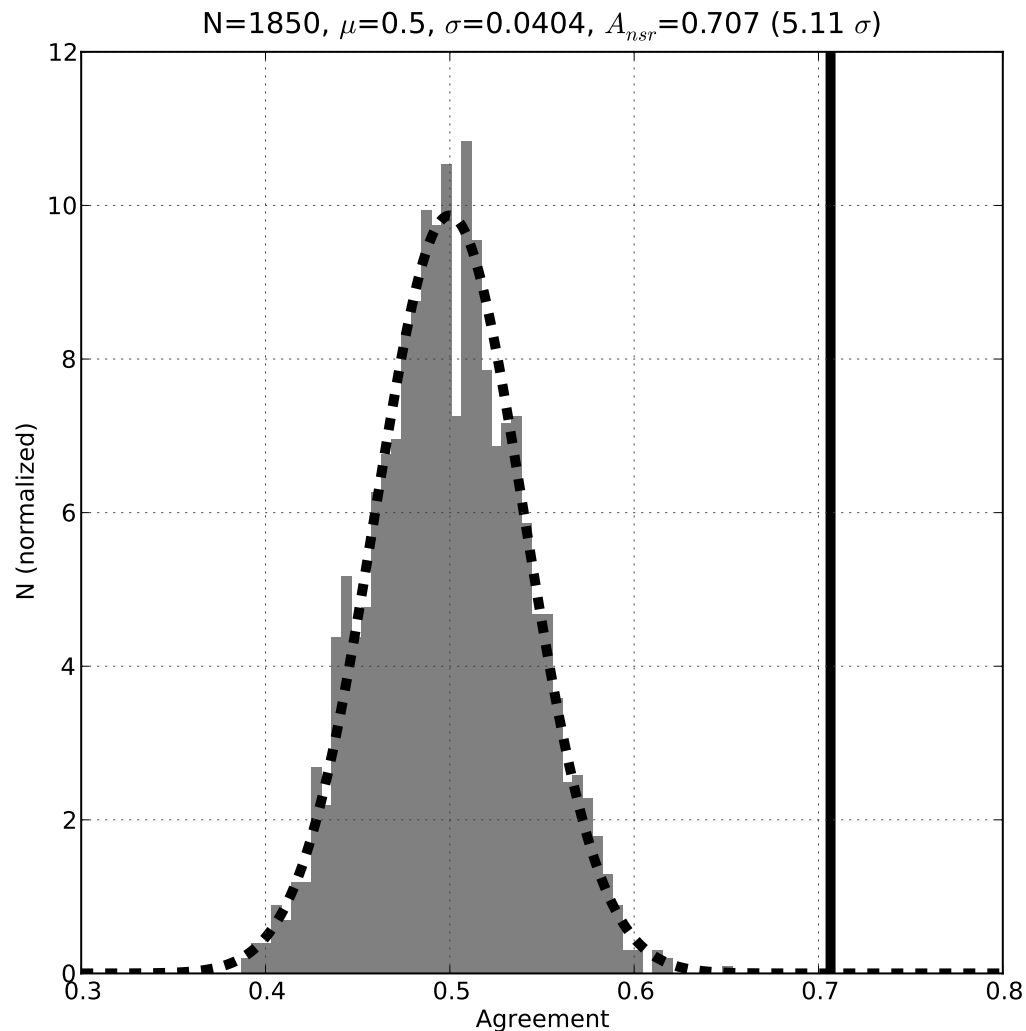


Figure 4.11: Histogram showing the range of expected chance agreement values for the features from the E15 regional map and the NSR ordering hypothesis. The distribution appears truly Gaussian, having a mean, $\mu = 0.500$ and standard deviation $\sigma = 0.0404$ (the thick dashed line is an ideal normal probability distribution generated using those parameters). The measured agreement between the E15 map and the NSR hypothesis is 0.707 (the thick vertical line), which is $\sim 5\sigma$ from the mean, indicating that the NSR ordering is much more consistent with the stratigraphy than chance can explain.

the observations.

That said, the strong preference demonstrated here for a particular direction of shell rotation (even when only considering 180° of rotation overall), when combined with the very significant non-uniformity in the inferred history of activity, does seem to lend significant support to the NSR hypothesis. Testing the NSR ordering hypothesis within several widely separated regions on the surface and obtaining the same result would be very strong evidence in support of NSR, as it would be more likely to exclude other possibilities, such as TPW. If NSR is really responsible for the features we see, it should do well everywhere. If it does not do well everywhere, we might attempt to use it as a criterion for narrowing down the apparently broad range of potentially statistically equivalent paleopole locations seen in Fig. 3.20, and see if any clearly superior pole exists.

4.5 Future GSN Applications

There are many possible future applications for encoding superposition relationships using the GSN model. Obviously there are other regions on Europa with high resolution imaging, and some fraction of the intersections between the global-scale features analyzed in Chapter 3 are also clear enough to make the technique fruitful. When we eventually obtain high resolution coverage of Europa's entire surface, we may be able to create a detailed global-scale GSN, relating features temporally that are separated by thousands of km.

Europa's profusion of linear features makes it the ideal body for the technique, but there is nothing precluding the construction of GSNs made up of polygonal features, or a mixture of different feature types. All that is required is for the features to have well defined extents, clear superposition relationships, and fairly discrete periods of activity.

Clearly there are also many other ordering hypotheses that could be tested,

based on visible feature characteristics like morphology or spectral properties, or as with the comparison above, based on some time dependent model of formation. Of course it would also be more interesting to compare two competing hypotheses, rather than just the null hypothesis.

There are other metrics which can be further developed to take advantage of the GSN encoding as well. For instance, the completeness of the GSN will be expected to be different for different formation processes: a regular rectilinear grid with a random order of feature formation tends to be almost complete no matter how big it is, while NSR, in the ideal case, would tend to create many sub-parallel lineaments having few intersections, until a significant amount of shell rotation (and thus also rotation of the expected failure orientation) had taken place. The quantity being measured here then more generally would be the rate of feature formation vs. the change in failure orientation. More detailed control studies, including the effects of feature length distribution, would need to be completed to discern these differences. This might allow us to more confidently differentiate between shear and tensile failure, as in compressional failure, one would expect to see multiple faulting orientations simultaneously, resulting in more intersections than in a failure mode like NSR and tensile fracture.

The cluster of features found to be involved in cycles should be picked apart in detail. Is there a small subset of them which if removed can eliminate the cycles altogether? If so is there anything special about those features? Do they have particularly questionable continuity? If we map other regions on Europa do they result in similarly almost-acyclic GSNs? If not, what other variables correlate well with a presence or lack of cycles?

Chapter 5

Conclusions and Future Work

We know that the two sources of tidal stress which we have modeled are insufficient, alone to explain the diversity of features that we see on Europa. Other forces must be at work. The method described in Chapter 2, and the code implementing it (available at <http://code.google.com/p/satstress/> under an open source license) are amenable to the addition of other stresses, and ideally others will extend the model to include stresses due to obliquity, true polar wander, and other potential drivers of global tectonics.

We come away from this investigation having somewhat less confidence in the NSR hypothesis than we began with. The originally cited evidence for it, that the prominent lineaments were a particularly good fit to the expected stresses, turns out to be unconvincing upon closer inspection. However, there are other more subtle lines of evidence, such as the non-uniformity of the activity history, and the preponderance toward agreement with the NSR ordering that we find in mapped superposition relationships. Our brains want to find patterns, and to tell stories about those patterns, but simply having a narrative which is consistent with the available observations is not enough to indicate causation. We must also investigate whether that consistency is remarkable; if we are telling a story which will always, or usually, be true, regardless of our observations, then we might as well be reading somebody's palm as mapping out the tectonics of a distant, icy

world.

If based on the evidence presented here, we are willing to accept that NSR has occurred, and is responsible for a significant portion of the tectonic features we see, then we can draw some conclusions. When examined in combination with the stratigraphic information from Chapter 4 it seems likely that the shell is rotating faster than synchronously, and that the rate of lineament formation is low, compared to the rate of shell rotation. It appears that in order to get the width and amplitude of peak we see in $H(b)$, lineaments must have been forming over a significant span of rotational time: a single, completely discrete event cannot reproduce our observations. For some reason, this span of time appears to have been recent, and short, relative to the shell's rotation period.

The location of the peak in activity, if the shell has not rotated very much, indicates that the ice is responding at least somewhat, if not entirely viscously on the timescale of the shell's rotation. This places an upper bound of ~ 1.75 MPa on the magnitude of the tensile stresses due to NSR.

The story with respect to a true polar wander event is still murky. Without doing much more rigorous (and computationally intensive) statistics on the fits, we cannot say for certain whether the variation in apparent lineament formation history with paleopole location is significant. If there really is a pole about which NSR occurred, then we should expect to see that information reflected also in the agreement between stratigraphic information and the ordering implied by NSR about those paleopoles, and we should expect it to be consistent globally. Performing the analysis described in Chapter 4 for three widely distributed sites on Europa, and getting the same answer for all of them, would be strong evidence of NSR, and potentially for TPW as well, if the best pole were not the current one.

The fact that both our synthetic reconstructions of the activity history for

the global map and the agreement between the NSR ordering and the mapped stratigraphy suggest roughly 40% of the mapped features are due to recently formed NSR features is tantalizing. If the stratigraphically agreeing features also have best-fit b values which cluster around the peak, then we might be able to identify with some accuracy which features are actually due to NSR, and which are just background noise.

Neither the fitting of mapped lineaments to the NSR stresses, nor the geological superposition networks alone can provide very clear answers. Both of them are handicapped by a fundamental lack of data, but because they access different information, together they appear capable of giving us a much more complete picture of Europa's tectonic history.

Bibliography

- Alexander, E. C., Jr., P. K. Davis, and R. S. Lewis, Argon-40-Argon-39 Dating of Apollo Sample 15555, *Science*, 175, 417–419, doi:10.1126/science.175.4020.417, 1972.
- Bart, G. D., E. P. Turtle, W. L. Jaeger, L. P. Keszthelyi, and R. Greenberg, Ridges and tidal stress on Io, *Icarus*, 169, 111–126, doi:10.1016/j.icarus.2004.01.003, 2004.
- Bierhaus, E. B., C. R. Chapman, and W. J. Merline, Secondary craters on Europa and implications for cratered surfaces, *Nature*, 437, 1125–1127, doi:10.1038/nature04069, 2005.
- Bills, B. G., Free and forced obliquities of the Galilean satellites of Jupiter, *Icarus*, 175, 233–247, doi:doi:10.1016/j.icarus.2004.10.028, 2005.
- Collins, G. C., J. W. Head, and R. T. Pappalardo, Formation of Ganymede grooved terrain by sequential extensional episodes: implications of Galileo observations for regional stratigraphy, *Icarus*, 135, 345–359, doi:10.1006/icar.1998.5978, 1998.
- Croft, S. K., and L. A. Soderblom, Geology of the Uranian satellites, in *Uranus*, pp. 561–628, University of Arizona Press, Tucson, AZ, 1991.
- Croft, S. K., J. S. Kargel, J. M. Moore, P. M. Schenk, and R. G. Strom, Geology of Triton, in *Neptune and Triton*, pp. 879–948, University of Arizona Press, Tucson, AZ, 1995.
- Dahlen, F., The passive influence of the oceans upon the rotation of the earth, *Geophys. J.R. Astr. Soc.*, 46, 363–406, 1976.
- Dahlen, F. A., and J. Tromp, *Theoretical Global Seismology*, Princeton University Press, Princeton, New Jersey, 2001.
- Dalrymple, G. B., *The Age of the Earth*, Stanford University Press, 1994.
- Dijkstra, E. W., A note on two problems in connexion with graphs, *Numerische Mathematik*, 1, 269–271, 1959.

- Dobrovolskis, A. R., Internal stresses in Phobos and other triaxial bodies, *Icarus*, 52, 136–148, doi:10.1016/0019-1035(82)90174-9, 1982.
- Dombard, A. J., and W. B. McKinnon, Folding of Europa's icy lithosphere: an analysis of viscous-plastic buckling and subsequent topographic relaxation, *Journal of Structural Geology*, 28, 2259–2269, doi:10.1016/j.jsg.2005.12.003, 2006.
- Figueredo, P. H., and R. Greeley, Geologic mapping of the northern leading hemisphere of Europa from Galileo solid-state imaging data, *J. Geophys. Res.*, 105, 22,629–22,646, 2000.
- Geissler, P. E., et al., Evidence for non-synchronous rotation of Europa, *Nature*, 391, 368–370, 1998.
- Greeley, R. C., C. Chyba, J. W. Head, T. McCord, W. B. McKinnon, and R. T. Pappalardo, Geology of Europa, in *Jupiter: The Planet, Satellites & Magnetosphere*, pp. 329–362, Cambridge University Press, New York, 2004.
- Greenberg, R., and S. J. Weidenschilling, How fast do Galilean satellites spin?, *Icarus*, 58, 186–196, doi:10.1016/0019-1035(84)90038-1, 1984.
- Greenberg, R., et al., Tectonic processes on Europa: Tidal stresses, mechanical response, and visible features, *Icarus*, 135, 64–78, doi:10.1006/icar.1998.5986, 1998.
- Harada, Y., and K. Kurita, Effect of non-synchronous rotation on surface stress upon Europa: Constraints on surface rheology, *Geophys. Res. Lett.*, 34, L11,204, doi:10.1029/2007GL029554, 2007.
- Hartmann, W. K., Early lunar cratering, *Icarus*, 5, 406–418, doi:10.1016/0019-1035(66)90054-6, 1966a.
- Hartmann, W. K., Martian Cratering, *Icarus*, 5, 565–576, doi:10.1016/0019-1035(66)90071-6, 1966b.
- Hartmann, W. K., Note: Lunar Cratering Chronology, *Icarus*, 13, 299–+, doi:10.1016/0019-1035(70)90059-X, 1970.
- Helfenstein, P., and E. M. Parmentier, Patterns of fracture and tidal stresses on Europa, *Icarus*, 53, 415–430, doi:10.1016/0019-1035(83)90206-3, 1983.
- Helfenstein, P., and E. M. Parmentier, Patterns of fracture and tidal stresses due to nonsynchronous rotation - Implications for fracturing on Europa, *Icarus*, 61, 175–184, doi:10.1016/0019-1035(85)90099-5, 1985.
- Hoppa, G. V., Europa: effects of rotation and tides on tectonic processes, *Doctoral Thesis*, p. 227, 1998.

- Hoppa, G. V., R. Greenberg, P. Geissler, B. R. Tufts, J. Plassmann, and D. D. Durda, Rotation of Europa: Constraints from terminator and limb positions, *Icarus*, 137, 341–347, doi:10.1006/icar.1998.6065, 1999a.
- Hoppa, G. V., B. R. Tufts, R. Greenberg, and P. Geissler, Strike-Slip faults on Europa: Global shear patterns driven by tidal stress, *Icarus*, 141, 287–298, doi:10.1006/icar.1999.6185, 1999b.
- Hoppa, G. V., B. R. Tufts, R. Greenberg, and P. E. Geissler, Formation of cycloidal features on Europa, *Science*, 285, 1899–1902, 1999c.
- Hoppa, G. V., B. Randall Tufts, R. Greenberg, T. A. Hurford, D. P. O'Brien, and P. E. Geissler, Europa's rate of rotation derived from the tectonic sequence in the Astypalaea region, *Icarus*, 153, 208–213, doi:10.1006/icar.2001.6663, 2001.
- Hurford, T. A., B. G. Bills, A. R. Sarid, and R. Greenberg, Unraveling Europa's Tectonic History: Evidence for a Finite Obliquity?, in *37th Annual Lunar and Planetary Science Conference, Lunar and Planetary Institute Conference Abstracts*, vol. 37, edited by S. Mackwell and E. Stansbery, pp. 1303–+, 2006.
- Hurford, T. A., A. R. Sarid, and R. Greenberg, Cycloidal cracks on Europa: Improved modeling and non-synchronous rotation implications, *Icarus*, 186, 218–233, doi:10.1016/j.icarus.2006.08.026, 2007.
- Husain, L., O. A. Schaeffer, and J. F. Sutter, Age of a Lunar Anorthosite, *Science*, 175, 428–430, doi:10.1126/science.175.4020.428, 1972.
- Kattenhorn, S. A., Nonsynchronous rotation evidence and fracture history in the bright plains region, Europa, *Icarus*, 157, 490–506, doi:10.1006/icar.2002.6825, 2002.
- Kaula, W. M., Tidal dissipation by solid friction and the resulting orbital evolution, *Rev. of Geophys.*, 2, 661–685, 1964.
- King, G. C. P., R. S. Stein, and J. Lin, Static stress changes and the triggering of earthquakes, *Bulletin of the Seismological Society of America*, 84, 935–953, 1994.
- Knopf, A., and A. Holmes, The Age of the Earth, *Bulletin of the National Research Council*, 80, 1931.
- Lambeck, K., *The Earth's Variable Rotation: Geophysical Causes and Consequences*, Cambridge University Press, Cambridge, England, 1980.
- Leith, A. C., and W. B. McKinnon, Is there evidence for polar wander on Europa?, *Icarus*, 120, 387–398, doi:10.1006/icar.1996.0058, 1996.
- McEwen, A. S., Tidal reorientation and the fracturing of Jupiter's moon Europa, *Nature*, 321, 49–51, 1986.

- McEwen, A. S., L. P. Keszthelyi, R. Lopes, P. M. Schenk, and J. R. Spencer, The lithosphere and surface of Io, in *Jupiter: The Planet, Satellites & Magnetosphere*, pp. 307–328, Cambridge University Press, New York, 2004.
- Melosh, H. J., Large impact craters and the moon's orientation, *Earth Planet. Sci. Lett.*, 26, 353–360, 1975.
- Melosh, H. J., Global tectonics of a despun planet, *Icarus*, 31, 221–243, 1977.
- Melosh, H. J., Tectonic patterns on a tidally distorted planet, *Icarus*, 43, 334–337, doi:10.1016/0019-1035(80)90178-5, 1980a.
- Melosh, H. J., Tectonic patterns on a reoriented planet - Mars, *Icarus*, 44, 745–751, doi:10.1016/0019-1035(80)90141-4, 1980b.
- Meyer, J., and J. Wisdom, Tidal heating in Enceladus, *Icarus*, 188, 535–539, doi:10.1016/j.icarus.2007.03.001, 2007.
- Moore, W. B., and G. Schubert, The tidal response of Europa, *Icarus*, 147, 317–319, 2000.
- Munk, W., and G. MacDonald, *The Rotation of the Earth*, Cambridge University Press, Cambridge, England, 1975.
- Nimmo, F., and R. T. Pappalardo, Furrow flexure and ancient heat flux on Ganymede, *Geophys. Res. Lett.*, 31, L19701, doi:10.1029/2004GL020763, 2004.
- Nimmo, F., and R. T. Pappalardo, Diapir-induced reorientation of Saturn's moon Enceladus, *Nature*, 441, 614–616, 2006.
- Nimmo, F., P. C. Thomas, R. T. Pappalardo, and W. B. Moore, Inferring the state of tidally-heated satellite ice shells from global shape measurements, *Eos Trans. AGU*, 87, 2006.
- Nimmo, F., J. R. Spencer, R. T. Pappalardo, and M. E. Mullen, Shear heating as the origin of the plumes and heat flux on Enceladus, *Nature*, 447, 289–291, 2007.
- Ojakangas, G. W., and D. J. Stevenson, Thermal state of an ice shell on Europa, *Icarus*, 81, 220–241, 1989.
- Pappalardo, R. T., G. C. Collins, J. W. Head, P. Helfenstein, T. McCord, J. M. Moore, L. M. Prockter, P. M. Schenk, and J. R. Spencer, Geology of Ganymede, in *Jupiter: The Planet, Satellites & Magnetosphere*, pp. 363–396, Cambridge University Press, New York, 2004.
- Peale, S. J., Origin and evolution of the natural satellites, *Ann. Rev. of Astron. and Astrophys.*, 37, 533–602, 1999.

- Peltier, W. R., The impulse response of a Maxwell earth, *Rev. of Geophys. and Space Phys.*, 12, 649–669, 1974.
- Peltier, W. R., The LAGEOS constraint on deep mantle viscosity: result from a new normal mode method for the inversion of viscoelastic relaxation spectra., *J. Geophys. Res.*, 90, 9411–9421, 1985.
- Prockter, L. M., R. T. Pappalardo, and F. Nimmo, A shear heating origin for ridges on Triton, *Geophys. Res. Lett.*, 32, L14202, doi:10.1029/2005GL022832, 2005.
- Rappaport, N. J., L. Iess, J. M. Wahr, J. I. Lunine, J. W. Armstrong, S. W. Asmar, P. Tortora, M. Di Benedetto, and P. Racioppa, Can Cassini detect a subsurface ocean in Titan from gravity measurements?, *Icarus*, 2008.
- Sarid, A. R., R. Greenberg, G. V. Hoppa, P. Geissler, and B. Preblich, Crack azimuths on Europa: time sequence in the southern leading face, *Icarus*, 168, 144–157, doi:10.1016/j.icarus.2003.11.021, 2004.
- Schenk, P., H. Hargitai, R. Wilson, A. McEwen, and P. Thomas, The mountains of Io: Global and geological perspectives from Voyager and Galileo, *J. Geophys. Res.*, 106(E15), 33,201–33,222, doi:10.1029/2000JE001408, 2001.
- Schenk, P., I. Matsuyama, and F. Nimmo, True polar wander on Europa from global-scale small-circle depressions, *Nature*, 453, 368–371, doi: 10.1038/nature06911, 2008.
- Schubert, G., J. D. Anderson, T. Spohn, and W. B. McKinnon, *Interior composition, structure and dynamics of the Galilean satellites*, pp. 263–280, Cambridge University Press, New York, NY, 2004.
- Showman, A. P., D. J. Stevenson, and R. Malhotra, Coupled orbital and thermal evolution of Ganymede, *Icarus*, 129, 367–383, 1997.
- Smith-Konter, B., and R. T. Pappalardo, Tidally driven stress accumulation and shear failure of Enceladus's tiger stripes, *Icarus*, pp. ??–??, 2008.
- Spaun, N. A., R. T. Pappalardo, and J. W. Head, Evidence for shear failure in forming near-equatorial lineae on Europa, *J. Geophys. Res.*, 108(E6), 14–1, doi:10.1029/2001JE001499, 2003.
- Squyres, S. W., and S. K. Croft, The tectonics of icy satellites, in *Satellites*, pp. 293–341, University of Arizona Press, Tucson, AZ, 1986.
- Toulmin, S. E., and J. Goodfield, *The Discovery of Time*, 64 pp., University of Chicago Press, Chicago, 1982.

- Wahr, J., Z. A. Selvans, M. E. Mullen, A. C. Barr, G. C. Collins, M. M. Selvans, and R. T. Pappalardo, Modeling stresses on satellites due to nonsynchronous rotation and orbital eccentricity using gravitational potential theory, *Icarus*, 200, 188–206, doi:10.1016/j.icarus.2008.11.002, 2009.
- Wahr, J. M., Body tides on an elliptical, rotating, elastic and oceanless Earth, *Geophys. J.R. Astr. Soc.*, 64, 677–704, 1981.
- Wahr, J. M., M. T. Zuber, D. E. Smith, and J. I. Lunine, Tides on Europa, *J. Geophys. Res.*, 111, E12,005, doi:10.1029/2006JE002,729, 2006.
- Wu, X. P., Y. E. Bar-Sever, W. M. Folkner, J. G. Williams, and J. F. Zumberge, Probing Europa’s hidden ocean from tidal effects on orbital dynamics, *Geophys. Res. Lett.*, 28, 2245–2248, 2001.
- Yoder, C. F., How tidal heating in Io drives the galilean orbital resonance locks, *Nature*, 279, 767–770, 1979.
- Zahnle, K., L. Dones, and H. F. Levison, Cratering rates on the Galilean satellites, *Icarus*, 136, 202–222, 1998.
- Zahnle, K., P. Schenk, H. Levison, and L. Dones, Cratering rates in the outer Solar System, *Icarus*, 163, 263–289, doi:10.1016/S0019-1035(03)00048-4, 2003.
- Zahnle, K. J., Cratering rates on Europa, in *Lunar and Planetary Institute Conference Abstracts*, p. 1699, 2001.